Sheared peridotite and megacryst formation beneath the Kaapvaal craton: a snapshot of tectonomagmatic processes across the lithosphere–asthenosphere transition

✉Sebastian Tappe [a, *], Malcolm Massuyeau [a, b], Katie A. Smart [c], Alan B. Woodland [d], Nikolaus Gussone [b], Sarah Milne [a], Andreas Stracke [b]

[a] Deep & Early Earth Processes (DEEP) Research Group, Department of Geology, University of Johannesburg, 2006 Auckland Park, South Africa

[b] Institut für Mineralogie, Westfälische Wilhelms-Universität, 48149 Münster, Germany

[c] School of Geosciences, University of the Witwatersrand, 2050 Johannesburg, South Africa

[d] Institut für Geowissenschaften, Goethe-Universität, 60438 Frankfurt am Main, Germany

[*] ***Corresponding author (S.Tappe):*** Department of Geology, University of Johannesburg, P.O. Box 524, 2006 Auckland Park, Gauteng, South Africa; Tel: +27-011-5594716; Fax: +27-011-5594702; E-mail: sebastiant@uj.ac.za

Running title: Origins of sheared peridotite xenoliths

ABSTRACT

The cratonic lithosphere–asthenosphere boundary is commonly invoked as the site of sheared peridotite and megacryst formation, a well-recognized petrologic assemblage whose genetic relationships – if any – remain poorly understood. We have undertaken a comprehensive petrology and Sr-Nd-Hf-Ca isotope study of sheared peridotite xenoliths and clinopyroxene megacrysts from the ca. 1150 Ma Premier kimberlite pipe on the central Kaapvaal craton in South Africa. New textural and mineral trace element evidence suggests that strong tectonic and magmatic overprinting affected the lower cratonic mantle over a vertical distance of ≥50 km from the lithosphere–asthenosphere boundary located at ~200-225 km depth. Although modification of the central Kaapvaal cratonic mantle is commonly linked to the ca. 2056 Ma Bushveld large igneous event, our thermobarometry, mantle redox, and Sr-Nd-Hf-Ca isotope data support a model in which volatile-rich low-volume melts and associated high-density fluids refertilized the lithosphere base shortly before or during asthenosphere-derived kimberlite and carbonatite magmatism at around 1150 Ma. This episode of lithospheric mantle enrichment was facilitated by exceptionally strong shear movements, as are recorded in the plastically deformed peridotites. We argue that stress-driven segregation of percolating carbonated melts contributed to megacryst formation along, or in close proximity to, shear zones within the cratonic mantle lithosphere.

Integration of our results from the Kaapvaal craton and modern petrologic concepts allows for the identification of a lithosphere–asthenosphere transition zone between ~150-225 km depth. This horizon is defined by intersections of the ~40-42 mW/m^2 Premier paleogeotherm with *(1)* CO_2-H_2O-present solidus curves for peridotite (upper bound), and *(2)* typical mantle adiabats with potential temperatures between 1315 and 1420°C (lower bound). At Premier, the most strongly deformed sheared peridotites occur mainly between ~160–185

km depth, firmly within the lithosphere–asthenosphere transition zone. Contrary to many previous models, we suggest that sheared peridotite formation occurs in localized deformation zones spaced out across the entire width of the lithosphere–asthenosphere transition zone, rather than being restricted to a single thin layer at the craton base where mantle flow causes viscous drag. Hence, plate tectonic stresses acting on the lower cratonic lithosphere may be accommodated by extensive networks of shear zones, which provide transient pathways and sinks for percolating volatile-rich melts, linking the formation of megacrysts and sheared peridotites.

Keywords: Bushveld igneous event; Cratonic lithosphere evolution; Deformation-assisted melt segregation; Mantle redox; Sr-Nd-Hf-Ca isotopes; Thermobarometry

INTRODUCTION

Plate tectonics drives the compositional and dynamic evolution of the solid Earth. It mainly involves the rigid lithosphere, tessellated into discrete 'tectonic plates', and the rheologically weaker asthenosphere, *or* convecting upper mantle, over which the lithospheric plates move at different speeds and directions. The lithosphere–asthenosphere boundary (LAB) can be envisaged as a series of large-scale detachment zones along which tectonic strain caused by differential movements of mantle materials is accommodated (Eaton *et al.*, 2009). Beneath Archean cratons, the present-day LAB is typically located at 150–250 km depth, much deeper than in other continental settings or within the ocean basins, which complicates an accurate delineation of the cratonic LAB by geophysical methods (Jordan, 1978; Artemieva & Mooney, 2001; Jones *et al.*, 2010; Priestley *et al.*, 2019). Lithospheric plates appear to be most strongly coupled to asthenospheric flow at the base of thick continental roots (Stoddard & Abbott, 1996; Conrad & Lithgow-Bertelloni, 2006; Mancinelli *et al.*, 2017), and this 'basal drag' provides an important driving force of plate tectonics in addition to slab pull and ridge push (Bokelmann, 2002; Bokelmann & Silver, 2002; Kennedy *et al.*, 2002; Eaton & Frederiksen, 2007; Kaban *et al.*, 2015). For example, kinematic reconstructions for the past 200 million years suggest that lithospheric plates with a high proportion of thick continental roots drifted more slowly than the much thinner oceanic plates or composite oceanic–continental plates that lack significant cratonic regions (Zahirovic *et al.*, 2015).

The physicochemical properties of mantle materials in the vicinity of the cratonic LAB are only poorly understood (O'Reilly & Griffin, 2010). While some workers suggested that strongly deformed lherzolite xenoliths in kimberlites represent samples of upwelling asthenosphere near the cratonic LAB (Nixon & Boyd, 1973b; Green & Gueguen, 1974; Boyd & Nixon, 1975; Goetze, 1975; Mercier, 1979; Allegre *et al.*, 1982; Boyd *et al.*, 1985), more

recent interpretations view such 'porphyroclastic' or 'hot sheared' lherzolites (hereafter 'sheared peridotites') as the product of plastic deformation and refertilization–rehydration of ancient depleted peridotite protoliths at the base of cratonic lithosphere (Pearson *et al.*, 1995; Kopylova *et al.*, 1999; Kennedy *et al.*, 2002; Baptiste *et al.*, 2012; Agashev *et al.*, 2013; Doucet *et al.*, 2013; van der Meer *et al.*, 2013; Kargin *et al.*, 2017; Kopylova *et al.*, 2019), although somewhat shallower cratonic mantle shear zones have also been invoked (Katayama *et al.*, 2009). As such, sheared peridotites provide rare snapshots of the tectonic and magmatic interactions between the lithosphere and the underlying asthenosphere, adding to our knowledge about the dynamic Earth. More specifically, studies of sheared peridotite xenolith suites allow for estimates on the positions of the LAB at the time of kimberlite eruptions (O'Reilly & Griffin, 2010). They also provide insights into whether the lithosphere–asthenosphere interface is diffuse and several 10s of kilometers thick (Mancinelli *et al.*, 2017), or relatively sharp occurring over ≤15 km vertical distance (Eaton *et al.*, 2009; Tharimena *et al.*, 2017). The elemental and isotopic compositions of sheared peridotites and their constituent minerals provide information on the nature and origin of deep percolating melts (e.g., basaltic *versus* volatile-rich melts including diverse types of high-density fluids), with possible implications for diamond formation (Weiss *et al.*, 2011; Smith *et al.*, 2012; Jablon & Navon, 2016), kimberlite magma production and ascent (Moore & Belousova, 2005; Gregoire *et al.*, 2006; Arndt *et al.*, 2010), as well as high-resolution geophysical imaging of the elusive LAB beneath continental shields (Gaillard *et al.*, 2008; Massuyeau *et al.*, 2021).

This study evaluates a new comprehensive petrology (e.g., thermobarometry calculations, mantle redox measurements, mineral trace element analyses) and Sr-Nd-Hf-Ca isotope dataset for sheared peridotite xenoliths and clinopyroxene megacrysts from the ca. 1150 Ma Premier kimberlite pipe on the Kaapvaal craton in South Africa (Fig. 1). The results are integrated to further develop concepts of the nature and evolution of the cratonic LAB,

including the tectonomagmatic processes that shape this important boundary layer. We also assess the possibility that our sheared and metasomatized peridotite samples may present vestiges of the viscous drag applied to the underside of the 'Kalahari' tectonic plate by strong asthenospheric flow during the 1220–1090 Ma Namaqua-Natal orogeny, which was caused by collisions between the Kaapvaal craton and numerous surrounding terranes (Fig. 1).

GEOLOGICAL BACKGROUND AND SAMPLES

The 1153.3 ± 5.3 Ma Premier kimberlite diatreme on the central Kaapvaal craton in South Africa has a preserved surface area of ~32 hectares and thus presents one of the largest volcanic pipe structures in the world (Tappe *et al.*, 2018a). Premier pipe has been mined intermittently since 1903 and holds the record for the largest ever discovered gem-quality diamond – the 3106 carats 'Cullinan' stone. The deposit is renowned for the recovery of exceptionally large and pure high-value Type-II diamonds, and it ranks among the top five diamond mines by value with more than 20 billion US$ in contained revenue (de Wit *et al.*, 2016).

The Premier kimberlite and associated rare carbonatite dykes are part of a cluster of 11 known pipes that intruded at the southern periphery of the Bushveld Complex some 50 km northeast of Johannesburg (Fig. 1). At the present erosion and mining levels, the kimberlite magmas and associated volcaniclastic materials erupted through sedimentary rocks of the 2650 – 2200 Ma Transvaal Supergroup and mafic–ultramafic rocks of the ca. 2056 Ma Bushveld Complex (Field *et al.*, 2008). Although emplacement of the Premier kimberlite cluster has previously been linked to the formation of Mesoproterozoic alkaline and carbonatite complexes on the central Kaapvaal craton (Kramers & Smith, 1983; Harmer, 1999; Verwoerd, 2006), improved age constraints established a >200 million years gap

between these events (Elburg & Cawthorn, 2017; Tappe *et al.*, 2018a). This new finding rules out direct petrogenetic links between these discrete mantle-derived magmatic episodes, and it underpins that the Kaapvaal lithospheric root had been affected repeatedly by carbonate-rich and alkaline magmatism during the Mesoproterozoic (Fig. 1).

The combined Nd-Hf-Os isotope systematics of kimberlite and carbonatite dykes from Premier pipe suggest ultimate melt origins from the convecting upper mantle to the transition zone, with variable degrees of melt–rock interaction upon encounter of the overriding cratonic mantle lithosphere (Tappe *et al.*, 2020b). These radiogenic isotope data are compatible with recent results for rare mineral inclusion-bearing Type-II diamonds from Premier pipe that suggest ultimate origins of these stones from below the cratonic lithosphere well within the convecting mantle (Smith *et al.*, 2016; Korolev *et al.*, 2018a; Nestola *et al.*, 2018; Smith *et al.*, 2018). However, an origin of 'ultradeep' Type-II diamonds from the cratonic mantle near the LAB, either as part of megacryst-forming events (Moore, 2009; Moore & Helmstaedt, 2019) or as subcreted 'fossil' upwelling mantle (Haggerty, 2017; Tappe *et al.*, 2020a), is equally plausible.

The Kaapvaal craton is one of the best studied sizeable remnants of an Archean continent (de Wit *et al.*, 1992; Poujol *et al.*, 2003; Hofmann *et al.*, 2019), and the nature of its thick mantle root has profoundly influenced models of cratonic lithosphere formation (Boyd *et al.*, 1985; Pearson, 1999; O'Reilly *et al.*, 2001; Woodland & Koch, 2003; Carlson *et al.*, 2005; Aulbach, 2012; Herzberg & Rudnick, 2012; Kamber & Tomlinson, 2019). The craton comprises two major Early Archean blocks of typical granite–greenstone lineage, which were brought together during Late Archean subduction and collision tectonics (Shirey *et al.*, 2002; Schmitz *et al.*, 2004; Smart *et al.*, 2016). Whereas the western cratonic domain, or so-called Kimberley block, exhibits one of the highest incidences of kimberlite magma eruptions during

the Mesozoic (Tappe *et al.*, 2018b) with fairly efficient sampling of the western Kaapvaal mantle lithosphere (Bell *et al.*, 2003; Grégoire *et al.*, 2003; Griffin *et al.*, 2003; Simon *et al.*, 2007; Gibson *et al.*, 2008; Rehfeldt *et al.*, 2008; Creighton *et al.*, 2009; Katayama *et al.*, 2009; Lazarov *et al.*, 2009; Hanger *et al.*, 2015; Tomlinson *et al.*, 2018; Shu *et al.*, 2019; Smart *et al.*, 2021a), the central plus eastern domains (i.e., the Witwatersrand block – host to Premier kimberlite pipe) are less well studied in terms of their cratonic mantle compositions (Pearson *et al.*, 1995; Gregoire *et al.*, 2005; Viljoen *et al.*, 2009; Aulbach & Viljoen, 2015; Shu & Brey, 2015; Burness *et al.*, 2020; Smart *et al.*, 2021b). In general, the thermal state and chemical composition of the Kaapvaal mantle lithosphere are regionally highly heterogeneous (Bell *et al.*, 2003; Griffin *et al.*, 2003), which is also recognized in irregular present-day P-wave velocity patterns at cratonic mantle depth levels imaged in seismic tomography studies (James *et al.*, 2001; Fouch *et al.*, 2004). Regions with high seismic P-wave velocities reflect strongly depleted mantle lithosphere or cooler conductive geotherms. In contrast, low P-wave velocities reflect refertilisation–rehydration of the cratonic mantle root or warmer local geotherms, which may be causally linked to voluminous regional intraplate magmatism such as the ca. 2056 Ma Bushveld or the ca. 180 Ma Karoo large igneous events (Griffin *et al.*, 2003; Fouch *et al.*, 2004; Shirey *et al.*, 2004; Rehfeldt *et al.*, 2007; Giuliani *et al.*, 2014). In this context it should be noted that the Premier kimberlite pipe at the southern margin of the Bushveld Complex is located in a region of the central Kaapvaal craton that is characterized by lower present-day seismic P-wave velocities (James *et al.*, 2001; Shirey *et al.*, 2002).

The paleogeotherm beneath the ca. 1150 Ma Premier kimberlite pipe has been constrained at ~39 – 45 mW/m^2 based on peridotite xenolith and single-grain clinopyroxene thermobarometry (Danchin, 1979; Finnerty & Boyd, 1987; Viljoen *et al.*, 2009; Nimis *et al.*, 2020). These heat flow estimates were obtained by application of a range of methods and models, which are often not directly comparable (see Kopylova *et al.*, 2019). Nevertheless, it

is reasonable to conclude that the study area had a slightly elevated cratonic geotherm at 1150 Ma. This observation, together with ca. 2 Ga old lherzolitic mineral inclusions in some diamonds (Richardson *et al.*, 1993) and ca. 2 Ga rhenium depletion model ages of many peridotite xenoliths from Premier (Pearson *et al.*, 1995; Morel *et al.*, 2008), led several authors to propose that the central Kaapvaal mantle lithosphere had been heavily overprinted by the Bushveld magmatic event (Danchin, 1979; Griffin *et al.*, 2003; Gregoire *et al.*, 2005; Richardson & Shirey, 2008; Viljoen *et al.*, 2009; Viljoen *et al.*, 2014; Korolev *et al.*, 2018b). It should be noted, however, that the southern African cratonic and peri-cratonic lithosphere is generally characterized by 'warmer' conductive geotherms over the past one billion years approaching 42 mW/m^2 in places (Rudnick & Nyblade, 1999; Grütter, 2009; Ngwenya & Tappe, 2021). Hence, the impact by heat advection, emanating from giant mantle-derived magmatic events, on the thermal structure of dynamically evolving cratonic mantle lithosphere may be overestimated (Bell *et al.*, 2003; Kobussen *et al.*, 2009).

In 2015 and 2016, we collected >50 new sheared peridotite xenoliths from the Premier kimberlite pipe at Cullinan Diamond Mine. After an initial inspection of these nodules in petrographic thin sections, 14 fresh sheared peridotite xenoliths were identified as suitable for pressure–temperature estimations and geochemical analyses; i.e., they exhibit a 'touching' garnet, orthopyroxene, clinopyroxene and olivine phase assemblage (Figs. 2-4). For comparative purposes we also included a single coarse-grained granular garnet peridotite xenolith into the analytical program (Fig. 2D). In addition, 10 clinopyroxene megacrysts recovered from the oversize tailings dumps are incorporated into our petrology and isotope geochemistry study, because previous models suggest links between the formation of sheared peridotites and megacrysts near the cratonic LAB (Nixon & Boyd, 1973a, b; Moore & Lock, 2001; Moore & Belousova, 2005; Bussweiler *et al.*, 2018).

METHODS AND APPROACH

Electron microprobe analysis

Quantitative major and minor element compositions of silicates were determinded on polished thin sections and epoxy grain mounts with a Cameca SX100 electron microprobe at the University of Johannesburg in South Africa. The instrument was operated at 20 kV acceleration voltage and a beam current of 20 nA was applied. The electron beam was adjusted for 1 μm spot analyses. Signal counting times varied between 40 and 60 seconds on peak, depending on the chemical element of interest. The electron microprobe was calibrated using the following natural and synthetic reference materials: diopside (Si), almandine garnet (Al), hematite (Fe), wollastonite (Ca), olivine (Mg), rhodonite (Mn), orthoclase (K), jadeite (Na), as well as pure TiO_2, Cr_2O_3 and NiO. The elements were measured on their X-ray Kα lines employing all four wavelength dispersive spectrometers. Raw data reduction and matrix corrections were done with the 'X-PHI' method, which is a φ(ρz)-type off-line analytical protocol. Emphasis was laid on the detection of potentially occurring major and minor element zoning within individual mineral grains; however, the observed intra-grain compositional variability – if any – is within the reproducibility of our analytical technique (Ngwenya & Tappe, 2021). Backscatter electron imagery also demonstrates compositional homogeneity of all present silicate phases within any given peridotite xenolith sample (except for porous/spongy clinopyroxene rims due to partial melting) (Figs. 3, 4). This confirms attainment of full mineral major element equilibrium (Finnerty & Boyd, 1984; Nimis & Grütter, 2010), which is a prerequisite to the application of meaningful thermobarometry. To this end, we also generated backscatter electron maps for selected thin sections at full scale (Fig. 3A) using a FEI Quanta 600F Mineral Liberation Analyser system at the University of

Johannesburg. The instrument is equipped with two Bruker 4010 Xflash X-ray detectors, and operating conditions are given in Ngwenya & Tappe (2021).

Laser ablation ICP-MS analysis

Mineral trace element concentrations were determined in situ by laser ablation inductively coupled plasma mass spectrometry (LA-ICP-MS) at Stellenbosch University in South Africa and at the University of Münster in Germany. Eight representative peridotite xenoliths and all ten clinopyroxene megacrysts from the Premier kimberlite pipe were crushed in an agate mortar and visibly clear crystal fragments of the 0.5 – 1.2 mm size fraction were mounted in epoxy resin at the University of Johannesburg. Orthopyroxene and clinopyroxene grain mounts were analysed at Stellenbosch University and the garnet grain mounts were measured at the University of Münster. Several garnet grains were analysed as replicates in Stellenbosch, and the trace element results from the two laboratories agree within 20% in all cases and within 10% in most cases. However, only the garnet dataset from Münster is reported and discussed in the main manuscript.

The LA-ICP-MS setup at Stellenbosch University consists of an excimer laser system emitting at 193 nm (Resonetics Resolution M50) coupled to an Agilent 7700 quadrupole ICP-MS instrument. Ablations were performed in a double helix Laurin Technic cell in helium carrier gas that was mixed into the argon sample gas, with nitrogen added to the gas mixture at a rate of 5 ml per minute prior to introduction into the mass spectrometer. Each analysis included 35 seconds of sample ablation plus background readings for 15 seconds prior to ablation. NIST SRM 610 glass was analysed as the calibration standard every 15 unknowns, which included analyses of the USGS basalt glasses BCR and BHVO as secondary reference materials for evaluations of accuracy and precision. Trace element concentrations were obtained by spot analysis using a beam diameter of 100 μm. Up to five spot analyses were

carried out per mounted grain and average trace element compositions for each grain studied were calculated. The reduction of time-resolved raw data and calculations of trace element concentrations were performed with Iolite 3.3, using ^{29}Si as internal standard matched against the electron microprobe data. The results for the BCR and BHVO glasses are within the 2-sigma uncertainty margins of the recommended average element concentrations and typically reproduce better than 6% (http://georem.mpch-mainz.gwdg.de). Detection limits for most analysed trace elements are in the low ppb range or better. Further details about the Stellenbosch LA-ICP-MS setup are provided in Smart et al. (2017).

In Münster, the LA-ICP-MS system consists of a 193 nm Photon Machine excimer laser coupled to a ThermoFisher Scientific Element-2 SF-ICP-MS instrument (see the detailed method description in Beyer et al., 2013). Ablations were performed in a Helex cell in helium carrier gas that was mixed into the argon sample gas, with nitrogen added to the gas mixture prior to entering the mass spectrometer. Each analysis included 40 seconds of sample ablation plus background readings for 20 seconds before ablation. The NIST SRM 612 glass was analysed as the calibration standard every 30 unknowns, which included analyses of the basalt glasses BIR-1, BCR-2 and BHVO-2 as secondary reference materials for data quality control (Supplementary Data Appendix A). Trace element concentrations were determined by spot analysis applying a 85 µm beam diameter. Five spot analyses were carried out per mounted garnet grain and average trace element compositions for each grain studied were calculated. Data reduction and the calculation of trace element concentrations were performed with GLITTER 4.4, using ^{29}Si as internal standard. Results for the basaltic glasses are within the 2-sigma uncertainty margins of the recommended average element concentrations and reproduce better than 5% (http://georem.mpch-mainz.gwdg.de). We also analysed mounted GHR-1 garnet and KBY17-4 clinopyroxene as in-house reference materials (Supplementary Data Appendix A), and the results for petrogenetically important trace elements such as Ni

and the REE are within the 2-sigma uncertainty margins of the average concentrations recommended in Smart et al. (2021). Detection limits for all analysed trace elements of interest are in the low ppb range or better.

Mössbauer spectroscopy

The Fe^{3+} contents of garnet were determined by Mössbauer spectroscopy at Frankfurt University in Germany, and they are reported in Table 1 as $Fe^{3+}/\Sigma Fe$. Spectra were obtained from visually clean hand-selected garnet grains that had been separated from five suitable sheared peridotite xenoliths from the Premier kimberlite pipe. The cleaned garnet separates were milled into powder and subsequently mixed with a small amount of sugar crystals prior to placement into a Pb sample holder. The amount of sample (10-20 mg) and sample diameter were adjusted to create sample thicknesses of <5 mg/cm^2 to mitigate saturation effects. Measurements were made at constant acceleration with a velocity ramp of ±5 mm/s and a 50 mCi ^{57}Co in Rh source. Mirror-image spectra, calibrated against α-Fe metal foil, were collected over 512 channels until 2×10^6 counts per channel were reached. Fitting of the garnet spectra followed the approach of Woodland & Koch (2003), which included a correction for different recoil free fractions of Fe^{2+} and Fe^{3+} in garnet.

Corrected $Fe^{3+}/\Sigma Fe$ ratios for the peridotite-derived garnet fractions are reported in Table 1, and they have absolute uncertainties of ±0.01 (Woodland & Koch, 2003). Peridotite fO_2 values are reported relative to the fayalite-magnetite-quartz (FMQ) reference buffer and they were calculated using the oxybarometer formulation of Stagno et al. (2013). This oxybarometer requires as input: *(1)* pressure-temperature estimates, *(2)* garnet major element compositions including the corrected $Fe^{3+}/\Sigma Fe$ ratios, and *(3)* Fe^{2+}/Mg ratios of coexisting olivine and orthopyroxene. All reported peridotite fO_2 literature data (Supplementary Data Appendix B), as determined by garnet Fe^{3+} analyses, were recalculated applying the same

thermobarometer combination (Nickel & Green, 1985; Taylor, 1998) and oxybarometer (Stagno *et al.*, 2013) to enable meaningful comparisons in depth–fO_2 space.

Sr-Nd-Hf isotope ratio determinations

Clinopyroxene mineral separates were produced from six representative peridotite xenoliths and the ten megacrysts following coarse crushing steps in an agate mortar and sieving of the crushed material to collect the grain size fraction between 0.5 and 1.2 mm. Visually clean and inclusion-free clinopyroxene crystal fragments were hand-selected under a binocular microscope at the University of Johannesburg to obtain pure mineral fractions weighing between 18 and 180 mg. Representative crystal fragments from each sample were mounted in epoxy resin for trace element determinations by LA-ICP-MS analysis (see above).

The bulk of the clinopyroxene fractions was washed in deionized H_2O, transferred into Savillex teflon vials and dissolved in concentrated HF–HNO_3 (3 / 1) on a hotplate at 150°C for 48 hours (University of Münster). Sample solutions were gently dried down and the residues were redissolved in 6N HCl alternating between a hotplate and an ultrasonic bath. This dissolution step was repeated at least twice until clear solutions were obtained. Approximately 10 wt.% of each sample solution was allocated for Ca isotope analytical work (see below). The other 90 wt.% of the solutions were processed through ion exchange chromatography to isolate Sr (AG50W-X8 cation resin, 200–400 mesh, (Hart & Brooks, 1977)) and Nd-Hf (LN Spec anion resin, 50–100 mesh, (Pin & Zalduegui, 1997; Münker *et al.*, 2001)) fractions for isotope ratio determinations at the University of Münster. The total procedural blanks are typically <50 pg Sr, <30 pg Nd and <10 pg Hf, and are negligible (Tappe *et al.*, 2020b).

Strontium isotope ratio measurements were performed on a Thermo Scientific Triton TIMS instrument (^{85}Rb monitored to correct for the potential presence of interfering ^{87}Rb was negligible), whereas Nd and Hf isotope ratios were measured in solution mode with a Thermo Scientific Neptune Plus MC-ICP-MS instrument in static collection mode. Measured $^{87}Sr/^{86}Sr$, $^{143}Nd/^{144}Nd$ and $^{176}Hf/^{177}Hf$ ratios were normalized using an exponential mass fractionation law and the recommended $^{88}Sr/^{86}Sr$ (8.37521), $^{146}Nd/^{144}Nd$ (0.7219) and $^{179}Hf/^{177}Hf$ (0.7325) ratios. The measured Sr-Nd-Hf isotope ratios for all sample and secondary standard runs are reported relative to $^{87}Sr/^{86}Sr = 0.710245$ for NBS987 (Thirlwall, 1991), $^{143}Nd/^{144}Nd = 0.512115$ for JNdi-1 (Tanaka *et al.*, 2000), and $^{176}Hf/^{177}Hf = 0.282160$ for AMES / JMC-475 (Blichert-Toft *et al.*, 1997) standard solutions, respectively. During the course of multiple analytical sessions in Münster in 2018–2019, repeated measurements of $^{87}Sr/^{86}Sr$ for the NBS987 primary standard averaged 0.710250 ±11 (2S.D., n=5), $^{143}Nd/^{144}Nd$ for the JNdi-1 primary standard averaged 0.512072 ±17 (2S.D., n=20), and $^{176}Hf/^{177}Hf$ for the AMES primary standard averaged 0.282146 ±9 (2S.D., n=16). During this analysis period we also processed the USGS basaltic reference materials BCR-2 and BHVO-2 alongside our samples, and the results are in good agreement with previous measurements (Weis *et al.*, 2006; McCoy-West *et al.*, 2010; Chauvel *et al.*, 2011). For BCR-2 the obtained values are: $^{87}Sr/^{86}Sr = 0.705005$ ±7 (2S.D., n=2), $^{143}Nd/^{144}Nd = 0.512635$ ±6 (2S.D., n=3), $^{176}Hf/^{177}Hf = 0.282873$ ±22 (2S.D., n=3). For BHVO-2 the obtained values are: $^{87}Sr/^{86}Sr = 0.703469$ ±7 (2S.D., n=2), $^{143}Nd/^{144}Nd = 0.512990$ ±16 (2S.D., n=3), $^{176}Hf/^{177}Hf = 0.283108$ ±13 (2S.D., n=3) (Tappe *et al.*, 2020a).

Parent-daughter element ratios were calculated using the Rb, Sr, Sm, Nd, Lu and Hf concentrations of clinopyroxene as determined by the LA-ICP-MS method for the same sample aliquots used for solution mode Sr-Nd-Hf isotope analytical work. All initial isotope ratios and notations are reported for the Premier kimberlite magma emplacement age of ca.

1150 Ma (Tappe *et al.*, 2018a). Corrections of measured $^{87}Sr/^{86}Sr$ for 1150 million years of in situ ^{87}Rb decay are small due to the generally low Rb/Sr nature of clinopyroxene, whereas calculations of the initial $^{143}Nd/^{144}Nd$ and $^{176}Hf/^{177}Hf$ ratios are associated with a substantial error propagation resulting in uncertainties of 0.7–1.3 and 0.5–1.0 epsilon units at the 2-sigma level, respectively. The 2-sigma uncertainties of the calculated initial epsilon Nd and Hf values entail a propagation of errors assuming normally distributed data (Table 2), for which the uncertainties of the 1150 Ma emplacement age and parent-daughter element ratios were set at 1% (i.e., 1150 ±12 Ma) and 5%, respectively. The following decay constants were used for age corrections: ^{87}Rb 1.42×10^{-11} a^{-1}; ^{147}Sm 6.54×10^{-12} a^{-1}; ^{176}Lu 1.865×10^{-11} a^{-1} (see Tappe *et al.*, 2020b for references).

Ca isotope ratio determinations

Approximately 10 wt.% of each sample solution prepared for Sr-Nd-Hf isotope analytical work was transferred into Savillex teflon vials and mixed with a ^{42}Ca–^{43}Ca double-spike to enable correction for isotope fractionation during mass spectrometry (Gussone *et al.*, 2011). Calcium isotope ratio measurements were performed at the University of Münster on the same Thermo Scientific Triton TIMS instrument as used for the Sr isotope ratio determinations (see above). Purified Ca was loaded onto Re single filaments with a Ta activator in sandwich technique (Gussone *et al.*, 2010). The Ca isotope variations are expressed as $\delta^{44/40}Ca$ values relative to the NIST SRM-915a standard: $\delta^{44/40}Ca$ [‰] = $(((^{44}Ca/^{40}Ca)_{sample} / (^{44}Ca/^{40}Ca)_{SRM\text{-}915a} - 1) \times 1000$.

All sample data are normalised to the average value of the 3 to 5 measurements of SRM-915a per turret during a TIMS analytical session to mitigate potential effects of collector cup-degradation. Replicate measurements of samples and standards yielded an average 2S.D. of approximately 0.05‰ (an individual analysis consisted of 180 cycles over a ca. 40 minute

period). The average value of 20 analyses of SRM-915b is 0.76 ±0.02‰ (2S.E.) *or* ±0.09% (2S.D.) relative to SRM-915a, which is in good agreement with the recommended value of 0.72‰ (Heuser *et al.*, 2016). Nine analyses of the IAPSO seawater standard yielded a value of 1.87 ±0.03‰ (2S.E.) *or* ±0.09% (2S.D.) during the analytical sessions in Münster in April/May 2018, which is in good agreement with the seawater $\delta^{44/40}$Ca values compiled in Heuser *et al.* (2016).

Thermobarometry

Pressure–temperature estimations

Pressures and temperatures (P-T) of last equilibration were calculated from the acquired plus quality-screened mineral compositional data for the peridotite xenoliths and clinopyroxene megacrysts following the guidelines of Nimis & Grütter (2010). For the garnet peridotite xenoliths we applied two well-established thermobarometer combinations: *(1)* Taylor (1998) – Nickel & Green (1985) *[hereafter TNG]*, and *(2)* Brey & Köhler (1990). For both combinations the temperature estimates are obtained from two-pyroxene Fe-Mg exchange equilibria and the pressure estimates from Al-exchange equilibrium between coexisting orthopyroxene and garnet. Although these two thermobarometer combinations yield systematically different P-T values for individual data inputs (Supplementary Data Appendix C; see also Kopylova *et al.*, 2019), the obtained P-T arrays, or shapes of the resultant paleogeotherms, are identical within uncertainties. However, fitting of garnet-facies peridotite xenoliths P-T arrays using the numerical *FITPLOT* model (McKenzie & Bickle, 1988) shows that the *TNG* thermobarometer combination results in more precise estimates of lithosphere thickness, which was also pointed out by Mather et al. (2011). This observation is in good agreement with the reappraisal of widely used barometers and thermometers by Nimis & Grütter (2010), who recommended the *TNG* combination as the most accurate currently

available. Pressure–temperature estimates of last equilibration for the clinopyroxene megacrysts were obtained using the single-grain thermobarometer of Nimis & Taylor (2000), implementing the new data quality-control screens developed by Ziberna et al. (2016).

Pressure–temperature array ('geotherm') fitting

The obtained garnet peridotite xenolith and clinopyroxene megacryst P-T arrays were quantitatively fitted to calculate paleogeotherms utilizing the numerical *FITPLOT* model (McKenzie & Bickle, 1988; Mather *et al.*, 2011). Besides equations that describe the thermal properties of peridotite-dominated lithospheric mantle, *FITPLOT* requires the following input parameters for the crustal and mantle portions of the lithosphere column under investigation: *(1)* thickness and heat production of the upper and lower crust, *(2)* heat production of the lithospheric mantle, and *(3)* potential temperature T_P of the sublithospheric convecting upper mantle, *or* asthenosphere.

For *FITPLOT* geotherm calculations using our P-T dataset for xenoliths and megacrysts from the ca. 1150 Ma Premier kimberlite we applied the upper (23 km) and lower (27 km) crustal thicknesses reported for the Rehoboth terrane (Youssof *et al.*, 2013) (Fig. 1). These values are the current best estimates of thickened Precambrian crust on and off the Kaapvaal craton in southern Africa (Stankiewicz & de Wit, 2013), as for example in the vicinity of the ca. 2056 Ma Bushveld Complex, where 5-10 km of mafic material had been 'underplated' during this large igneous event (Wright *et al.*, 2003). Values for heat production of the upper (1.4 $\mu W/m^3$) and lower (0.3 $\mu W/m^3$) cratonic crust, as well as of the continental lithospheric mantle (zero), are taken from Rudnick & Nyblade (1999) and Michaut et al. (2007). In our paleogeotherm calculations for the central Kaapvaal craton at Mesoproterozoic times we applied a range of mantle potential temperatures between 1315 and 1420ºC,

corresponding to estimates of ambient upper mantle temperatures at around 1.1 Ga (Davies, 2009; Ganne & Feng, 2017); i.e., at the time of Premier kimberlite magma eruption.

RESULTS

Petrography of the mantle-derived peridotite xenoliths from Premier

The investigated 15 garnet peridotite xenoliths range in size between 3 and 10 cm (Fig. 2). Abundances of the primary rock-forming minerals were visually estimated during microscopy of polished petrographic thin sections (Table 1). The xenoliths are dominated by olivine (typically >70 vol.%) and contain variably small but significant amounts of orthopyroxene, clinopyroxene and garnet. On the basis of this mineral assemblage, the ultramafic xenoliths are identified as garnet lherzolites. Although the studied lherzolite nodules are very fresh, round to elongate garnet and orthopyroxene porphyroclasts typically exhibit a thin 'coat' of dark brown to black reaction products (Fig. 3). Applying the terminology of Harte (1977), the 14 'sheared peridotite' xenoliths have mosaic–porphyroclastic textures, whereas the 'coarse peridotite' nodule CIM15-40 lacks porphyroclasts and has a relatively homogeneous grain size distribution between 2–5 mm (Fig. 2D; Table 1). The sheared peridotites contain mm-sized porphyroclasts comprising single and composite grains of garnet, orthopyroxene, clinopyroxene and rare olivine, set in a fine-grained matrix of recrystallized olivine, where neoblast sizes typically range between 30–300 μm across (Figs. 3, 4). Although single-crystal porphyroclasts, often showing incipient subgrain formation along grain boundaries, may occur in isolation within the olivine-rich matrix, mm-sized lenses and stringers consisting of composite garnet–pyroxene assemblages are common (Figs. 3, 4). The lenses may form sheared and folded bands imparting a 'fluidal' rock texture (Fig. 4C), and their clinopyroxene constituents are commonly porous to spongy along the margins indicative of incipient melting

(Kopylova *et al.*, 2021). Orthopyroxene porphyroclasts also show evidence of partial melting such as the development of diffuse clinopyroxene coronas (Fig. 4E). Among the sheared peridotite xenoliths, sample CIM15-35 and CIM15-50 exhibit cm-sized round clusters *or* 'pockets' of ultra-coarse garnet and clinopyroxene assemblages set in a fine-grained olivine-rich matrix (Supplementary Data Figure 1). This 'coarse-in-sheared' texture may represent in situ megacryst formation. Ten discrete clinopyroxene megacrysts studied range in size between 1 and 3 cm across.

Pressure–temperature array

Conventional thermobarometry was applied to estimate the P-T conditions for 14 sheared peridotite xenoliths from Premier (Table 1). The sheared peridotites equilibrated last at 5.2–5.6 GPa (~170–185 km depth) and 1208–1324°C, with the exception of CIM15-35 (4.8 GPa and 1088°C). The coarse peridotite xenolith CIM15-40 equilibrated last at much shallower conditions at ~2.8 GPa (~90 km depth) and ~809°C. Eight clinopyroxene megacrysts equilibrated over a wide P-T range between 4.1–6.3 GPa (~135–210 km depth) and 1026–1382°C (Fig. 5). Sample CUL17-cpx4 falls off the megacryst P-T trend (~7.2 GPa and ~1313°C; see Discussion) and CUL17-cpx8 is not suitable for single-grain thermobarometry due to its very low Cr content (Supplementary Data Appendix D).

All investigated samples, except for the 'shallow' coarse peridotite xenolith CIM15-40, are derived from the diamond stability field (Fig. 5) applying the graphite–diamond transition curve of Day (2012). The majority of analysed sheared peridotite xenoliths (n=12) form a cluster in P-T space between 5.2–5.6 GPa and 1294–1324°C (Fig. 5), recording warmer conditions than the 40 mW/m^2 model conductive geotherm of Hasterok & Chapman (2011). The cluster of high-temperature sheared peridotite analyses is equivalent to the 'hot deformed' peridotite xenolith suite from Premier discussed in Viljoen *et al.* (2009), for which

we reprocessed the original data with our methodology where possible to ensure data compatibility. These authors noted that the Premier peridotite xenoliths fall between the 40 and 45 mW/m^2 model geotherms of Pollack & Chapman (1977), which tend to be slightly warmer near the cratonic LAB than the model of Hasterok & Chapman (2011). Regardless, the P-T array fit for the peridotite xenoliths *versus* the fit for xenoliths plus clinopyroxene megacrysts (excluding CUL17-cpx4) yielded very similar geotherm shapes with the *FITPLOT* algorithm (Supplementary Data Figure 2). This suggests that most of the megacrysts studied equilibrated with the diamondiferous lithospheric mantle root of the central Kaapvaal craton by ca. 1150 Ma (see also Bell & Moore, 2004). Recently, Nimis *et al.* (2020) presented a large P-T dataset for clinopyroxene from Premier pipe, which comprises two subsets of grains that fall either along a ~38-40 mW/m^2 *(xenocrysts and inclusions in diamond)* or along a ~36-37 mW/m^2 *(inclusions in diamond)* model conductive geotherm of Hasterok & Chapman (2011). Importantly, our clinopyroxene megacryst CUL17-cpx4 falls onto the newly identified enigmatic Premier model geotherm of ~36-37 mW/m^2. This rather 'cold' geotherm is subordinate to the more representative heat flow of ~40-42 mW/m^2 for the central Kaapvaal cratonic mantle root (Fig. 5).

The newly devised conductive paleogeotherm of ~40-42 mW/m^2 for the lithospheric mantle column of the central Kaapvaal craton (Fig. 1), which incorporates the new P-T data into the existing body of work on peridotite xenoliths, intersects the modern 1315°C mantle adiabat at approximately 200 km depth, defining a thermal lithosphere–asthenosphere boundary *or* LAB at 1150 Ma (Fig. 5). If a 1420°C mantle adiabat is applied, catering for a slightly warmer convecting upper mantle during the Mesoproterozoic (Davies, 2009; Ganne & Feng, 2017), then the central Kaapvaal lithosphere may have reached down to ~225 km depth at 1150 Ma (Fig. 5). Note that the pressure–depth conversion applied in this study is

based on the 'PREM' model (Dziewonski & Anderson, 1981), in which 1 GPa lithostatic pressure is equivalent to ~33 km depth (see also Cammarano, 2013).

Mineral major and trace element compositions

The major and trace element concentrations of mineral phases measured during this study are listed in Supplementary Data Appendix D, including mean and median values for each xenolith as used in pressure–temperature calculations (see above).

Olivine

Sheared peridotites contain two generations of olivine, and the olivine Mg-numbers (atomic $Mg/[Mg+Fe^{2+}]\times100$) for rare porphyroclasts and the abundant fine-grained neoblasts in the matrix overlap within the range of 89.9–91.7 (Fig. 6). These high Mg-number values are coupled to high Ni contents between 2947–3222 ppm. Olivine in sheared peridotite sample CIM15-23 has a lower Mg-number of ~87.6 and a lower Ni content of ~2750 ppm. Within individual sheared peridotite nodules the olivine major and minor element compositions are exceptionally homogenous in keeping with attainment of equilibrium. Olivine in the coarse peridotite xenolith CIM15-40 has a Mg-number value of ~91.7 and a Ni content of up to 3379 ppm, which fall at the upper end of the ranges displayed by the sheared peridotites (Fig. 6). In general, the olivine compositions of the peridotite xenoliths from Premier pipe studied here are notably less refractory than depleted low-temperature peridotites from cratonic mantle roots worldwide (Fig. 6), which typically have average Mg-number values between 92.4–92.9 (Boyd, 1989; Bernstein *et al.*, 2007; Pearson & Wittig, 2014).

Orthopyroxene

Orthopyroxene in the sheared peridotite xenoliths has a near end-member enstatite composition (~90 mol.%) with Mg-number values ranging between 91.1–92.6 (~89.2 for CIM15-23). Higher Mg-numbers of orthopyroxene compared with coexisting olivine have also been reported for garnet peridotite xenoliths from Kimberley and Lesotho on the Kaapvaal craton, which testifies to attainment of orthopyroxene-olivine equilibrium (Simon *et al.*, 2007). As observed for olivine, orthopyroxene in coarse peridotite xenolith CIM15-40 exhibits a Mg-number at the upper end of the range displayed by the sheared peridotites from Premier (~92.6).

The sheared peridotites contain orthopyroxene porphyroclasts with sinusoidal to hump-shaped chondrite normalized REE patterns that show LREE and HREE depletion relative to the MREE (Fig. 7). Although the REE as a group are depleted relative to chondrite, concentrations in orthopyroxene from Premier tend to be elevated compared with orthopyroxene from Lesotho and Kimberley low-temperature garnet peridotite xenoliths, which show much stronger MREE-HREE depletion (Simon *et al.*, 2003; Simon *et al.*, 2007). Orthopyroxene from the coarse peridotite xenolith CIM15-40 has a chondrite normalized REE pattern that shows LREE enrichment over the MREE, and much stronger HREE depletion compared with the sheared peridotites from Premier, more similar to some orthopyroxene patterns identified for Lesotho and Kimberley low-temperature peridotite xenoliths (Simon *et al.*, 2003; Simon *et al.*, 2007) (Fig. 7). All analysed orthopyroxene crystals from Premier garnet peridotite xenoliths show negative Th-U and positive Nb-Ta-Ti anomalies in primitive mantle normalized multi-element diagrams (not shown). Orthopyroxene porphyroclasts from the sheared peridotites show subtle positive anomalies at

Hf in these diagrams, which is not observed for the coarse peridotite sample CIM15-40 (not shown).

Clinopyroxene

Clinopyroxene porphyroclasts in the sheared peridotite xenoliths from Premier pipe are generally rich in Cr-diopside component with 0.59–1.73 wt.% Cr_2O_3 and Mg-number values between 89.8–91.6 (CIM15-23 clinopyroxene Mg-number is ~87.5). The Na_2O and TiO_2 contents are between 1.2–2 wt.% and 0.13–0.59 wt.%, respectively. Clinopyroxene in the coarse peridotite sample CIM15-40 has higher Cr_2O_3 (~1.8 wt.%) and Na_2O (~2.4 wt.%) concentrations, and a much higher Mg-number of ~93.5, whereas TiO_2 is relatively low at ~0.16 wt.%. The discrete clinopyroxene megacrysts display a wide range of Cr_2O_3 (0.02–1.09 wt.%), Na_2O (0.7–1.7 wt.%) and TiO_2 (0.09–0.51 wt.%) concentrations, with Mg-number values between 83.2–92.7. They share more compositional similarity with clinopyroxene porphyroclasts of the sheared peridotite xenoliths than with clinopyroxene in coarse peridotites from Premier (Viljoen *et al.*, 2009) (Fig. 8). Although the Premier clinopyroxene megacrysts have generally a 'low-Cr' nature, some crystals have higher Mg-number values and Cr_2O_3 contents of >0.7 wt.% partially overlapping the lower end of 'Cr-rich' clinopyroxene megacryst suites from cratons worldwide (Fig. 8B).

Clinopyroxene in the sheared peridotite xenoliths from Premier is generally LREE enriched (>10 times chondrite), with maxima at Pr-Nd and consistent levels of HREE depletion in chondrite normalized distribution patterns (Fig. 9). The coarse peridotite xenolith CIM15-40 contains clinopyroxene with even stronger LREE enrichment approaching 100 times chondritic values compared with clinopyroxene in the sheared nodules (Fig. 9A). This LREE enrichment level is more similar to clinopyroxene in low-temperature garnet peridotite xenoliths from Kimberley on the western Kaapvaal craton (Simon *et al.*, 2007). The discrete

clinopyroxene megacrysts from the Premier kimberlite pipe have identical chondrite normalized REE patterns that fully overlap those of clinopyroxene porphyroclasts from the sheared peridotite xenoliths (Fig. 9B). The only exception is megacryst CUL17-cpx4, which has much lower REE and HFSE concentrations (see Discussion). The clinopyroxene megacrysts and porphyroclasts from Premier also display very similar primitive mantle normalized multi-element patterns with similar concentration levels of Th-U-Nb-Ta, Sr and Zr-Hf (not shown).

Garnet

Garnets from the studied Premier peridotite samples have 'lherzolitic G9' affinities in terms of their Mg, Ca and Cr compositions (Fig. 10), which is compatible with the presence of significant clinopyroxene in these mantle-derived xenoliths (Sobolev *et al.*, 1973; Gurney & Zweistra, 1995; Grütter *et al.*, 2004). The sheared peridotites contain garnet porphyroclasts with Cr_2O_3 and TiO_2 concentrations between 1.9–6.7 wt.% and 0.48–1.56 wt.% respectively, compositional ranges that completely overlap with garnet in 'hot deformed' peridotites from Premier as reported in Viljoen *et al.* (2009). The pyrope-rich garnet porphyroclasts display a narrow range of Mg-number values between 82.4–85.7, with the exception of garnet from sheared peridotite xenolith CIM15-23, which has a lower Mg-number value of ~79.8, a trend that is also observed for olivine and the pyroxenes (see above). Major element compositions of garnet in the coarse peridotite xenolith CIM15-40 (e.g., Mg-number of ~82.9; ~2.5 wt.% Cr_2O_3) fall within the range of garnet compositions from the sheared peridotite xenolith suite (Fig. 10), except for the much lower TiO_2 content of ~0.1 wt.% (Fig. 11A), which is similar to garnet in other coarse peridotite xenoliths from Premier (Viljoen *et al.*, 2009). The garnet porphyroclasts in the sheared peridotite xenoliths resemble high-Cr megacrysts from kimberlite localities worldwide with regard to their elevated Mg- and Cr-numbers (Fig. 11B).

However, their elevated TiO_2 contents provide a good match to garnet compositions from metasomatized peridotite xenoliths of the Kaapvaal cratonic root (Fig. 11A).

The garnet porphyroclasts in the sheared peridotite xenoliths have 'normal' chondrite normalized REE patterns, with strong LREE depletions and a flat plateau for the MREE–HREE (Fig. 12A). The REE pattern for garnet in the coarse peridotite xenolith CIM15-40 is similar except for a slightly stronger LREE depletion. The enriched and positively correlated Y-Zr systematics of garnet porphyroclasts in the sheared peridotites from Premier follow the global trend of lherzolitic garnets from metasomatized cratonic mantle lithosphere (Griffin & Ryan, 1995; Griffin *et al.*, 1999; Viljoen *et al.*, 2009; Hunt *et al.*, 2012; Gibson *et al.*, 2013; Shu & Brey, 2015; Shaikh *et al.*, 2020) (Fig. 13A). The extremely high Ti/Eu of these garnets, coupled with low Zr/Hf, suggests an involvement of silicate-rich rather than carbonate-dominated metasomatic agents (Shu & Brey, 2015) (Fig. 13B), but these trace element proxies do not always provide meaningful insights into mantle enrichment processes (see Discussion). Regardless, the low Ti/Eu and high Zr/Hf ratios of garnets in the coarse peridotite xenolith CIM15-40, and in previously analysed coarse peridotite nodules from Premier (Viljoen *et al.*, 2009), point to contrasting metasomatic styles in the lithospheric mantle beneath the central Kaapvaal craton (Fig. 13B). Prominent HFSE enrichment of the sheared peridotite garnet porphyroclasts is also apparent in primitive mantle normalized multi-element diagrams, where Zr-Hf forms a plateau and Nb-Ta and Ti display slightly positive spikes (not shown). In contrast, garnet from the coarse peridotite xenolith CIM15-40 is characterized by negative anomalies at Zr-Hf and Ti (not shown).

The REE distribution coefficients for coexisting garnet and clinopyroxene porphyroclasts in sheared peridotites from the Premier kimberlite pipe reveal an only subtle offset from equilibrium $^{garnet/cpx}D_{REE}$ values (Fig. 14), which were determined both in

experiments and in natural rocks for ultramafic-mafic silicate and carbonated silicate systems between 920–1600°C and 1.5–10 GPa (Zack *et al.*, 1997; Green *et al.*, 2000; Adam & Green, 2006; Xiong, 2006; Girnis *et al.*, 2013). The offset from equilibrium is larger for garnet–clinopyroxene pairs in the coarse peridotite xenolith CIM15-40. In general, the observed subtle trace element disequilibrium in the Premier peridotite xenoliths, where clinopyroxene is systematically more REE enriched than coexisting garnet, suggests a complex metasomatic history of the central Kaapvaal mantle lithosphere (Simon *et al.*, 2003; Burgess & Harte, 2004), with some enrichment events having occurred only shortly prior to the kimberlite and carbonatite magma eruptions at ca. 1150 Ma.

Garnet $Fe^{3+}/\sum Fe$ compositions and sheared peridotite fO_2

Corrected $Fe^{3+}/\Sigma Fe$ ratios for peridotite-derived garnets range between 0.070–0.088 (Table 1), and these compositions were used to calculate sheared peridotite fO_2 values relative to the FMQ buffer applying the oxybarometer of Stagno et al. (2013). The oxybarometer yielded $\Delta \log fO_2$ [FMQ] values between -2.80 and -2.17 (2S.E. of ±0.5 log units) for five representative sheared peridotite xenoliths from the Premier kimberlite pipe (Fig. 15). Four high-temperature sheared peridotite xenoliths within the pressure range of 5.2–5.5 GPa (1300–1324ºC) are more reduced (-2.80 to -2.47 $\Delta \log fO_2$ units) than the slightly shallower and cooler (~1088ºC) 'megacrystic' sheared peridotite nodule CIM15-35 at ~4.8 GPa, which has the highest $\Delta \log fO_2$ value of FMQ-2.17 (Table 1).

Although this correlation is in alignment with the theoretically expected reduction of peridotite fO_2 with increasing pressure *or* depth (Woodland & Koch, 2003; Frost & McCammon, 2008), the trend observed for the sheared peridotite xenoliths from Premier is shifted by less than 0.5 log units toward slightly more oxidized $\Delta \log fO_2$ values relative to the most reduced garnet peridotite nodules known from the Kaapvaal craton (Fig. 15). The

oxidation state of the Premier sheared peridotites overlaps with fO_2 values for both coarse and sheared peridotites from the diamondiferous lithospheric mantle root of the western Kaapvaal craton (Supplementary Data Appendix B); e.g., from Kimberley and Finsch (Woodland & Koch, 2003; Creighton *et al.*, 2009; Lazarov *et al.*, 2009; Hanger *et al.*, 2015). Importantly, the diamondiferous root of the central Kaapvaal craton, as probed by the sheared garnet peridotite xenoliths from the ca. 1150 Ma Premier kimberlite pipe, is not as highly oxidized as the deformed mantle roots of the Slave (Creighton *et al.*, 2010; Yaxley *et al.*, 2017) and Siberian cratons (Goncharov *et al.*, 2012; Yaxley *et al.*, 2012) (Fig. 15).

Clinopyroxene Sr-Nd-Hf isotopic compositions

Clinopyroxene porphyroclasts separated from five sheared peridotite xenoliths from the Premier kimberlite pipe define a subhorizontal array in Sr-Nd isotope space. The initial $^{87}Sr/^{86}Sr$ and $^{143}Nd/^{144}Nd$ ratios are between 0.703256–0.707224 and 0.511304–0.511334, respectively. Only xenolith CIM15-35 falls off the Sr-Nd isotope array due to elevated initial $^{87}Sr/^{86}Sr$ and $^{143}Nd/^{144}Nd$. The Nd isotopic compositions of the sheared peridotites are moderately depleted as revealed by a narrow range of suprachondritic initial εNd values between +3 and +3.6. For the Premier peridotite xenoliths, we were only able to determine the Hf isotopic composition of clinopyroxene from the sheared sample CIM15-50 at high precision, and the initial εHf value is suprachondritic at +2.1. Coarse peridotite xenolith CIM15-40, which equilibrated at much lower pressure at ~2.8 GPa, has similar initial $^{87}Sr/^{86}Sr$ (0.704973) and $^{143}Nd/^{144}Nd$ (0.511303; equivalent to an initial εNd value of +3) ratios compared with the deeper derived sheared peridotites at 5.2–5.6 GPa (Fig. 16A).

The ten low-Cr clinopyroxene megacrysts from Premier pipe show a similar range of initial $^{87}Sr/^{86}Sr$ (0.702235–0.706073), but a much wider range of initial $^{143}Nd/^{144}Nd$ (0.511223–0.511354; equivalent to an initial εNd range of +1.4 to +4.0) compared to

clinopyroxene hosted in the peridotite xenoliths. The initial $^{176}Hf/^{177}Hf$ compositions of the clinopyroxene megacrysts range between 0.282063–0.282154, which is equivalent to an initial εHf range of +0.2 to +3.4 (Fig. 16B). In Nd-Hf isotope space, the clinopyroxene megacrysts and the only successfully analysed sheared peridotite nodule from Premier pipe fall mostly within the mantle array (initial ΔεHf of -2.6 to -6.9; for definition see footnote to Table 2), in contrast to the more strongly decoupled Nd-Hf isotope systematics of the host Premier kimberlite (initial ΔεHf of -7.6 to -10.7; Tappe et al., 2020b). There is, however, a small overlap between the Nd-Hf isotopic compositions of the clinopyroxene megacrysts and enigmatic carbonatite dykes at Premier pipe (initial ΔεHf of -6.1 to -8.8; Tappe et al., 2020b) (Fig. 16B).

We note that sheared peridotite xenoliths and clinopyroxene megacrysts from the same depth interval at the craton base have similar Sr-Nd isotopic compositions. We note further that clinopyroxene megacrysts from >5.5 GPa contain isotopically more enriched Sr with initial $^{87}Sr/^{86}Sr$ >0.7050 compared to shallower megacrysts, although this trend with depth is less clear for Nd and Hf isotopes (Fig. 17; Table 2).

Calcium isotopic compositions of clinopyroxene and garnet

Aliquots of clinopyroxene sample solutions prepared for Sr-Nd-Hf isotope analytical work were processed and analysed for stable Ca isotopic compositions, expressed here as $\delta^{44/40}Ca$ in per mil relative to SRM-915a (Table 2). We also analysed garnet grains that were left over after Mössbauer spectroscopy Fe^{3+} determinations (see above) for their $\delta^{44/40}Ca$ compositions. Clinopyroxene from five sheared peridotite xenoliths displays a range in $\delta^{44/40}Ca$ values between 0.78–1.00‰ (Fig. 18), and the $\delta^{44/40}Ca$ values for coexisting garnet grains range between 1.06–1.24‰, in excellent agreement with the known clinopyroxene–garnet Ca

isotope equilibrium fractionation of 0.2–0.6‰ at high temperatures (Antonelli *et al.*, 2019; Huang *et al.*, 2019; Wang *et al.*, 2019; Smart *et al.*, 2021a). The coarse peridotite xenolith CIM15-40 contains clinopyroxene and garnet with corresponding $\delta^{44/40}$Ca values of 0.95‰ and 1.87‰, which suggests Ca isotopic disequilibrium for this low-temperature peridotite sample (Table 2). The $\delta^{44/40}$Ca values of the clinopyroxene megacrysts range between 0.72–0.94‰, with exception of crystal CUL17-cpx4, which has a value of 1.38‰ (Fig. 18). We note that deeper derived clinopyroxene megacrysts from >5.5 GPa reveal more notable Ca isotopic heterogeneity compared with the shallower megacrysts (Fig. 17; Table 2). We also analysed fresh bulk rock materials from four kimberlite dykes at Premier pipe for their $\delta^{44/40}$Ca compositions, which show a wide range between 0.73–1.27‰ (Supplementary Data Appendix E).

DISCUSSION: THE DYNAMIC KAAPVAAL CRATON LITHOSPHERE

Sheared peridotite formation across the lithosphere–asthenosphere transition

Petrological and geophysical models often define different depths for the cratonic LAB. Whereas results from seismological methods have frequently suggested craton thicknesses in excess of 250 km (Jordan, 1978; James *et al.*, 2001), geotherms derived from peridotite xenoliths typically project LAB positions between 150–250 km depths (Sleep, 2003; Sand *et al.*, 2009; Mather *et al.*, 2011; Gibson *et al.*, 2013; Kopylova *et al.*, 2019). O'Reilly & Griffin (2010) pointed out that petrological–geochemical methods tend to detect the horizon within the cratonic mantle lithosphere where the shallower depleted mantle transitions into refertilized *or* less depleted portions of a >250 km thick cratonic mantle root, which is strictly speaking not equivalent to the LAB, but conforms to earlier concepts of a mechanical/chemical *versus* a thermal boundary layer (McKenzie & Bickle, 1988). Other

authors also advocated for the existence of much deeper cratonic roots that extend down to 400 km depth approaching the mantle transition zone (Jordan, 1988; Masters *et al.*, 1996). However, recently improved treatments of global seismological datasets suggest that a lithosphere–asthenosphere transition occurs beneath cratons at shallower levels of less than 230 km depth, roughly overlapping the petrologically defined LAB (Mancinelli *et al.*, 2017; Tharimena *et al.*, 2017; Priestley *et al.*, 2019; Rychert *et al.*, 2020).

We derived a refined paleogeotherm of ~40-42 mW/m^2 for the central Kaapvaal craton at ca. 1150 Ma through regression of both previously published and the new P-T data, obtained for both coarse and sheared garnet-facies peridotite xenoliths from Premier pipe (Fig. 5). The P-T array fitting of exclusively coarse peridotite xenoliths resulted in an only marginally cooler steady-state geotherm of ~41 mW/m^2 compared to the regression that incorporated all textural types of garnet-facies peridotite (Fig. 5). The P-T data for discrete clinopyroxene megacrysts independently define a conductive geotherm of 40-41 mW/m^2 (Supplementary Data Figure 2), which is similar to the ~38-40 mW/m^2 geotherm defined by clinopyroxene xenocrysts from the Premier kimberlite (Nimis *et al.*, 2020). Our new ~40-42 mW/m^2 conductive paleogeotherm for the lithospheric mantle column of the central Kaapvaal craton intersects the 1315°C mantle adiabat at approximately 200 km depth, defining the thermal LAB at 1150 Ma (Fig. 5). Adjusting the potential temperature of the ambient upper mantle to 1420°C, as may be more realistic for the convecting mantle during the Proterozoic (Davies, 2009; Ganne & Feng, 2017), increases the thickness of the central Kaapvaal lithosphere to ~225 km at 1150 Ma (Fig. 5), which is in good agreement with the estimate of ~230 km based on single-grain clinopyroxene xenocryst thermobarometry (Nimis *et al.*, 2020). Taking these new estimates of the LAB beneath the central Kaapvaal craton into account, it appears that the sheared peridotites studied here and by Viljoen *et al.* (2009) formed near the craton base in some vertical distance of ~10–50 km above this thermal and

structural/rheological discontinuity. Three of the analysed clinopyroxene megacrysts are derived from ~190–210 km depth suggesting formation at the cratonic LAB, if the 1420°C mantle potential temperature scenario is considered (Fig. 5).

Clinopyroxene megacryst CUL17-cpx4 is anomalous in that it is derived from great depth (~230 km) but records a relatively low temperature of ~1300°C (Fig. 5). Similar P-T systematics corresponding to a ~36-37 mW/m^2 conductive paleogeotherm are reported for some clinopyroxene xenocrysts and a suite of clinopyroxene inclusions in diamond from Premier pipe (Supplementary Data Figure 2). This observation has been tentatively interpreted as a record of deep and old lithospheric mantle that predates Proterozoic thermal perturbations (Nimis *et al.*, 2020). The much less enriched or even depleted trace element composition of CUL17-cpx4 supports this idea; e.g., this megacryst only contains 0.05 ppm Hf (Fig. 9B; Supplementary Data Appendix D). In addition, CUL17-cpx4 has the highest $\delta^{44/40}$Ca value (1.38‰) of the suite analysed (0.72–0.94‰; Fig. 18), and such ^{44}Ca enriched clinopyroxene compositions relative to 'normal' upper mantle are probably a consequence of melt extraction (Chen *et al.*, 2019; Smart *et al.*, 2021a). Thus, the Ca isotopic evidence also supports the presence of remnant deep lithospheric mantle 'pockets' that remained largely unaffected by younger metasomatic (and thermal) events. Such materials may be more common in the lower cratonic mantle lithosphere than is generally accepted, and a few studies suggest indeed that 'kimberlite sampling patterns' are skewed toward metasomatically overprinted mantle rocks and minerals (Malkovets *et al.*, 2007; Artemieva *et al.*, 2019).

A paleogeotherm of ~40-42 mW/m^2 intersects the solidus of CO_2-H_2O-fluxed (Massuyeau *et al.*, 2021) or CO_2-bearing peridotite (Dasgupta & Hirschmann, 2006) between ~130–160 km, which means that small volumes of ephemeral carbonated silicate melts may be ubiquitous at ≥150 km depths at the relatively reducing fO_2 conditions recorded by the

Premier garnet peridotite xenoliths (Stagno *et al.*, 2013) (Fig. 15). The presence of these volatiles and partial melt component (see the melting-induced textures in Figure 4) decreases the viscosity of peridotitic mantle and thus enhances plastic flow and heat transfer (Faul, 1997; Tharimena *et al.*, 2017). Our model suggests that the depth interval between ~150–225 km presents a cratonic lithosphere–asthenosphere transition zone, comparable to the concept of a thermal boundary layer in earlier studies (McKenzie, 1989). Importantly, the majority of the analysed sheared peridotite xenoliths equilibrated between ~170–185 km depth (see also Viljoen *et al.*, 2009), firmly within this boundary layer. The most shallowly derived sheared peridotite xenolith CIM15-35 equilibrated at ~160 km depth in close proximity to the deepest confirmed coarse peridotite sample of Viljoen *et al.* (2009) (Fig. 5). This textural and spatial evidence supports the position of the upper limit of the lithosphere–asthenosphere transition zone as inferred primarily on the basis of petrological constraints.

Baptiste *et al.* (2012) presented OH^- concentration data for olivine from Kaapvaal craton peridotite xenoliths from several kimberlite localities of mainly Mesozoic age. These data demonstrate that the lithospheric mantle at greater than 150 km depth is surprisingly dry compared to the shallower cratonic mantle (Baptiste *et al.*, 2012), a pattern that had previously emerged based on a preliminary dataset for the Kaapvaal craton (Peslier *et al.*, 2010). Although the water systematics of the Kaapvaal lithospheric root are generally opposite to trends observed for other continental mantle columns worldwide (Doucet *et al.*, 2014; Demouchy & Bolfan-Casanova, 2016; Kilgore *et al.*, 2020), experimental data suggest that melt-driven metasomatism in the presence of abundant mixed CO_2-H_2O volatiles results in rather dry olivine compositions (Baptiste *et al.*, 2015) that may subsequently dominate a thermally and chemically overprinted cratonic root. Eaton *et al.* (2009) integrated olivine creep data into thermal models and concluded that if the LAB comprises mainly dry peridotites, then this boundary layer is probably diffuse and >50 km thick. In this scenario

extremely high shear stresses are required to accommodate tectonic plate motion. In contrast, a wet LAB would cause this boundary to be <20 km thick and relatively sharp, with much lower shear stresses caused by the differential motion between the lithospheric plate and the underlying convecting mantle. Relatively dry sheared peridotites from the Premier kimberlite pipe, together with the observations from other localities by Baptiste *et al.* (2012), support a case for a thick and diffuse LAB beneath the Kaapvaal craton at 1150 Ma, where plate tectonic movements may have created a several 10s of kilometers thick deformed layer at the base of the lithosphere.

Some earlier studies of sheared peridotites argued that the high equilibration temperatures and mylonitic microstructures, such as extremely reduced grain sizes and laminated-disrupted porphyroclastic textures, record strain rates that are too high to be explained by mantle flow at the LAB, or plate tectonic movements in general (Green & Gueguen, 1974; Goetze, 1975; Skemer & Karato, 2008; Baptiste *et al.*, 2012). In these studies, sheared peridotite formation at >150 km depth within the lower reaches of cratonic mantle lithosphere had been ascribed to strong plastic deformation associated with ascending kimberlite magma diapirs [see also Gregoire *et al.* (2006) and Arndt *et al.* (2010)]. However, mylonite formation is common in crustal shear zones and thrust faults and can be readily explained by the differential movement of rock packages at strain rates that are comparable to those in the deep continental mantle lithosphere (Le Roux *et al.*, 2008; Lee *et al.*, 2018). We argue that rather than being restricted to a narrow zone at the base of the craton where mantle flow causes viscous drag (Boyd & Nixon, 1975; Kennedy *et al.*, 2002), sheared peridotite formation may occur in localized meter-thick bands spaced out across the entire width of the lithosphere–asthenosphere transition zone between ~150–225 km depth. This idea is supported by the facts that *(1)* sheared peridotites have protoliths that resemble ancient coarse garnet peridotites (Harte, 1977; Walker *et al.*, 1989; Pearson *et al.*, 1995), and *(2)* that such

coarse garnet peridotites occur across a large portion of the Kaapvaal cratonic mantle column from 80 km down to 215 km depth (Katayama *et al.*, 2009; Viljoen *et al.*, 2009; Baptiste *et al.*, 2012). Thus, it is reasonable to assume that relatively undeformed coarse peridotite materials and strongly deformed sheared peridotites are structurally interleaved between ~150–200 km depth, where most of the tectonic strain may be accommodated by a network of relatively narrow subhorizontal shear zones (Fig. 19). It should be noted, however, that modern geobarometry of garnet-bearing peridotites is typically associated with uncertainties of ~0.2-0.4 GPa *or* ±10 km (Mather *et al.*, 2011), such that relative depth distributions of coarse and sheared peridotite varieties as building blocks of cratonic mantle roots cannot be resolved more precisely.

Despite the intense plastic deformation of sheared peridotites under extreme deviatoric stress, most xenoliths of this textural group exhibit a recrystallized olivine-rich matrix that records evidence of effective recovery from strain, such as grain boundary migration under static conditions (e.g., olivine tablet formation; Fig. 4). This evidence for annealing has been used as an argument against a spatial association of sheared peridotites with the cratonic LAB (Baptiste *et al.*, 2012). However, in our model the observed annealing microstructures are readily explained by mantle shear zones going through cycles of intense movement and dormancy (i.e., non-steady state deformation); that is, they are active only intermittently, similar to major shear zones in the Earth's crust (Fossen & Cavalcante, 2017). In other words, we suggest that plate tectonically induced stresses onto the lower cratonic mantle are distributed unevenly (i.e., strain partitioning) over extensive networks of subhorizontal shear bands across the entire ≥50 km thick lithosphere–asthenosphere transition zone (Fig. 5, 19).

The enigmatic connection between sheared peridotites and megacrysts

Although olivine in peridotites from the lower Kaapvaal craton lithosphere appears to have lower OH^- contents than in the shallow cratonic mantle at <150 km depth (Peslier *et al.*, 2010; Baptiste *et al.*, 2012), past activity of fluids and melts in the sheared peridotitic mantle, as probed by the kimberlite-borne xenoliths from Premier pipe derived from ~160–185 km depth, is evidenced by the annealing textures of the olivine-rich matrix. Undeformed mosaic textures, including olivine tablet formation in the matrix of sheared cratonic peridotites (Figs. 3, 4), have been explained by fluid-assisted static recrystallization (Drury & van Roermund, 1989). The former presence of fluid/melt is also recorded in the REE patterns of clinopyroxene in the sheared peridotites and megacrysts from Premier pipe, suggesting a common origin by metasomatic reactions within the lower Kaapvaal craton lithosphere (Fig. 9). This trace element evidence is supported by melting-induced texture development such as the porous tails around and spongy margins along clinopyroxene porphyroclasts in the sheared peridotite xenoliths (Fig. 4).

The Premier paleogeotherm of ~40-42 mW/m^2 intersects the solidus of CO_2-H_2O-bearing (Massuyeau *et al.*, 2021) or CO_2-bearing peridotite (Dasgupta & Hirschmann, 2006) between ~130–160 km depth, which suggests that an influx of CHO volatile mixtures should stabilize low-degree partial melts with carbonate-rich to carbonated silicate compositions at ≥150 km depth (Foley *et al.*, 2009; Aulbach *et al.*, 2017), even under relatively reducing conditions (Stagno & Frost, 2010). Several studies suggest that megacryst suites in kimberlites on cratons worldwide formed from percolating melts within the lower cratonic mantle lithosphere (Hops *et al.*, 1992; Bell & Moore, 2004; Moore & Belousova, 2005; Kopylova *et al.*, 2009; Bussweiler *et al.*, 2018; Cone & Kopylova, 2021). The Premier clinopyroxene megacrysts studied formed over a wide P-T range between ~135–210 km depth

(Fig. 5). In detail, a shallower megacryst subgroup at ~135–150 km depth can be distinguished from a deeper subgroup at ~190–210 km depth. The apparent clustering of clinopyroxene megacrysts near the top and bottom of the central Kaapvaal lithosphere–asthenosphere transition zone may reflect stalling of melt in channels beneath permeability boundaries (e.g., Sleep, 2003; Rychert *et al.*, 2020). Nimis *et al.* (2020) observed a similar bimodal depth distribution for a large clinopyroxene xenocryst suite from Premier pipe that probably comprises a significant portion of fragmented megacrysts. Importantly, the clinopyroxene megacrysts from both depth horizons have similar geochemical and Sr-Nd-Hf isotopic compositions (Figs. 9, 16), which suggests a common melt source and similar magma evolution. We note, however, that the shallower megacryst subgroup shows slightly lower initial $^{87}Sr/^{86}Sr$ and slightly higher initial $^{176}Hf/^{177}Hf$ relative to the deeper clinopyroxene subgroup (Fig. 17; see below). It is noted further that the Ca isotopic compositions of the deepest derived clinopyroxene megacrysts from ~190–210 km depth are more variable compared to their counterparts from mid-lithospheric depth, which exhibit exclusively mantle-like $\delta^{44/40}Ca$ values (Figs. 17B, 18).

Clinopyroxene porphyroclasts in sheared peridotite xenoliths from Premier show a striking overlap with the clinopyroxene megacrysts in terms of major and trace element compositions as well as Sr-Nd-Hf-Ca isotope ratios (Figs. 8, 9, 16, 18). The clinopyroxene porphyroclasts (~160–185 km depth) exhibit the same range of $\delta^{44/40}Ca$ values as their megacrystic counterparts from ~190–210 km depth; i.e., 0.78–1.00‰ and 0.72–0.94‰ $\delta^{44/40}Ca$, respectively (Figs. 17B, 18). These clinopyroxene Ca isotopic compositions are also similar to those of the host kimberlite magmas with $\delta^{44/40}Ca$ values as low as 0.73‰ (Fig. 18; Supplementary Data Appendix E). The clinopyroxene Sr-Nd isotopic compositions from both megacrysts and sheared peridotites are moderately depleted to slightly enriched, overlapping the compositions of kimberlite and carbonatite magmas from Premier pipe (Fig. 16A).

However, in Nd-Hf isotope space there is only a match between the mantle-derived clinopyroxene crystals (megacrysts and sheared peridotite) and carbonatite magmas, falling slightly below the mantle array (Fig. 16B). In contrast, the Premier kimberlites show strong Nd-Hf isotope decoupling significantly below the mantle regression line (Tappe *et al.*, 2020b). Combined, the isotope data reveal that clinopyroxene formation or heavy overprinting by melt/fluid must have been a relatively 'young' event that occurred only shortly prior to kimberlite and carbonatite magmatism on the central Kaapvaal craton at ca. 1150 Ma. The data suggest direct links between passing carbonatitic to kimberlitic melts, localised plastic deformation and clinopyroxene formation during metasomatic reactions within the lower lithospheric mantle, as had been proposed for other regions on the Kaapvaal craton (Gurney & Harte, 1980; Moore & Lock, 2001). Tappe *et al.* (2018a) presented high-precision geochronology data for Premier pipe and suggested that the kimberlite–carbonatite magmatic system was active for >3 million years, which provides ample time for metasomatic overprinting of portions within the lower lithospheric mantle, including megacryst formation. Although vestiges of undisturbed Archean lower cratonic mantle are preserved in some peridotitic clinopyroxene and garnet inclusions in diamonds from Premier pipe showing extremely depleted εNd values of up to +66 (Richardson *et al.*, 1993), no such ancient material has been traced in the formation of metasomatic clinopyroxene within sheared peridotitic mantle and associated megacrysts (Fig. 16). However, clinopyroxene crystal CUL17-cpx4 is anomalous and falls on a relatively cold 36-37 mW/m^2 cratonic geotherm (Fig. 5), similar to several clinopyroxene inclusions in diamond and few clinopyroxene xenocrysts from the Premier kimberlite, which have apparently not adjusted to the elevated heat flow of the central Kaapvaal cratonic mantle root, with values of ~39-42 mW/m^2 at 1150 Ma (Viljoen *et al.*, 2009; Nimis *et al.*, 2020; this study).

To further constrain possible links between clinopyroxene in sheared peridotites and the discrete megacrysts via kimberlitic to carbonatitic melt metasomatism, we calculated the REE contents of hypothetical melts in equilibrium with clinopyroxene (Fig. 9C). Both the effects of carbonate-dominated (cpx/melt partition coefficients from Dasgupta *et al.*, 2009 and Girnis *et al.*, 2013) and carbonated silicate (Keshav *et al.*, 2005) melts at conditions equivalent to those near cratonic LABs are shown in Figure 9C. The reconstructed equilibrium melt compositions that may have been involved in metasomatic clinopyroxene formation are highly enriched in LREE–MREE, with concentration levels up to an order of magnitude higher than in the natural carbonatite and kimberlite dyke magmas known from Premier pipe (Tappe *et al.*, 2020b). The best fit between model and nature is provided by the extremely high LREE–MREE concentrations of saline and high-Mg carbonatitic high-density fluids (HDFs) entrapped in diamonds from lithospheric mantle columns of cratons worldwide (Weiss *et al.*, 2011; Weiss *et al.*, 2018). Hence, carbonatitic to kimberlitic melts plus associated high-density fluids may have been responsible for metasomatic clinopyroxene formation within the lithosphere–asthenosphere transition zone of the central Kaapvaal cratonic root at ca. 1150 Ma.

Several other studies also ascribed metasomatic origins to garnet in cratonic mantle peridotites (Malkovets *et al.*, 2007; Simon *et al.*, 2007; Klein-BenDavid & Pearson, 2009; Chepurov *et al.*, 2019; Kopylova *et al.*, 2019), and the high TiO_2 contents of ≥0.5 wt.% as well as elevated Mg- and Cr-number values of garnet in sheared peridotites from Premier lend support to this idea (Fig. 11). We used a range of equilibrium $^{Grt/Cpx}D$ values for the REE (Zack *et al.*, 1997; Green *et al.*, 2000; Adam & Green, 2006; Xiong, 2006; Girnis *et al.*, 2013) to evaluate trace element equilibrium between metasomatic garnet and clinopyroxene in the sheared peridotite xenoliths from Premier. Our data show that clinopyroxene is slightly more REE enriched than predicted by the composition of coexisting garnet (Fig. 14), which

indicates a subtle trace element disequilibrium between these phases and suggests distinct origins during multiple metasomatic events. The Y-Zr and Zr/Hf-Ti/Eu systematics of garnet in the sheared peridotite xenoliths reveal strong HFSE enrichments at constant and low Zr/Hf (Fig. 13), a geochemical signature that is typically ascribed to silicate melt metasomatism (Griffin & Ryan, 1995; Griffin *et al.*, 2003; Viljoen *et al.*, 2009; Shaikh *et al.*, 2020). High Zr/Hf ratios at low Ti/Eu are observed for garnet in the coarse low-temperature peridotite xenoliths from Premier (Fig. 13B), and this contrasting signature points to carbonate-dominated melt metasomatism of the shallow cratonic mantle beneath Premier pipe (Rudnick *et al.*, 1993; McCoy-West *et al.*, 2015; Shu & Brey, 2015). However, Tappe *et al.* (2017) showed that natural primitive carbonated silicate magmas with up to 25 wt.% CO_2 derived from >200 km depth can be extremely enriched in Ti and Zr, which complicates use of the HFSE systematics of mantle-derived xenoliths in our quest for the nature and origin of metasomatic agents within the lower cratonic lithosphere. For example, both the action of carbonate-dominated (garnet/melt partition coefficients from Dasgupta *et al.*, 2009 and Girnis *et al.*, 2013) and carbonated silicate *or* kimberlitic (Brey *et al.*, 2008) melts at P-T conditions equivalent to those of lower cratonic lithosphere and slightly deeper can explain the observed REE compositions of metasomatic garnet in sheared peridotites from Premier, without involvement of pure silicate melts such as basaltic liquid compositions. Regardless of the exact nature of the garnet-forming metasomatic agent, in the absence of radiogenic isotope data for garnet from the sheared peridotite xenoliths it is impossible to constrain the timing of this mantle enrichment event. However, on the basis of attained major element equilibrium between garnet and clinopyroxene (e.g., Ca isotope equilibrium, compatibility of Fe-Mg exchange temperatures with other thermometer results), but subtle trace element disequilibrium (Fig. 14), it can be inferred that all of these identified metasomatic events

occurred shortly prior to kimberlite magmatism during the Mesoproterozoic (see Jollands *et al.*, 2018).

Bushveld mantle plume impact on the Kaapvaal cratonic root revisited

Several studies link the slightly elevated cratonic geotherm and relatively fertile nature of the central Kaapvaal mantle lithosphere, as probed by the ca. 1150 Ma Premier kimberlite, to the magmatic events associated with the ca. 2056 Ma Bushveld layered mafic–ultramafic intrusion (Danchin, 1979; Griffin *et al.*, 2003; Gregoire *et al.*, 2005; Richardson & Shirey, 2008; Viljoen *et al.*, 2009; Viljoen *et al.*, 2014; Korolev *et al.*, 2018b). However, some of the previously discussed evidence is ambiguous or circumstantial, and simpler explanations exist. Because impingement of the putative Bushveld mantle plume on thick diamondiferous continental lithosphere frequently serves in metallogenesis models (Arndt, 2013; Griffin *et al.*, 2013; Fiorentini *et al.*, 2020), a brief re-examination of this contentious topic in light of our new evidence appears warranted.

For Premier pipe, a high abundance of Ti-rich garnet in sheared peridotite xenoliths (Fig. 11A) and from heavy mineral concentrate has been ascribed previously to melt metasomatism that was potentially related to basaltic magmatism of the Bushveld event (Griffin *et al.*, 2003; Kobussen *et al.*, 2009; Viljoen *et al.*, 2009). New research shows, however, that the parental magmas to the giant Bushveld layered intrusion had a low-Ti komatiitic nature (Wilson, 2012; Maier *et al.*, 2016; Solovova *et al.*, 2021) and were probably incapable of causing the observed Ti-enrichment of the lower cratonic mantle. Instead, our major and trace element results for such metasomatic garnet porphyroclasts show that an origin from carbonated silicate melts, such as kimberlitic liquids, is more likely (see the previous section). Moreover, the observed subtle trace element disequilibrium between metasomatic garnet and clinopyroxene suggests that volatile-driven refertilization events

occurred shortly prior to Mesoproterozoic kimberlite and carbonatite magmatism on the central Kaapvaal craton. Based on the garnet Fe^{3+} compositions, it appears that the oxidative effects of this volatile-rich mantle metasomatism were only minor when compared with the highly oxidized and deformed mantle roots beneath some regions on the Slave and Siberian cratons (Creighton *et al.*, 2010; Goncharov *et al.*, 2012; Yaxley *et al.*, 2012; Yaxley *et al.*, 2017) (Fig. 15). Recently, Moussallam *et al.* (2019) demonstrated the highly oxidized nature of mafic–ultramafic silicate melts from major modern mantle plumes worldwide, which have primary fO_2 values of up to two log units above the FMQ buffer. Several Paleoproterozoic large igneous events were also supplied with magma from relatively oxidized mantle sources (Nicklas *et al.*, 2019). However, the putative Bushveld plume impact on the central Kaapvaal cratonic root left no such anomalous imprint on the lithospheric mantle redox composition. This argument is also consistent with the observation that Premier garnet-facies peridotite xenoliths have similar fO_2 values to deep-sourced peridotite xenolith suites from other regions of southern Africa, which have been more distal to the possible effects of the Bushveld large igneous event at ca. 2056 Ma (Woodland & Koch, 2003; Creighton *et al.*, 2009; Lazarov *et al.*, 2009; Hanger *et al.*, 2015) (Fig. 15). Similar to Premier, these peridotite xenolith suites may also show strong Ti-enrichment (e.g., Rehfeldt *et al.*, 2008).

A frequently cited line of evidence for Fe-Ti-enrichment of the lower Kaapvaal cratonic mantle lithosphere by plume-related mafic–ultramafic Bushveld magmas is the occurrence of so-called ‘igneous textured mantle xenoliths’, which contain biotite and ilmenite (Hoal, 2003). Our own ongoing work on this type of xenolith from the Premier kimberlite pipe shows that the textures and mineral assemblages plus compositions are similar to ultramafic lamprophyre dykes, which are common on the central Kaapvaal craton in the vicinity of the ca. 1400 Ma Pilanesberg alkaline complex (Verwoerd, 2006) (Fig. 1). Hence, it

is doubtful that this xenolith type from Premier has a direct mantle origin and we also challenge the previously inferred connection to Bushveld magmatic activity (cf., Hoal, 2003).

Ernst *et al.* (2018) modelled the thermal impact of sizeable mantle plumes on thick diamond-bearing lithospheres and concluded that excess heat of >150°C above ambient mantle temperature dissipates within approximately 100 million years, after which the pre-plume thermal structure of the affected cratonic mantle would be restored. Hence, it is probable that the thermal effects of the putative Bushveld mantle plume on the central Kaapvaal cratonic root had vanished before the Mesoproterozoic. In other words, the mantle-derived xenoliths and megacrysts brought to surface by the ca. 1150 Ma Premier kimberlite magma eruptions, some 900 million years after the Bushveld event, are highly unlikely to retain a record of this large-scale thermal disturbance. Some of these materials, such as incompatible trace element enriched clinopyroxene megacrysts, may even post-date Bushveld magmatism.

Korolev *et al.* (2018b) determined anomalously high formation and equilibration temperatures of up to 1500°C for olivine inclusions in some lithosphere-derived peridotitic diamonds from Premier. Likewise, some lithosphere-derived eclogitic diamonds also yielded high formation temperatures of up to 1570°C. These high formation temperatures of some diamonds were linked to 'hot' carbon-bearing fluids associated with the putative Bushveld mantle plume (Nimis, 2002; Korolev *et al.*, 2018b). The fact that single mineral inclusions or non-touching inclusion pairs shielded by diamond cannot re-equilibrate to the steady-state thermal conditions of cooling mantle lithosphere suggests indeed that rare vestiges of a Bushveld mantle plume – or of any other known regional large igneous event during the Paleoproterozoic or Neoarchean (Gumsley *et al.*, 2020) – survived within the central Kaapvaal cratonic root. Rhenium depletion model ages between 2.8–1.7 Ga for peridotite

xenoliths from Premier are in agreement with both Neoarchean and Paleoproterozoic overprinting of the cratonic mantle lithosphere (Pearson *et al.*, 1995). However, the thermal, compositional and microstructural records of the sheared peridotite xenoliths and clinopyroxene megacrysts studied relate more plausibly to dynamic processes within the lithosphere–asthenosphere transition zone at ~150–225 km depth beneath the central Kaapvaal craton during the Mesoproterozoic.

Significance for kimberlite and carbonatite magma petrogenesis

The petrogenesis of the Premier kimberlite may hold important clues to the origins and evolution of volatile-rich low-volume melts beneath cratons, because this locality is associated with some of the largest and deepest derived 'sublithospheric' diamonds (Nestola *et al.*, 2018; Smith *et al.*, 2018), and also with one of the most strongly decoupled Nd-Hf isotope signatures identified for mantle-derived magmas (Tappe *et al.*, 2020a). Tappe *et al.* (2020b) used the highly siderophile element systematics of fresh kimberlite and carbonatite dykes from Premier pipe to argue that the observed Nd-Hf isotope decoupling, with initial $\Delta\varepsilon$Hf values as low as -10.7 (Fig. 16B), is probably not created during melt–rock interactions within the peridotite-dominated mantle lithosphere. These authors suggested a primary origin of this feature that either relates to the composition of the convecting mantle source (e.g., presence of ancient recycled oceanic crust components), or to the melting process within the convecting mantle source such as mixing of melt increments derived from a highly heterogeneous domain.

Megacryst formation in the lower cratonic lithosphere has frequently been linked to 'failed' proto-kimberlite magma eruptions (Hops *et al.*, 1992; Moore & Belousova, 2005; Giuliani *et al.*, 2013), and the partially overlapping Sr-Nd-Hf-Pb isotopic compositions between many megacryst suites and their host kimberlites from localities worldwide support

this inference (Nowell *et al.*, 2004; Kopylova *et al.*, 2009; Tappe *et al.*, 2011; Bussweiler *et al.*, 2018). At Premier, the analyzed clinopyroxene megacrysts show significantly less Nd-Hf isotope decoupling than the host kimberlite, with initial ΔεHf values of -2.6 to -6.9 *versus* -7.6 to -10.7, respectively. Importantly, the carbonatite dykes have ΔεHf values of -6.1 to -8.8 and provide a better Nd-Hf isotopic match to the megacrysts and clinopyroxene porphyroclasts of sheared peridotite xenolith CIM15-50 (ΔεHf -4.6), although the clinopyroxene crystals extend the data array toward slightly higher $^{176}Hf/^{177}Hf$ (Fig. 16B). Taken at face value, the Nd-Hf isotope data, together with P-T estimates and trace element compositions (Figs. 5, 9), suggest that the megacrysts formed from percolating carbonate-rich melts near the top and bottom of the lithosphere–asthenosphere transition zone beneath the central Kaapvaal craton at around 1150 Ma. The upward percolating carbonate-rich melts (carbonatitic to proto-kimberlitic?) appear to have interacted with ancient cratonic mantle lithosphere to attain the slightly more radiogenic Hf isotopic compositions measured for some of the shallower clinopyroxene megacrysts from ~135–145 km depth (Fig. 17; Table 2; Supplementary Data Appendix E). The main Hf repositories within Archean cratonic mantle are clinopyroxene and garnet (Griffin *et al.*, 2000), and both peridotitic (Simon *et al.*, 2007; Aulbach *et al.*, 2013; Shu *et al.*, 2019) and eclogitic (Jacob *et al.*, 2005; Aulbach *et al.*, 2007; Schmidberger *et al.*, 2007) assemblages show the high $^{176}Hf/^{177}Hf$ required to explain the small isotopic shifts by subtle interactions between the carbonate-rich melts and depleted ancient cratonic mantle lithosphere (Fig. 16B).

Previous authors also suggested roles for carbonate-rich melts in the origin of clinopyroxene megacrysts (e.g., Cone & Kopylova, 2021), and some workers argued that such carbonated liquids evolve into carbonated silicate magmas of kimberlitic affinity by assimilation processes within the lower cratonic lithosphere (van Achterbergh *et al.*, 2002,

2004; Bussweiler *et al.*, 2016; Bussweiler *et al.*, 2018). In the case of Premier, however, such melt evolution from carbonatitic to kimberlitic would require assimilation of significant amounts of refractory peridotite material that has very low $^{176}Hf/^{177}Hf$, as well as εNd-εHf systematics below the mantle array (Fig. 16B). Cratonic peridotites with εNd-εHf values below the mantle array are volumetrically very minor, and the continental lithospheric mantle reservoir is characterized by strongly depleted Nd-Hf isotopic compositions above the mantle array (Pearson & Wittig, 2014). Hence, we argue that the Premier kimberlite magmas originated as carbonated silicate melts from the >1300ºC warm convecting mantle beneath the >200 km thick continental root, a notion that finds support in the compositions of silicate glass-rich melt inclusions within kimberlite-borne olivine megacrysts derived from the base of the Kaapvaal craton farther south (Howarth & Büttner, 2019). In contrast, the thermal regime of the cooler lithosphere–asthenosphere transition zone between ~150–200 km depth additionally can stabilize relatively 'pure' carbonate melts in the presence of CHO fluid phases (Foley *et al.*, 2009; Massuyeau *et al.*, 2021), but this process requires – at least temporarily – fairly oxidizing mantle redox conditions (Stagno & Frost, 2010; Stagno *et al.*, 2013). Such carbonate-rich melts and associated high-density fluids are extremely mobile and present potent metasomatic agents upon interactions with the lower cratonic mantle lithosphere (Rudnick *et al.*, 1993; Weiss *et al.*, 2011; Kopylova *et al.*, 2021). In conjunction with local melt ponding at permeability boundaries (Rabinowicz *et al.*, 2002), and also during strong shear movements (Katz *et al.*, 2006; Holtzman & Kohlstedt, 2007; Le Roux *et al.*, 2008) (Supplementary Data Figure 1), megacrysts may form from such low-volume carbonate-rich melts by deformation-assisted segregation and channeling within the lower reaches of cratonic lithosphere.

Ubiquitous volatile-rich melts and high-density fluids also contribute to the accommodation of extremely high shear stresses across the lithosphere–asthenosphere

transition zone caused by plate tectonic motions (Tharimena *et al.*, 2017). Hence, low-degree carbonate-rich melts within the lowermost lithosphere may – contrary to previous models (e.g., Tappe *et al.*, 2007; Foley, 2011; Holtzman *et al.*, 2012) – lend overall stability to cratonic mantle keels while they are dragged over the convecting mantle for >2.5 billion years as part of drifting tectonic plates. In other words, the fabrics of and metasomatic imprints on the sheared peridotite xenoliths and clinopyroxene megacrysts entrained by the Premier kimberlite eruptions at ca. 1150 Ma may present snapshots of lithosphere–asthenosphere interactions at the early phase of the 1220–1090 Ma Namaqua–Natal orogeny, during which the Kaapvaal craton was on collision course with several adjacent more juvenile terranes (Jacobs *et al.*, 2008; Spencer *et al.*, 2015; Van Schijndel *et al.*, 2020) (Fig. 1). These deformation events may have also facilitated the creation of new, or the reactivation of existing, translithospheric magma ascent pathways through the central Kaapvaal craton (see Holtzman *et al.*, 2012), along which both kimberlitic and carbonatitic melts were successfully extracted from the lithosphere–asthenosphere boundary over the course of several millions of years (Tappe *et al.*, 2018a; Tappe *et al.*, 2018b).

CONCLUSIONS

- This study shows that strongly deformed and refertilized sheared peridotites occur between ~160–185 km depth beneath the central Kaapvaal craton, falling firmly within a lithosphere–asthenosphere transition zone that reaches from ~150 to ~225 km depth. This ≥50 km thick boundary layer is defined here by intersections of the ~40-42 mW/m^2 Premier paleogeotherm with *(1)* CO_2-H_2O-present solidus curves for peridotite (upper bound), and *(2)* typical mantle adiabats with potential temperatures between 1315 and 1420°C (lower bound).

- At 150–225 km depth, the central Kaapvaal cratonic mantle root should be able to stabilize small volumes of ephemeral carbonate-rich melts and associated high-density fluids, which may be a critical factor in causing diffuse, several 10s of kilometers thick lithosphere–asthenosphere 'transitions' beneath cratons. Permeability contrasts at the top and bottom of the lithosphere–asthenosphere transition zone may cause local ponding of carbonate-rich melts, which can trigger the formation of megacryst suites.

- We suggest that sheared peridotite formation occurs in localized deformation zones spaced out across the entire width of the lithosphere–asthenosphere transition zone between ~150–225 km depth, rather than being restricted to a single thin layer at the craton base where mantle flow causes viscous drag. Thus, plate tectonic stresses acting on the lower cratonic lithosphere may be accommodated by networks of narrow shear zones, which – when active – provide pathways and sinks for percolating volatile-rich melts, linking the formation of megacrysts and sheared peridotites (i.e., deformation-assisted melt segregation).

- The central Kaapvaal cratonic root has frequently been portrayed as thermally and compositionally 'anomalous', and a common explanation is heavy overprinting of the mantle lithosphere during magmatic activity associated with the giant Bushveld layered intrusion at ca. 2056 Ma. However, the vast majority of thermal, compositional and microstructural properties of the lower cratonic mantle beneath the ca. 1150 Ma Premier pipe can be linked to dynamic processes across the ≥50 km thick lithosphere–asthenosphere transition zone, shortly prior to or during Mesoproterozoic kimberlite and carbonatite magmatism. Thus, it is unlikely that after 900 million years the impact of a putative Bushveld mantle plume on the Kaapvaal cratonic root would

still be evident, with the possible exception of 'remnant' high formation temperatures of some lithospheric diamonds that retain a memory of long vanished heat anomalies.

- The Nd-Hf isotopic compositions of the clinopyroxene megacrysts, falling largely within the mantle array, are best explained by an origin from percolating carbonate-rich melts that underwent subtle interactions with ancient depleted cratonic mantle components on their way through the lowermost lithosphere. On the basis of this Nd-Hf isotope evidence, these particular melt–rock interactions cannot transform the observed carbonate-rich liquid compositions into kimberlitic magmas. Thus, the strongly decoupled Nd-Hf isotope systematics of the Premier kimberlite, falling below the mantle array, are consistent with an ultimate magma origin as carbonated silicate melts from deep within the convecting upper mantle, fully compatible with the presence of 'ultradeep' sublithospheric diamonds.

FUNDING

This work was supported by the National Research Foundation (NRF) of South Africa (IPRR grant to ST) and the Geological Society of South Africa (REI grant to ST). The DEEP Research Group at the University of Johannesburg is financially supported by the DSI-NRF CIMERA Centre of Excellence, South Africa. Calcium isotope work in Münster was supported through grant GU1035/10-1 by the German Research Foundation (DFG).

ACKNOWLEDGMENTS

We gratefully acknowledge support of our research on Cullinan Diamond Mine by Petra Diamonds Ltd and the Geological Society of South Africa. Christian Reinke and Bradley Guy are thanked for valuable help with the EPMA and MLA analyses in Johannesburg. This study

has benefited from informal discussions with Fanus Viljoen about the Premier mantle and Jeremie Lehmann about shear zones. Yannick Bussweiler is sincerely thanked for sharing his megacryst database and for discussions pertaining to this topic. The highly constructive criticism and valuable scientific feedback by Maya Kopylova, Alex McCoy-West, Pedro Waterton and an anonymous reviewer are much appreciated. We thank the science editors Tod Waight and Georg Zellmer for consummate handling of the review process.

DATA AVAILABILITY STATEMENT

The data underlying this article are available in the article and in its online supplementary material.

SUPPLEMENTARY DATA

Supplementary data are available at *Journal of Petrology* online.

FIGURE CAPTIONS

Figure 1:

Geological map of southern Africa showing the outline of the Archean Kaapvaal craton and surrounding Proterozoic terranes plus mobile belts (adopted from Tappe *et al.*, 2020b). The 1153.3 ± 5.3 Ma Premier kimberlite pipe (Cullinan Diamond Mine) is located in the Republic of South Africa on the central Kaapvaal craton at the southern margin of the ca. 2056 Ma Bushveld Complex. The ca. 1400 Ma Pilanesberg alkaline complex (PAC) that intrudes the western lobe of the Bushveld Complex, as well as several renowned Group-1 kimberlite localities on and around the Kaapvaal craton, ranging in age between 1835 and 90 Ma, are shown for reference.

Figure 2:

Photographs of representative sheared peridotite xenoliths **(A-C)** and coarse peridotite 'nodule' CIM15-40 **(D)** from the ca. 1150 Ma old Premier kimberlite pipe, Cullinan Diamond Mine, on the central Kaapvaal craton. **Panel A** reveals the contact between sheared peridotite xenolith CIM15-8 and 'Grey' volcaniclastic kimberlite that fills large volumes of the ~32 hectares large Premier diatreme structure (Tappe *et al.*, 2018a). The scale bar in **Panel A** applies to all panels. Ol – olivine, Grt – garnet, Opx – orthopyroxene, Cpx – clinopyroxene.

Figure 3:

(A) Back-scattered electron image map of sheared peridotite xenolith CIM15-24 from the Premier kimberlite pipe at the scale of an entire standard petrographic thin section. The BSE map was created with a FEI Quanta 600F MLA system that is equipped with two Bruker 4010 Xflash X-ray detectors. The laminated and disrupted peridotite fabric with isolated garnet–orthopyroxene porphyroclasts set in a matrix of olivine neoblasts can be identified. Note at the image centre the coarser olivine porphyroclasts that underwent grain-size-reduction and neoblast formation along their margins. **(B-C)** Photomicrographs of sheared peridotite xenoliths from Premier pipe under plane-polarized light. Note the strong ductile deformation textures with development of recrystallization tails that can be used as kinematic shear-sense indicators. Note further touching relationships between coexisting garnet and orthopyroxene grains enabling pressure estimations based on Al-exchange. The scale bar in **Panel B** also applies to **Panel C**. Ol – olivine, Grt – garnet, Opx – orthopyroxene, Cpx – clinopyroxene, alt – alteration (e.g., kelyphite).

Figure 4:

Back-scattered electron images **(A-E)** of sheared peridotite xenoliths recovered from the Premier kimberlite pipe, Cullinan Diamond Mine, in South Africa. **(A)** Stretched clinopyroxene porphyroclast with a spongy-textured halo and fine-grained recrystallization tail engulfed by a matrix that is dominated by olivine neoblasts. **(B)** Touching pair of garnet and orthopyroxene as part of a porphyroclast set within a fine-grained matrix that consists mainly of neoblastic olivine including undeformed euhedral 'tablets'. **(C)** Laminated–disrupted porphyroclastic texture of sheared peridotite xenolith ST16-CUL26 showing a tightly folded clinopyroxene crystal at the image centre. The image is a composite comprising four individual BSE images taken at the smallest possible magnification. **(D)** Touching pair of garnet and orthopyroxene as part of a porphyroclast set within a fine-grained olivine matrix. Note the significant grain-size-reduction and neoblast formation that affected the larger olivine crystal enclosed by porphyroclastic orthopyroxene. **(E)** Relatively small orthopyroxene porphyroclast with a diffuse melting-induced clinopyroxene halo 'floating' within a neoblastic olivine matrix. Ol – olivine, Grt – garnet, Opx – orthopyroxene, Cpx – clinopyroxene.

Figure 5:

Pressure–temperature systematics of peridotite xenoliths and Cr-poor clinopyroxene megacrysts from the Premier kimberlite pipe, Cullinan Diamond Mine (all data are listed in Table 1 and Supplementary Data Appendix E). The 'Premier' paleogeotherm (thick solid red curve) was obtained by regression of P-T data for the here investigated and previously reported coarse and sheared / 'deformed' peridotite xenoliths using *FITPLOT*. The long-dashed red curve represents geotherm fitting that included only coarse peridotite xenoliths. All xenolith data, including those from Viljoen *et al.* (2009), are calculated or recalculated

using the preferred *TNG* thermobarometer combination (Nickel & Green, 1985; Taylor, 1998). The P-T data for discrete clinopyroxene megacrysts were calculated according to Nimis & Taylor (2000), but are not included into the displayed geotherm fitting (outlier CUL17-cpx4 is discussed in the main text). The brown field for rare 'cold' clinopyroxene xenocrysts and inclusions in some Premier diamonds is based on the data reported in Nimis *et al.* (2020) (the complete clinopyroxene P-T dataset is displayed in Supplementary Data Figure 2). The graphite/diamond phase transition curve of Day (2012) and conductive model geotherms from Hasterok & Chapman (2011) are shown for reference. The CO_2-H_2O-present peridotite solidus curve is adopted from Foley *et al.* (2009) and has been extrapolated beyond 6 GPa applying the data compilations for high-P melting experiments in Tappe *et al.* (2018b) and Massuyeau *et al.* (2021). Adiabats for ambient mantle potential temperatures of 1315, 1360 and 1420ºC are shown together with corresponding estimations of the petrological lithosphere–asthenosphere boundary (LAB) beneath the central Kaapvaal craton at ca. 1150 Ma. The blue vertical bar indicates the depth location of a lithosphere–asthenosphere transition zone (LAT), in which low-degree carbonate-rich melts may be ubiquitous (see main text).

Figure 6:

Average forsterite contents *versus* corresponding olivine modal abundances of sheared and coarse garnet-facies peridotite xenoliths from the Premier kimberlite pipe, Cullinan Diamond Mine (all data are listed in Supplementary Data Appendix D, E). For the sheared peridotite xenoliths from Premier, both porphyroclastic and neoblastic 'matrix' olivine compositions are shown, without discernable differences in their Mg-numbers within a single nodule. The field for olivine inclusions within Premier diamonds is based on data presented in Viljoen *et al.* (2014) and Korolev *et al.* (2018b), with the mean forsterite content shown as an 'X'. Fields

for low- and high-temperature peridotite xenoliths from the Kaapvaal and Zimbabwe cratons are adopted from van der Meer *et al.* (2013). Averages for low-temperature peridotites from the Kaapvaal craton *(golden star 1)* and other major cratons worldwide *(red star 2)*, as well as for modern abyssal peridotites *(green star 3)*, are taken from Pearson & Wittig (2014). Olivine in sheared peridotites from Premier pipe and other kimberlite occurrences on the Kaapvaal craton resembles olivine from abyssal peridotites of the modern ocean basins, as is also apparent from the proximity to the 'oceanic melting trend' of Boyd (1989).

Figure 7:

Chondrite normalized REE distributions for orthopyroxene in sheared and coarse peridotite xenoliths from the Premier kimberlite pipe, Cullinan Diamond Mine (all data are listed in Supplementary Data Appendix D). The REE patterns for orthopyroxene in garnet-facies peridotite xenoliths derived from ca. 90 Ma old kimberlite pipes of Lesotho and Kimberley on the Kaapvaal craton *(grey squares)* are shown for reference (Simon *et al.*, 2003, 2007). Chondrite values for normalization are from Palme & Jones (2003).

Figure 8:

TiO_2 **(A)** and Cr_2O_3 **(B)** contents *versus* Mg-number for clinopyroxene in sheared and coarse peridotite xenoliths, as well as Cr-poor clinopyroxene megacrysts, from the Premier kimberlite pipe, Cullinan Diamond Mine (all data are listed in Supplementary Data Appendix D). Premier pipe literature data for clinopyroxene from sheared *(filled black circles)* and coarse *(open black circles)* peridotite xenoliths are taken from Viljoen *et al.* (2009). The data compilation for clinopyroxene megacrysts from kimberlite localities worldwide is based on Bussweiler *et al.* (2018). The field for clinopyroxene compositions in metasomatized peridotite xenoliths from cratons worldwide is based on data provided by Kopylova *et al.*

(1999), Simon *et al.* (2003, 2007), Aulbach *et al.* (2007), Rehfeldt *et al.* (2008), Kargin *et al.* (2017), and Bussweiler *et al.* (2018).

Figure 9:

Chondrite normalized REE distributions for clinopyroxene in sheared and coarse peridotite xenoliths **(A)** and for Cr-poor clinopyroxene megacrysts **(B)** from the Premier kimberlite pipe, Cullinan Diamond Mine (all data are listed in Supplementary Data Appendix D). **(C)** Reconstructed equilibrium melt compositions that may have been responsible for the metasomatic nature of clinopyroxene in garnet-facies peridotite xenoliths from the Premier kimberlite pipe, and may have also caused clinopyroxene megacryst formation. Both the effects of 'carbonate-dominated' (cpx/melt partition coefficients from Dasgupta *et al.*, 2009 and Girnis *et al.*, 2013) and 'carbonated silicate' (Keshav *et al.*, 2005) melts at P-T conditions equivalent to the lithosphere–asthenosphere boundary beneath the central Kaapvaal craton are shown. Average kimberlite (red line) and carbonatite (blue line) dyke compositions from Premier pipe are based on the data presented in Tappe *et al.* (2020b). The extremely high LREE–MREE concentrations of saline and high-Mg carbonatitic high-density fluids (HDFs) entrapped in diamonds from lithospheric mantle columns of cratons worldwide (Weiss *et al.*, 2011, 2018) suggest their possible involvement in the origin of enriched clinopyroxene signatures within the Kaapvaal continental root. The REE patterns for clinopyroxene from garnet-facies peridotite xenoliths of the Kimberley kimberlite cluster on the western Kaapvaal craton *(grey lines)* are shown for reference in **Panels A-B-C** (Simon *et al.*, 2007). Chondrite values for normalization are from Palme & Jones (2003).

Figure 10:

Cr_2O_3 *versus* CaO contents (wt.%) of garnet in sheared and coarse peridotite xenoliths from the Premier kimberlite pipe, Cullinan Diamond Mine (all data are listed in Supplementary Data Appendix D). The garnet 'G-type' classification and the 'graphite–diamond constraint' are according to Grütter *et al.* (2004). Literature data for garnet from sheared *(filled black circles)* and coarse *(open black circles)* peridotite xenoliths, as well as from diamond inclusions *(filled grey diamond symbol)* are taken from Viljoen *et al.* (2009) and Viljoen *et al.* (2014), respectively. Note the partial overlap between G9 lherzolitic garnet grains from Premier pipe and the compositional field of G1 low-Cr garnet megacrysts.

Figure 11:

TiO_2 content **(A)** and Cr-number **(B)** *versus* Mg-number for garnet in sheared and coarse peridotite xenoliths from the Premier kimberlite pipe, Cullinan Diamond Mine (all data are listed in Supplementary Data Appendix D). Premier pipe literature data for garnet from sheared *(filled black circles)* and coarse *(open black circles)* peridotite xenoliths, as well as from diamond inclusions *(filled grey diamond symbol)* are taken from Viljoen *et al.* (2009) and Viljoen *et al.* (2014), respectively. The data compilation for garnet megacrysts from localities worldwide is based on Bussweiler *et al.* (2018), and dominated by southern African occurrences for the low-Cr suite *(filled dark grey circles)*, as opposed to occurrences located mainly on the Slave craton in Canada for the high-Cr megacrysts *(filled light grey circles)*. The field for garnet compositions from metasomatized peridotite xenoliths of the Kaapvaal craton is based on data compiled in Bussweiler *et al.* (2018).

Figure 12:

(A) Chondrite normalized REE distributions for garnet in sheared and coarse peridotite xenoliths from the Premier kimberlite pipe, Cullinan Diamond Mine (all data are listed in Supplementary Data Appendix D). Premier pipe literature data for garnet from sheared / deformed and coarse peridotite xenoliths *(grey lines)* are taken from Viljoen *et al.* (2009) and display both 'normal' and 'sinusoidal' patterns. **(B)** Reconstructed equilibrium melt compositions that may have been responsible for the metasomatic nature of garnet in peridotite xenoliths from the Premier kimberlite pipe. Both the effects of 'carbonate-dominated' (garnet/melt partition coefficients from Dasgupta *et al.*, 2009 and Girnis *et al.*, 2013) and 'carbonated silicate' (Brey *et al.*, 2008) melts at P-T conditions equivalent to the lithosphere–asthenosphere boundary beneath the central Kaapvaal craton are shown. Data for fresh kimberlite (red lines) and carbonatite (blue lines) dykes from Premier pipe are from Tappe *et al.* (2020b). Chondrite values for normalization are from Palme & Jones (2003).

Figure 13:

(A) Y *versus* Zr contents, and **(B)** Zr/Hf *versus* Ti/Eu ratios of garnet in sheared and coarse peridotite xenoliths from the Premier kimberlite pipe, Cullinan Diamond Mine (all data are listed in Supplementary Data Appendix D). Premier pipe literature data for garnet from sheared *(filled black circles)* and coarse *(open black circles)* peridotite xenoliths, as well as from diamond inclusions *(filled grey diamond symbol)* are taken from Viljoen *et al.* (2009) and Viljoen *et al.* (2014), respectively. Data for fresh kimberlite *(filled grey triangle)* and carbonatite *(filled grey inverted triangle)* dykes from Premier pipe are from Tappe *et al.* (2020b). The layout of **Panel A** is adopted from Griffin & Ryan (1995), with some modification to the metasomatic trend. The layout of **Panel B** is adopted from Shu & Brey (2015), with modifications of the metasomatic trends. Note that the Ti/Eu values have been

divided by a hundred for simplicity's sake. Primitive mantle composition is from Palme & O'Neill (2003).

Figure 14:

REE distribution coefficients (chondrite-normalized, Palme & Jones, 2003) for coexisting garnet and clinopyroxene in sheared and coarse peridotite xenoliths from the Premier kimberlite pipe, Cullinan Diamond Mine (all data are listed in Supplementary Data Appendix D). A range of equilibrium $^{Grt/Cpx}D$ values determined either experimentally (Green *et al.*, 2000; Adam & Green, 2006; Xiong, 2006; Girnis *et al.*, 2013) or on natural rocks (Zack *et al.*, 1997) is shown for comparison, indicating trace element equilibrium to subtle disequilibrium for the Premier sheared peridotite xenoliths, and notable LREE disequilibrium for coarse peridotite sample CIM15-040. For this sample, clinopyroxene is more LREE enriched than predicted by the composition of coexisting garnet.

Figure 15:

The pressure *versus* $\Delta\log fO_2$ systematics (relative to the FMQ buffer) of sheared garnet peridotite xenoliths from the Premier kimberlite pipe, Cullinan Diamond Mine (all data are listed in Table 1 and Supplementary Data Appendix E). The error bars entail the 2S.E. uncertainties of the fO_2 calculations using the formulation by Stagno *et al.* (2013) and an estimated uncertainty of 0.2 GPa for pressure calculations using the calibration by Nickel & Green (1985). The previously published data for garnet peridotite xenoliths from the Kaapvaal (Woodland & Koch, 2003; Creighton *et al.*, 2009; Lazarov *et al.*, 2009; Hanger *et al.*, 2015), Slave (Creighton *et al.*, 2010; Yaxley *et al.*, 2017) and Siberian (Goncharov *et al.*, 2012; Yaxley *et al.*, 2012) cratons are recalculated using the Stagno *et al.* (2013) and Nickel & Green (1985) methods for fO_2 and pressure estimations, respectively (Supplementary Data

Appendix B). The graphite/diamond phase transition and graphite/diamond *versus* carbonate stability reaction in a peridotitic system [EMOG/D] at cratonic thermal conditions are adopted from Yaxley *et al.* (2017).

Figure 16:

Initial εNd *versus* $^{87}Sr/^{86}Sr$ **(A)** and εHf *versus* εNd **(B)** for clinopyroxene from sheared and coarse peridotite xenoliths, as well as for discrete Cr-poor clinopyroxene megacrysts from the Premier kimberlite pipe, Cullinan Diamond Mine (all data are listed in Table 2 and Supplementary Data Appendix E). Published data for Cr-poor megacrysts (cpx – clinopyroxene, grt – garnet, ilm – ilmenite) from Premier pipe are taken from Nowell *et al.* (2004). The data for Premier kimberlite and carbonatite dykes are from Tappe *et al.* (2020b). In **Panel A**, the Sr-Nd isotope data for clinopyroxene and garnet inclusions within peridotitic diamonds from Premier pipe (Richardson *et al.*, 1993), the ca. 1400 Ma Pilanesberg alkaline complex (Cawthorn *et al.*, 2012), and basaltic lavas from the Rooiberg Group of the ca. 2056 Ma Bushveld Complex on the central Kaapvaal craton (Günther *et al.*, 2018) are shown for comparison. All data in **Panel A** and **B** are corrected to the kimberlite magma emplacement age of ca. 1150 Ma for Premier pipe (Tappe *et al.*, 2018a) and they entail a full propagation of uncertainties shown by the error bars (see Methods and the footnote to Table 2). In **Panel B**, the 'mantle array' is after Chauvel *et al.* (2008) and the vectors pointing toward depleted ancient cratonic mantle peridotites are after Tappe *et al.* (2020b).

Figure 17:

Initial $^{87}Sr/^{86}Sr$ **(A)**, $\delta^{44/40}Ca$ **(B)**, initial $^{176}Hf/^{177}Hf$ **(C)**, and initial ΔεHf **(D)** compositions *versus* the equilibration depths of clinopyroxene porphyroclasts from sheared peridotite xenoliths and of discrete clinopyroxene megacrysts from the Premier kimberlite pipe,

Cullinan Diamond Mine (all data are listed in Supplementary Data Appendix E). No hafnium isotope data are available for megacryst CUL17-cpx4 due to its very low Hf concentration. The upper mantle $\delta^{44/40}$Ca composition is after Chen *et al.* (2019).

Figure 18:

The $\delta^{44/40}$Ca values for clinopyroxene from sheared and coarse peridotite xenoliths, as well as for discrete Cr-poor clinopyroxene megacrysts from the Premier kimberlite pipe, Cullinan Diamond Mine, reported relative to SRM-915a (all data are listed in Table 2 and Supplementary Data Appendix E). The Ca isotopic compositions of four kimberlite dykes from Premier pipe have also been analysed for comparative purposes. Published $\delta^{44/40}$Ca data for relevant rock types and geochemical reservoirs are taken from the following literature sources and compilations (averages ± 2S.D.): continental peridotite xenoliths (Kang *et al.*, 2017), cratonic eclogites/pyroxenites (Smart *et al.*, 2021), modern oceanic basalts (Schiller *et al.*, 2016; Chen *et al.*, 2019), modern to 3 Ga old Ca-Mg-Fe carbonatites (Amsellem *et al.*, 2020; Sun *et al.*, 2021) and 1-3 Ga old Precambrian marine carbonates (Blättler & Higgins, 2017). The average $\delta^{44/40}$Ca value for the upper mantle of 0.94 ± 0.1‰ (dashed vertical line plus error envelop) is based on Chen *et al.* (2019).

Figure 19:

Schematic model of the central Kaapvaal cratonic mantle lithosphere during the ca. 1150 Ma kimberlite and carbonatite magma eruptions at Premier/Cullinan. This study proposes a ≥50 km thick lithosphere–asthenosphere transition zone between ~150-225 km depth, where strong plastic deformation creates a network of narrow subhorizontal shear zones as represented by abundant sheared peridotite xenoliths. Stress-driven segregation of percolating carbonate-rich melts may provide a link between the common association of megacrysts and

sheared peridotites as part of kimberlite mantle cargo. Both lithospheric and sublithospheric (i.e., 'ultradeep') diamonds are shown for reference, but they are not discussed in detail as part of this model. CLM – cratonic lithospheric mantle, LAB – lithosphere–asthenosphere boundary.

SUPPLEMENTARY DATA FILES

Supplementary Data Appendix A

LA-ICP-MS trace element results for in-house garnet standard GHR-1 and clinopyroxene standard KBY17-cpx4.

Supplementary Data Appendix B

Recalculated oxygen fugacity data for garnet peridotite xenoliths from literature sources as used in this study for comparison (see Figure 15).

Supplementary Data Appendix C

Comparison of pressure–temperature results obtained with different thermobarometer combinations.

Supplementary Data Appendix D

Complete major and trace element dataset for minerals analysed in-situ during this study.

Supplementary Data Appendix E

Combined petrology and Sr-Nd-Hf-Ca isotope dataset for minerals analysed during this study (Table 1 & 2 of the main article).

Supplementary Data Figure 1

Clinopyroxene megacryst formation (melt pool) within sheared peridotite xenolith CIM15-50.

Supplementary Data Figure 2

FITPLOT P-T data arrays for mantle-derived materials from the Premier kimberlite (this study and literature sources).

REFERENCES

Adam, J. & Green, T. H. (2006). Trace element partitioning between mica- and amphibole-bearing garnet lherzolite and hydrous basanitic melt: 1. Experimental results and the investigation of controls on partitioning behaviour. *Contributions to Mineralogy and Petrology* **152**, 1-17.

Agashev, A. M., Ionov, D. A., Pokhilenko, N. P., Golovin, A. V., Cherepanova, Y. & Sharygin, I. S. (2013). Metasomatism in lithospheric mantle roots: Constraints from whole-rock and mineral chemical composition of deformed peridotite xenoliths from kimberlite pipe Udachnaya. *Lithos* **160**, 201-215.

Allegre, C. J., Shimizu, N. & Rousseau, D. (1982). History of the continental lithosphere recorded by ultramafic xenoliths. *Nature* **296**, 732-735.

Amsellem, E., Moynier, F., Bertrand, H., Bouyon, A., Mata, J., Tappe, S. & Day, J. M. D. (2020). Calcium isotopic evidence for the mantle sources of carbonatites. *Science Advances* **6**, eaba3269.

Antonelli, M. A., Schiller, M., Schauble, E. A., Mittal, T., DePaolo, D. J., Chacko, T., Grew, E. S. & Tripoli, B. (2019). Kinetic and equilibrium Ca isotope effects in high-T rocks and minerals. *Earth and Planetary Science Letters* **517**, 71-82.

Arndt, N. T., Guitreau, M., Boullier, A. M., le Roex, A. P., Tommasi, A., Cordier, P. & Sobolev, A. V. (2010). Olivine, and the origin of kimberlite. *Journal of Petrology* **51**, 573-602.

Arndt, N. T. (2013). The lithospheric mantle plays no active role in the formation of orthomagmatic ore deposits. *Economic Geology* **108**, 1953-1970.

Artemieva, I. M. & Mooney, W. D. (2001). Thermal thickness and evolution of Precambrian lithosphere: A global study. *Journal of Geophysical Research* **106**, 16387-16414.

Artemieva, I. M., Thybo, H. & Cherepanova, Y. (2019). Isopycnicity of cratonic mantle restricted to kimberlite provinces. *Earth and Planetary Science Letters* **505**, 13-19.

Aulbach, S., Pearson, N. J., O'Reilly, S. Y. & Doyle, B. J. (2007). Origins of xenolithic eclogites and pyroxenites from the central Slave craton, Canada. *Journal of Petrology* **48**, 1843-1873.

Aulbach, S. (2012). Craton nucleation and formation of thick lithospheric roots. *Lithos* **149**, 16-30.

Aulbach, S., Griffin, W. L., Pearson, N. J. & O'Reilly, S. Y. (2013). Nature and timing of metasomatism in the stratified mantle lithosphere beneath the central Slave craton (Canada). *Chemical Geology* **352**, 153-169.

Aulbach, S. & Viljoen, K. S. (2015). Eclogite xenoliths from the Lace kimberlite, Kaapvaal craton: From convecting mantle source to palaeo-ocean floor and back. *Earth and Planetary Science Letters* **431**, 274-286.

Aulbach, S., Massuyeau, M. & Gaillard, F. (2017). Origins of cratonic mantle discontinuities: A view from petrology, geochemistry and thermodynamic models. *Lithos* **268**, 364-382.

Baptiste, V., Tommasi, A. & Demouchy, S. (2012). Deformation and hydration of the lithospheric mantle beneath the Kaapvaal craton, South Africa. *Lithos* **149**, 31-50.

Baptiste, V., Demouchy, S., Keshav, S., Parat, F., Bolfan-Casanova, N., Condamine, P. & Cordier, P. (2015). Decrease of hydrogen incorporation in forsterite from CO2-H2O-rich kimberlitic liquid. *American Mineralogist* **100**, 1912-1920.

Bell, D. R., Schmitz, M. D. & Janney, P. E. (2003). Mesozoic thermal evolution of the southern African mantle lithosphere. *Lithos* **71**, 273-287.

Bell, D. R. & Moore, R. O. (2004). Deep chemical structure of the southern African mantle from kimberlite megacrysts. *South African Journal of Geology* **107**, 59-80.

Bernstein, S., Kelemen, P. B. & Hanghøj, K. (2007). Consistent olivine Mg# in cratonic mantle reflects Archean mantle melting to the exhaustion of orthopyroxene. *Geology* **35**, 459-462.

Beyer, C., Berndt, J., Tappe, S. & Klemme, S. (2013). Trace element partitioning between perovskite and kimberlite to carbonatite melt: New experimental constraints. *Chemical Geology* **353**, 132-139.

Blättler, C. L. & Higgins, J. A. (2017). Testing Urey's carbonate-silicate cycle using the calcium isotopic composition of sedimentary carbonates. *Earth and Planetary Science Letters* **479**, 241-251.

Blichert-Toft, J., Chauvel, C. & Albarede, F. (1997). Separation of Hf and Lu for high-precision isotope analysis of rock samples by magnetic sector-multiple collector ICP-MS. *Contributions to Mineralogy and Petrology* **127**, 248-260.

Bokelmann, G. H. R. (2002). Which forces drive North America? *Geology* **30**, 1027-1030.

Bokelmann, G. H. R. & Silver, P. G. (2002). Shear stress at the base of shield lithosphere. *Geophysical Research Letters* **29**, 1-4.

Bouvier, A., Vervoort, J. D. & Patchett, P. J. (2008). The Lu-Hf and Sm-Nd isotopic composition of CHUR: Constraints from unequilibrated chondrites and implications for the bulk composition of terrestrial planets. *Earth and Planetary Science Letters* **273**, 48-57.

Boyd, F. R. & Nixon, P. H. (1975). Origins of the ultramafic nodules from some kimberlites of northern Lesotho and the Monastery Mine, South Africa. *Physics and Chemistry of the Earth* **9**, 431-454.

Boyd, F. R., Gurney, J. J. & Richardson, S. H. (1985). Evidence for a 150-200 km thick Archaean lithosphere from diamond inclusion thermobarometry. *Nature* **315**, 387-389.

Boyd, F. R. (1989). Compositional distinction between oceanic and cratonic lithosphere. *Earth and Planetary Science Letters* **96**, 15-26.

Brey, G. P. & Köhler, T. (1990). Geothermobarometry in four-phase lherzolites II. New thermobarometers, and practical assessment of existing thermobarometers. *Journal of Petrology* **31**, 1353-1378.

Brey, G. P., Bulatov, V. K., Girnis, A. V. & Lahaye, Y. (2008). Experimental melting of carbonated peridotite at 6-10 GPa. *Journal of Petrology* **49**, 797-821.

Burgess, S. R. & Harte, B. (2004). Tracing lithosphere evolution through the analysis of heterogeneous G9-G10 garnets in peridotite xenoliths, II: REE chemistry. *Journal of Petrology* **45**, 609-634.

Burness, S., Smart, K. A., Tappe, S., Stevens, G., Woodland, A. B. & Cano, E. (2020). Sulphur-rich mantle metasomatism of Kaapvaal craton eclogites and its role in redox-controlled platinum group element mobility. *Chemical Geology* **542**, 1-22.

Bussweiler, Y., Stone, R. S., Pearson, D. G., Luth, R. W., Stachel, T., Kjarsgaard, B. A. & Menzies, A. (2016). The evolution of calcite-bearing kimberlites by melt-rock reaction: Evidence from polymineralic inclusions within clinopyroxene and garnet megacrysts from Lac de Gras kimberlites, Canada. *Contributions to Mineralogy and Petrology* **171**, 1-25.

Bussweiler, Y., Pearson, D. G., Stachel, T. & Kjarsgaard, B. A. (2018). Cr-rich megacrysts of clinopyroxene and garnet from Lac de Gras kimberlites, Slave Craton, Canada – implications for the origin of clinopyroxene and garnet in cratonic lherzolites. *Mineralogy and Petrology* **112**, 583–596.

Cammarano, F. (2013). A short note on the pressure-depth conversion for geophysical interpretation. *Geophysical Research Letters* **40**, 4834-4838.

Carlson, R. W., Pearson, D. G. & James, D. E. (2005). Physical, chemical, and chronological characteristics of continental mantle. *Reviews of Geophysics* **43**, 1-24.

Cawthorn, R. G., Ellam, R. M., Ashwal, L. D. & Webb, S. J. (2012). A clinopyroxenite intrusion from the Pilanesberg Alkaline Province, South Africa. *Precambrian Research* **198**, 25-36.

Chauvel, C., Lewin, E., Carpentier, M., Arndt, N. T. & Marini, J. C. (2008). Role of recycled oceanic basalt and sediment in generating the Hf-Nd mantle array. *Nature Geoscience* **1**, 64-67.

Chauvel, C., Bureau, S. & Poggi, C. (2011). Comprehensive chemical and isotopic analyses of basalt and sediment reference materials. *Geostandards and Geoanalytical Research* **35**, 125-143.

Chen, C., Dai, W., Wang, Z., Liu, Y., Li, M., Becker, H. & Foley, S. F. (2019). Calcium isotope fractionation during magmatic processes in the upper mantle. *Geochimica Et Cosmochimica Acta* **249**, 121-137.

Chepurov, A. A., Faryad, S. W., Agashev, A. M., Strnad, L., Jedlicka, R., Turkin, A. I., Mihaljevic, M. & Lin, V. V. (2019). Experimental crystallization of a subcalcic Cr-rich pyrope in the presence of REE-bearing carbonatite. *Chemical Geology* **509**, 103-114.

Cone, D. & Kopylova, M. G. (2021). Origin of megacrysts by carbonate-bearing metasomatism: A case study for the Muskox kimberlite, Slave craton, Canada. *Journal of the Geological Society* **178**, 1-20.

Conrad, C. P. & Lithgow-Bertelloni, C. (2006). Influence of continental roots and asthenosphere on plate-mantle coupling. *Geophysical Research Letters* **33**, 1-4.

Creighton, S., Stachel, T., Matveev, S., Höfer, H., McCammon, C. & Luth, R. W. (2009). Oxidation of the Kaapvaal lithospheric mantle driven by metasomatism. *Contributions to Mineralogy and Petrology* **157**, 491-504.

Creighton, S., Stachel, T., Eichenberg, D. & Luth, R. W. (2010). Oxidation state of the lithospheric mantle beneath Diavik diamond mine, central Slave craton, NWT, Canada. *Contributions to Mineralogy and Petrology* **159**, 645-657.

Danchin, R. V. (1979). Mineral and bulk chemistry of garnet lherzolite and garnet harzburgite xenoliths from the Premier Mine, South Africa. In: Boyd, F. R. & Meyer, H. O. A. (eds.) *The mantle sample: Inclusions in kimberlites and other volcanics*. Washington D.C.: American Geophysical Union, 104-126.

Dasgupta, R. & Hirschmann, M. M. (2006). Melting in the Earth's deep upper mantle caused by carbon dioxide. *Nature* **440**, 659-662.

Dasgupta, R., Hirschmann, M. M., McDonough, W. F., Spiegelman, M. & Withers, A. C. (2009). Trace element partitioning between garnet lherzolite and carbonatite at 6.6 and 8.6 GPa with applications to the geochemistry of the mantle and of mantle-derived melts. *Chemical Geology* **262**, 57-77.

Davies, G. F. (2009). Effect of plate bending on the Urey ratio and the thermal evolution of the mantle. *Earth and Planetary Science Letters* **287**, 513-518.

Day, H. W. (2012). A revised diamond-graphite transition curve. *American Mineralogist* **97**, 52-62.

de Wit, M. C. J., Bhebhe, Z., Davidson, J., Haggerty, S. E., Hundt, P., Jacob, J., Lynn, M., Marshall, T. R., Skinner, C., Smithson, K., Stiefenhofer, J., Robert, M., Revitt, A., Spaggiari, R. & Ward, J. (2016). Overview of diamond resources in Africa. *Episodes* **39**, 199-237.

de Wit, M. J., Roering, C., Hart, R. J., Armstrong, R. A., Deronde, C. E. J., Green, R. W. E., Tredoux, M., Peberdy, E. & Hart, R. A. (1992). Formation of an Archean continent. *Nature* **357**, 553-562.

Demouchy, S. & Bolfan-Casanova, N. (2016). Distribution and transport of hydrogen in the lithospheric mantle: A review. *Lithos* **240**, 402-425.

Doucet, L. S., Ionov, D. A. & Golovin, A. V. (2013). The origin of coarse garnet peridotites in cratonic lithosphere: New data on xenoliths from the Udachnaya kimberlite, central Siberia. *Contributions to Mineralogy and Petrology* **165**, 1225-1242.

Doucet, L. S., Peslier, A. H., Ionov, D. A., Brandon, A. D., Golovin, A. V., Goncharov, A. G. & Ashchepkov, I. V. (2014). High water contents in the Siberian cratonic mantle linked to

metasomatism: An FTIR study of Udachnaya peridotite xenoliths. *Geochimica Et Cosmochimica Acta* **137**, 159-187.

Drury, M. R. & van Roermund, H. L. M. (1989). Fluid assisted recrystallization in upper mantle peridotite xenoliths from kimberlites. *Journal of Petrology* **30**, 133-152.

Dziewonski, A. M. & Anderson, D. L. (1981). Preliminary reference Earth model. *Physics of the Earth and Planetary Interiors* **25**, 297-356.

Eaton, D. W. & Frederiksen, A. (2007). Seismic evidence for convection-driven motion of the North American plate. *Nature* **446**, 428-431.

Eaton, D. W., Darbyshire, F., Evans, R. L., Grütter, H., Jones, A. G. & Yuan, X. H. (2009). The elusive lithosphere-asthenosphere boundary (LAB) beneath cratons. *Lithos* **109**, 1-22.

Elburg, M. A. & Cawthorn, R. G. (2017). Source and evolution of the alkaline Pilanesberg Complex, South Africa. *Chemical Geology* **455**, 148-165.

Ernst, R. E., Davies, D. R., Jowitt, S. M. & Campbell, I. H. (2018). When do mantle plumes destroy diamonds? *Earth and Planetary Science Letters* **502**, 244-252.

Faul, U. H. (1997). Permeability of partially molten upper mantle rocks from experiments and percolation theory. *Journal of Geophysical Research* **102**, 10299-10311.

Field, M., Stiefenhofer, J., Robey, J. & Kurszlaukis, S. (2008). Kimberlite-hosted diamond deposits of southern Africa: A review. *Ore Geology Reviews* **34**, 33-75.

Finnerty, A. A. & Boyd, F. R. (1984). Evaluation of thermobarometers for garnet peridotites. *Geochimica Et Cosmochimica Acta* **48**, 15-27.

Finnerty, A. A. & Boyd, F. R. (1987). Thermobarometry for garnet peridotite xenoliths: A basis for mantle stratigraphy. In: Nixon, P. H. (ed.) *Mantle xenoliths*. New York: Wiley, 381-402.

Fiorentini, M. L., O'Neill, C., Giuliani, A., Choi, E., Maas, R., Pirajno, F. & Foley, S. F. (2020). Bushveld superplume drove Proterozoic magmatism and metallogenesis in Australia. *Scientific Reports* **10**, 1-10.

Foley, S. F., Yaxley, G. M., Rosenthal, A., Buhre, S., Kiseeva, E. S., Rapp, R. P. & Jacob, D. E. (2009). The composition of near-solidus melts of peridotite in the presence of CO_2 and H_2O between 40 and 60 kbar. *Lithos* **112**, 274-283.

Foley, S. F. (2011). A reappraisal of redox melting in the Earth's mantle as a function of tectonic setting and time. *Journal of Petrology* **52**, 1363-1391.

Fossen, H. & Cavalcante, G. C. G. (2017). Shear zones - a review. *Earth-Science Reviews* **171**, 434-455.

Fouch, M. J., James, D. E., VanDecar, J. C. & van der Lee, S. (2004). Mantle seismic structure beneath the Kaapvaal and Zimbabwe Cratons. *South African Journal of Geology* **107**, 33-44.

Frost, D. J. & McCammon, C. A. (2008). The redox state of Earth's mantle. *Annual Review of Earth and Planetary Sciences* **36**, 389-420.

Gaillard, F., Malki, M., Iacono-Marziano, G., Pichavant, M. & Scaillet, B. (2008). Carbonatite melts and electrical conductivity in the asthenosphere. *Science* **322**, 1363-1365.

Ganne, J. & Feng, X. (2017). Primary magmas and mantle temperatures through time. *Geochemistry Geophysics Geosystems* **18**, 872–888.

Gibson, S. A., Malarkey, J. & Day, J. A. (2008). Melt depletion and enrichment beneath the western Kaapvaal craton: Evidence from Finsch peridotite xenoliths. *Journal of Petrology* **49**, 1817-1852.

Gibson, S. A., McMahon, S. C., Day, J. A. & Dawson, J. B. (2013). Highly refractory lithospheric mantle beneath the Tanzanian craton: Evidence from Lashaine pre-metasomatic garnet-bearing peridotites. *Journal of Petrology* **54**, 1503-1546.

Girnis, A. V., Bulatov, V. K., Brey, G. P., Gerdes, A. & Höfer, H. E. (2013). Trace element partitioning between mantle minerals and silico-carbonate melts at 6-12 GPa and applications to mantle metasomatism and kimberlite genesis. *Lithos* **160**, 183-200.

Giuliani, A., Kamenetsky, V. S., Kendrick, M. A., Phillips, D., Wyatt, B. A. & Maas, R. (2013). Oxide, sulphide and carbonate minerals in a mantle polymict breccia: Metasomatism by proto-kimberlite magmas, and relationship to the kimberlite megacrystic suite. *Chemical Geology* **353**, 4-18.

Giuliani, A., Phillips, D., Maas, R., Woodhead, J. D., Kendrick, M. A., Greig, A., Armstrong, R. A., Chew, D., Kamenetsky, V. S. & Fiorentini, M. L. (2014). LIMA U-Pb ages link lithospheric mantle metasomatism to Karoo magmatism beneath the Kimberley region, South Africa. *Earth and Planetary Science Letters* **401**, 132-147.

Goetze, C. (1975). Sheared Iherzolites: From the point of view of rock mechanics. *Geology* **3**, 172-173.

Goncharov, A. G., Ionov, D. A., Doucet, L. S. & Pokhilenko, L. N. (2012). Thermal state, oxygen fugacity and C-O-H fluid speciation in cratonic lithospheric mantle: New data on peridotite xenoliths from the Udachnaya kimberlite, Siberia. *Earth and Planetary Science Letters* **357**, 99-110.

Green, H. W. & Gueguen, Y. (1974). Origin of kimberlite pipes by diapiric upwelling in upper mantle. *Nature* **249**, 617-620.

Green, T. H., Blundy, J. D., Adam, J. & Yaxley, G. M. (2000). SIMS determination of trace element partition coefficients between garnet, clinopyroxene and hydrous basaltic liquids at 2-7.5 GPa and 1080-1200 degrees C. *Lithos* **53**, 165-187.

Gregoire, M., Tinguely, C., Bell, D. R. & le Roex, A. P. (2005). Spinel lherzolite xenoliths from the Premier kimberlite (Kaapvaal craton, South Africa): Nature and evolution of the shallow upper mantle beneath the Bushveld complex. *Lithos* **84**, 185-205.

Gregoire, M., Rabinowicz, M. & Janse, A. J. A. (2006). Mantle mush compaction: A key to understand the mechanisms of concentration of kimberlite melts and initiation of swarms of kimberlite dykes. *Journal of Petrology* **47**, 631-646.

Grégoire, M., Bell, D. R. & le Roex, A. P. (2003). Garnet lherzolites from the Kaapvaal Craton (South Africa): Trace element evidence for a metasomatic history. *Journal of Petrology* **44**, 629-657.

Griffin, W. L. & Ryan, C. G. (1995). Trace elements in indicator minerals: Area selection and target evaluation in diamond exploration. *Journal of Geochemical Exploration* **53**, 311-337.

Griffin, W. L., Doyle, B. J., Ryan, C. G., Pearson, N. J., O'Reilly, S. Y., Davies, R., Kivi, K., van Achterbergh, E. & Natapov, L. M. (1999). Layered mantle lithosphere in the Lac de Gras area, Slave craton: composition, structure and origin. *Journal of Petrology* **40**, 705-728.

Griffin, W. L., Pearson, N. J., Belousova, E. A., Jackson, S. E., van Achterbergh, E., O'Reilly, S. Y. & Shee, S. R. (2000). The Hf isotope composition of cratonic mantle: LAM-MC-ICPMS analysis of zircon megacrysts in kimberlites. *Geochimica Et Cosmochimica Acta* **64**, 133-147.

Griffin, W. L., O'Reilly, S. Y., Natapov, L. M. & Ryan, C. G. (2003). The evolution of lithospheric mantle beneath the Kalahari Craton and its margins. *Lithos* **71**, 215-241.

Griffin, W. L., Begg, G. C. & O'Reilly, S. Y. (2013). Continental-root control on the genesis of magmatic ore deposits. *Nature Geoscience* **6**, 905-910.

Grütter, H. S., Gurney, J. J., Menzies, A. H. & Winter, F. (2004). An updated classification scheme for mantle-derived garnet, for use by diamond explorers. *Lithos* **77**, 841-857.

Grütter, H. S. (2009). Pyroxene xenocryst geotherms: Techniques and application. *Lithos* **112**, 1167-1178.

Gumsley, A., Stamsnijder, J., Larsson, E., Soderlund, U., Naeraa, T., de Kock, M. O., Salacinska, A., Gaweda, A., Humbert, F. & Ernst, R. E. (2020). Neoarchean large igneous provinces on the Kaapvaal craton in southern Africa re-define the formation of the Ventersdorp Supergroup and its temporal equivalents. *Geological Society of America Bulletin* **132**, 1829-1844.

Günther, T., Haase, K. M., Klemd, R. & Teschner, C. (2018). Mantle sources and magma evolution of the Rooiberg lavas, Bushveld Large Igneous Province, South Africa. *Contributions to Mineralogy and Petrology* **173**, 1-51.

Gurney, J. J. & Harte, B. (1980). Chemical variations in upper mantle nodules from southern African kimberlites. *Philosophical Transactions of the Royal Society of London* **297**, 273–293.

Gurney, J. J. & Zweistra, P. (1995). The interpretation of the major element compositions of mantle minerals in diamond exploration. *Journal of Geochemical Exploration* **53**, 293-309.

Gussone, N., Zonneveld, K. & Kuhnert, H. (2010). Minor element and Ca isotope composition of calcareous dinoflagellate cysts of cultured Thoracosphaera heimii. *Earth and Planetary Science Letters* **289**, 180-188.

Gussone, N., Nehrke, G. & Teichert, B. M. A. (2011). Calcium isotope fractionation in ikaite and vaterite. *Chemical Geology* **285**, 194-202.

Haggerty, S. E. (2017). Majorite-indicative ultradeep (>300 km) xenoliths with spinel associations from the Jagersfontein kimberlite, South Africa. *South African Journal of Geology* **120**, 1–20.

Hanger, B. J., Yaxley, G. M., Berry, A. J. & Kamenetsky, V. S. (2015). Relationships between oxygen fugacity and metasomatism in the Kaapvaal subcratonic mantle, represented by garnet peridotite xenoliths in the Wesselton kimberlite, South Africa. *Lithos* **212**, 443-452.

Harmer, R. E. (1999). The petrogenetic association of carbonatite and alkaline magmatism: Constraints from the Spitskop Complex, South Africa. *Journal of Petrology* **40**, 525-548.

Hart, S. R. & Brooks, C. (1977). The geochemistry and evolution of the early Precambrian mantle. *Contributions to Mineralogy and Petrology* **61**, 109-128.

Harte, B. (1977). Rock nomenclature with particular relation to deformation and recrystallisation textures in olivine-bearing xenoliths. *Journal of Geology* **85**, 279-288.

Hasterok, D. & Chapman, D. S. (2011). Heat production and geotherms for the continental lithosphere. *Earth and Planetary Science Letters* **307**, 59-70.

Herzberg, C. & Rudnick, R. (2012). Formation of cratonic lithosphere: An integrated thermal and petrological model. *Lithos* **149**, 4-15.

Heuser, A., Schmitt, A.-D., Gussone, N. & Wombacher, F. (2016). Analytical methods. In: Gussone, N., Schmitt, A.-D., Heuser, A., Wombacher, F., Dietzel, M., Tipper, E. T. & Schiller, M. (eds.) *Calcium stable isotope geochemistry*. Heidelberg: Springer, 23-73.

Hoal, K. O. (2003). Samples of Proterozoic iron-enriched mantle from the Premier kimberlite. *Lithos* **71**, 259-272.

Hofmann, A., Anhaeusser, C. R., Dixon, J., Kröner, A., Saha, L., Wilson, A. & Xie, H. (2019). Archaean granitoid–greenstone geology of the southeastern part of the Kaapvaal craton. In: Kröner, A. & Hofmann, A. (eds.) *The Archaean geology of the Kaapvaal craton, southern Africa*. Heidelberg: Springer, 33-54.

Holtzman, B. K. & Kohlstedt, D. L. (2007). Stress-driven melt segregation and strain partitioning in partially molten rocks: Effects of stress and strain. *Journal of Petrology* **48**, 2379-2406.

Holtzman, B. K., King, D. S. H. & Kohlstedt, D. L. (2012). Effects of stress-driven melt segregation on the viscosity of rocks. *Earth and Planetary Science Letters* **359**, 184-193.

Hops, J. J., Gurney, J. J. & Harte, B. (1992). The Jagersfontein Cr-poor megacryst suite: Towards a model for megacryst petrogenesis. *Journal of Volcanology and Geothermal Research* **50**, 143-160.

Howarth, G. H. & Büttner, S. H. (2019). New constraints on archetypal South African kimberlite petrogenesis from quenched glass-rich melt inclusions in olivine megacrysts. *Gondwana Research* **68**, 116-126.

Huang, F., Zhou, C., Wang, W. Z., Kang, J. T. & Wu, Z. Q. (2019). First-principles calculations of equilibrium Ca isotope fractionation: Implications for oldhamite formation and evolution of lunar magma ocean. *Earth and Planetary Science Letters* **510**, 153-160.

Hunt, L., Stachel, T., Grütter, H. S., Armstrong, J., McCandless, T. E., Simonetti, A. & Tappe, S. (2012). Small mantle fragments from the Renard kimberlites, Quebec: Powerful recorders of mantle lithosphere formation and modification beneath the eastern Superior craton. *Journal of Petrology* **53**, 1597-1635.

Jablon, B. M. & Navon, O. (2016). Most diamonds were created equal. *Earth and Planetary Science Letters* **443**, 41-47.

Jacob, D. E., Bizimis, M. & Salters, V. J. M. (2005). Lu-Hf and geochemical systematics of recycled ancient oceanic crust: Evidence from Roberts Victor eclogites. *Contributions to Mineralogy and Petrology* **148**, 707-720.

Jacobs, J., Pisarevsky, S., Thomas, R. J. & Becker, T. (2008). The Kalahari Craton during the assembly and dispersal of Rodinia. *Precambrian Research* **160**, 142-158.

James, D. E., Fouch, M. J., VanDecar, J. C. & van der Lee, S. (2001). Tectospheric structure beneath southern Africa. *Geophysical Research Letters* **28**, 2485-2488.

Jollands, M. C., Hanger, B. J., Yaxley, G. M., Hermann, J. & Kilburn, M. R. (2018). Timescales between mantle metasomatism and kimberlite ascent indicated by diffusion profiles in garnet crystals from peridotite xenoliths. *Earth and Planetary Science Letters* **481**, 143-153.

Jones, A. G., Plomerova, J., Korja, T., Sodoudi, F. & Spakman, W. (2010). Europe from the bottom up: A statistical examination of the central and northern European lithosphere-asthenosphere boundary from comparing seismological and electromagnetic observations. *Lithos* **120**, 14-29.

Jordan, T. H. (1978). Composition and development of the continental tectosphere. *Nature* **274**, 544-548.

Jordan, T. H. (1988). Structure and formation of the continental tectosphere. *Journal of Petrology* **1988**, 11-37.

Kaban, M. K., Mooney, W. D. & Petrunin, A. G. (2015). Cratonic root beneath North America shifted by basal drag from the convecting mantle. *Nature Geoscience* **8**, 797-800.

Kamber, B. S. & Tomlinson, E. L. (2019). Petrological, mineralogical and geochemical peculiarities of Archaean cratons. *Chemical Geology* **511**, 123-151.

Kang, J. T., Ionov, D. A., Liu, F., Zhang, C. L., Golovin, A. V., Qin, L. P., Zhang, Z. F. & Huang, F. (2017). Calcium isotopic fractionation in mantle peridotites by melting and metasomatism and Ca isotope composition of the Bulk Silicate Earth. *Earth and Planetary Science Letters* **474**, 128-137.

Kargin, A. V., Sazonovaa, L. V., Andreevn, A., Pervov, V., Minevrina, E. V., Khvostikov, V. A. & Burmii, Z. P. (2017). Sheared peridotite xenolith from the V. Grib kimberlite pipe, Arkhangelsk Diamond Province, Russia: Texture, composition, and origin. *Geoscience Frontiers* **8**, 653-669.

Katayama, I., Suyama, Y., Ando, J. I. & Komiya, T. (2009). Mineral chemistry and P-T condition of granular and sheared peridotite xenoliths from Kimberley, South Africa: Origin of the textural variation in the cratonic mantle. *Lithos* **109**, 333-340.

Katz, R. F., Spiegelman, M. & Holtzman, B. K. (2006). The dynamics of melt and shear localization in partially molten aggregates. *Nature* **442**, 676-679.

Kennedy, L. A., Russell, J. K. & Kopylova, M. G. (2002). Mantle shear zones revisited: The connection between the cratons and mantle dynamics. *Geology* **30**, 419-422.

Keshav, S., Corgne, A., Gudfinnsson, G. H., Bizimis, M., McDonough, W. F. & Fei, Y. W. (2005). Kimberlite petrogenesis: Insights from clinopyroxene-melt partitioning experiments at 6 GPa in the CaO-MgO-Al2O3-SiO2-CO2 system. *Geochimica Et Cosmochimica Acta* **69**, 2829-2845.

Kilgore, M. L., Peslier, A. H., Brandon, A. D., Schaffer, L. A., Morris, R. V., Graff, T. G., Agresti, D. G., O'Reilly, S. Y., Griffin, W. L., Pearson, D. G., Gangi, K. & Shaulis, B. J. (2020). Metasomatic control of hydrogen contents in the layered cratonic mantle lithosphere sampled by Lac de Gras xenoliths in the central Slave craton, Canada. *Geochimica Et Cosmochimica Acta* **286**, 29-53.

Klein-BenDavid, O. & Pearson, D. G. (2009). Origins of subcalcic garnets and their relation to diamond forming fluids: Case studies from Ekati (NWT-Canada) and Murowa (Zimbabwe). *Geochimica Et Cosmochimica Acta* **73**, 837-855.

Kobussen, A. F., Griffin, W. L. & O'Reilly, S. Y. (2009). Cretaceous thermo-chemical modification of the Kaapvaal cratonic lithosphere, South Africa. *Lithos* **112**, 886-895.

Kopylova, M. G., Russell, J. K. & Cookenboo, H. O. (1999). Petrology of peridotite and pyroxenite xenoliths from Jericho kimberlite: Implications for the thermal state of the mantle beneath the Slave Craton, northern Canada. *Journal of Petrology* **40**, 79-104.

Kopylova, M. G., Nowell, G. M., Pearson, D. G. & Markovic, G. (2009). Crystallization of megacrysts from protokimberlitic fluids: Geochemical evidence from high-Cr megacrysts in the Jericho kimberlite. *Lithos* **112**, 284-295.

Kopylova, M. G., Tso, E., Ma, F., Liu, J. G. & Pearson, D. G. (2019). The metasomatized mantle beneath the North Atlantic Craton: Insights from peridotite xenoliths of the Chidliak kimberlite province (NE Canada). *Journal of Petrology* **60**, 1991-2024.

Kopylova, M. G., Ma, F. & Tso, E. (2021). Constraining carbonation freezing and petrography of the carbonated cratonic mantle with natural samples. *Lithos* **388**, 1-15.

Korolev, N., Kopylova, M. G., Gurney, J. J., Moore, A. E. & Davidson, J. (2018a). The origin of Type II diamonds as inferred from Cullinan mineral inclusions. *Mineralogy and Petrology* **112**, 275-289.

Korolev, N. M., Kopylova, M. G., Bussweiler, Y., Pearson, D. G., Gurney, J. J. & Davidson, J. (2018b). The uniquely high-temperature character of Cullinan diamonds: A signature of the Bushveld mantle plume? *Lithos* **304**, 362-373.

Kramers, J. D. & Smith, C. B. (1983). A feasibility study of U-Pb and Pb-Pb dating of kimberlites using groundmass mineral fractions and whole-rock samples. *Chemical Geology* **41**, 23-38.

Lazarov, M., Woodland, A. B. & Brey, G. P. (2009). Thermal state and redox conditions of the Kaapvaal mantle: A study of xenoliths from the Finsch mine, South Africa. *Lithos* **112**, 913-923.

Le Roux, V., Tommasi, A. & Vauchez, A. (2008). Feedback between melt percolation and deformation in an exhumed lithosphere-asthenosphere boundary. *Earth and Planetary Science Letters* **274**, 401-413.

Lee, A. L., Torvela, T., Lloyd, G. E. & Walker, A. M. (2018). Melt organisation and strain partitioning in the lower crust. *Journal of Structural Geology* **113**, 188-199.

Lugmair, G. W. & Marti, K. (1978). Lunar initial $^{143}Nd/^{144}Nd$: Differential evolution of the lunar crust and mantle. *Earth and Planetary Science Letters* **39**, 349-357.

Maier, W. D., Barnes, S.-J. & Karykowski, B. T. (2016). A chilled margin of komatiite and Mg-rich basaltic andesite in the western Bushveld Complex, South Africa. *Contributions to Mineralogy and Petrology* **171**, 1-22.

Malkovets, V. G., Griffin, W. L., O'Reilly, S. Y. & Wood, B. J. (2007). Diamond, subcalcic garnet, and mantle metasomatism: Kimberlite sampling patterns define the link. *Geology* **35**, 339-342.

Mancinelli, N. J., Fischer, K. M. & Dalton, C. A. (2017). How sharp is the cratonic lithosphere-asthenosphere transition? *Geophysical Research Letters* **44**, 10189-10197.

Massuyeau, M., Gardes, E., Rogerie, G., Aulbach, S., Tappe, S., Le Trong, E., Sifre, D. & Gaillard, F. (2021). MAGLAB: A computing platform connecting geophysical signatures to melting processes in Earth's mantle. *Physics of the Earth and Planetary Interiors* **106638**.

Masters, G., Johnson, S., Laske, G. & Bolton, H. (1996). A shear-velocity model of the mantle. *Philosophical Transactions of the Royal Society of London* **354**, 1385-1410.

Mather, K. A., Pearson, D. G., McKenzie, D., Kjarsgaard, B. A. & Priestley, K. (2011). Constraints on the depth and thermal history of cratonic lithosphere from peridotite xenoliths, xenocrysts and seismology. *Lithos* **125**, 729-742.

McCoy-West, A. J., Baker, J. A., Faure, K. & Wysoczanski, R. (2010). Petrogenesis and origins of mid-Cretaceous continental intraplate volcanism in Marlborough, New Zealand: Implications for the long-lived HIMU magmatic mega-province of the SW Pacific. *Journal of Petrology* **51**, 2003-2045.

McCoy-West, A. J., Bennett, V. C., O'Neill, H. S. C., Hermann, J. & Puchtel, I. S. (2015). The interplay between melting, refertilization and carbonatite metasomatism in off-cratonic lithospheric mantle under Zealandia: An integrated major, trace and platinum group element study. *Journal of Petrology* **56**, 563-604.

McKenzie, D. & Bickle, M. J. (1988). The volume and composition of melt generated by extension of the lithosphere. *Journal of Petrology* **29**, 625-679.

McKenzie, D. (1989). Some remarks on the movement of small melt fractions in the mantle. *Earth and Planetary Science Letters* **95**, 53-72.

Mercier, J.-C. C. (1979). Peridotite xenoliths and the dynamics of kimberlite intrusion. In: Boyd, F. R. & Meyer, H. O. A. (eds.) *Proceedings of the Second International Kimberlite Conference*. Washington D.C.: American Geophysical Union, 197–211.

Michaut, C., Jaupart, C. & Bell, D. R. (2007). Transient geotherms in Archean continental lithosphere: New constraints on thickness and heat production of the subcontinental lithospheric mantle. *Journal of Geophysical Research* **112**, 1-17.

Moore, A. E. & Lock, N. P. (2001). The origin of mantle-derived megacrysts and sheared peridotites: Evidence from kimberlites in the northern Lesotho, Orange Free State (South Africa), and Botswana pipe clusters. *South African Journal of Geology* **104**, 23-38.

Moore, A. E. & Belousova, E. A. (2005). Crystallization of Cr-poor and Cr-rich megacryst suites from the host kimberlite magma: Implications for mantle structure and the generation of kimberlite magmas. *Contributions to Mineralogy and Petrology* **149**, 462-481.

Moore, A. E. (2009). Type II diamonds: flamboyant megacrysts? *South African Journal of Geology* **112**, 23-38.

Moore, A. E. & Helmstaedt, H. (2019). Evidence for two blue (type IIb) diamond populations. *Nature* **570**, E26–E27.

Morel, M. L. A., Davies, G. R., Pearson, D. G., Viljoen, K. S. & Wittig, N. (2008). Os isotope and PGE evidence for modification of cratonic lithosphere: A study of peridotites from the Premier Mine, Kaapvaal craton, SA. *International Kimberlite Conference: Extended Abstracts 9*, doi.org/10.29173/ikc23294.

Moussallam, Y., Longpre, M. A., McCammon, C., Gomez-Ulla, A., Rose-Koga, E. F., Scaillet, B., Peters, N., Gennaro, E., Paris, R. & Oppenheimer, C. (2019). Mantle plumes are oxidised. *Earth and Planetary Science Letters* **527**, 1-10.

Münker, C., Weyer, S., Scherer, E. & Mezger, K. (2001). Separation of high field strength elements (Nb, Ta, Zr, Hf) and Lu from rock samples for MC-ICPMS measurements. *Geochemistry Geophysics Geosystems* **2**, 2001GC000183.

Nestola, F., Korolev, N., Kopylova, M. G., Rotiroti, N., Pearson, D. G., Pamato, M. G., Alvaro, M., Peruzzo, L., Gurney, J. J., Moore, A. E. & Davidson, J. (2018). $CaSiO_3$ perovskite in diamond indicates the recycling of oceanic crust into the lower mantle. *Nature* **555**, 237-241.

Ngwenya, N. S. & Tappe, S. (2021). Diamondiferous lamproites of the Luangwa Rift in central Africa and links to remobilized cratonic lithosphere. *Chemical Geology*, 120019.

Nickel, K. G. & Green, D. H. (1985). Empirical geothermobarometry for garnet peridotites and implications for the nature of the lithosphere, kimberlites and diamonds. *Earth and Planetary Science Letters* **73**, 158-170.

Nicklas, R. W., Puchtel, I. S., Ash, R. D., Piccoli, H. M., Hanski, E., Nisbet, E. G., Waterton, P., Pearson, D. G. & Anbar, A. D. (2019). Secular mantle oxidation across the Archean-Proterozoic boundary: Evidence from V partitioning in komatiites and picrites. *Geochimica Et Cosmochimica Acta* **250**, 49-75.

Nimis, P. & Taylor, W. R. (2000). Single clinopyroxene thermobarometry for garnet peridotites: Part I. Calibration and testing of a Cr-in-Cpx barometer and an enstatite-in-Cpx thermometer. *Contributions to Mineralogy and Petrology* **139**, 541-554.

Nimis, P. (2002). The pressures and temperatures of formation of diamond based on thermobarometry of chromian diopside inclusions. *The Canadian Mineralogist* **40**, 871-884.

Nimis, P. & Grütter, H. S. (2010). Internally consistent geothermometers for garnet peridotites and pyroxenites. *Contributions to Mineralogy and Petrology* **159**, 411-427.

Nimis, P., Preston, R., Perritt, S. H. & Chinn, I. L. (2020). Diamond's depth distribution systematics. *Lithos* **376**, 1-15.

Nixon, P. H. & Boyd, F. R. (1973a). The discrete nodule association in kimberlites from northern Lesotho. In: Nixon, P. H. (ed.) *Lesotho kimberlites*. Maseru: Lesotho National Development Corporation Maseru, 67-75.

Nixon, P. H. & Boyd, F. R. (1973b). Petrogenesis of the granular and sheared ultrabasic nodule suite in kimberlites. In: Nixon, P. H. (ed.) *Lesotho kimberlites*. Maseru: Lesotho National Development Corporation Maseru, 48-56.

Nowell, G. M., Pearson, D. G., Bell, D. R., Carlson, R. W., Smith, C. B., Kempton, P. D. & Noble, S. R. (2004). Hf isotope systematics of kimberlites and their megacrysts: New constraints on their source regions. *Journal of Petrology* **45**, 1583-1612.

O'Reilly, S. Y., Griffin, W. L., Djomani, Y. H. & Morgan, P. (2001). Are lithospheres forever? Tracking changes in subcontinental lithospheric mantle through time. *GSA Today* **11**, 4-10.

O'Reilly, S. Y. & Griffin, W. L. (2010). The continental lithosphere-asthenoshpere boundary: Can we sample it? *Lithos* **120**, 1-13.

Palme, H. & Jones, A. (2003). Solar system abundances of the elements. In: Carlson, R. W. (ed.) *Treatise on Geochemistry*. Amsterdam: Elsevier, 41-61.

Palme, H. & O'Neill, H. S. C. (2003). Cosmochemical estimates of mantle composition. In: Carlson, R. W. (ed.) *Treatise on Geochemistry*. Amsterdam: Elsevier, 1-38.

Pearson, D. G., Carlson, R. W., Shirey, S. B., Boyd, F. R. & Nixon, P. H. (1995). Stabilisation of Archaean lithospheric mantle: a Re-Os isotope study of peridotite xenoliths from the Kaapvaal Craton. *Earth and Planetary Science Letters* **134**, 341-357.

Pearson, D. G. (1999). The age of continental roots. *Lithos* **48**, 71-194.

Pearson, D. G. & Wittig, N. (2014). The formation and evolution of cratonic mantle lithosphere: Evidence from mantle xenoliths. In: Carlson, R. W. (ed.) *Treatise on Geochemistry*. Amsterdam: Elsevier, 255-292.

Peslier, A. H., Woodland, A. B., Bell, D. R. & Lazarov, M. (2010). Olivine water contents in the continental lithosphere and the longevity of cratons. *Nature* **467**, 78-81.

Pin, C. & Zalduegui, J. F. S. (1997). Sequential separation of light rare-earth elements, thorium and uranium by miniaturized extraction chromatography: Application to isotopic analyses of silicate rocks. *Analytica Chimica Acta* **339**, 79-89.

Pollack, H. N. & Chapman, D. S. (1977). On the regional variation of heat flow, geotherms, and lithospheric thickness. *Tectonophysics* **38**, 279-296.

Poujol, M., Robb, L. J., Anhaeusser, C. R. & Gericke, B. (2003). A review of the geochronological constraints on the evolution of the Kaapvaal Craton, South Africa. *Precambrian Research* **127**, 181-213.

Priestley, K., McKenzie, D. & Ho, T. (2019). A lithosphere–asthenosphere boundary: A global model derived from multimode surface-wave tomography and petrology. In: Yuan, H. L. & Romanowicz, B. (eds.) *Lithospheric discontinuities (Geophysical Monograph 239)*: Wiley, 111-123.

Rabinowicz, M., Ricard, Y. & Gregoire, M. (2002). Compaction in a mantle with a very small melt concentration: Implications for the generation of carbonatitic and carbonate-bearing high alkaline mafic melt impregnations. *Earth and Planetary Science Letters* **203**, 205-220.

Rehfeldt, T., Jacob, D. E., Carlson, R. W. & Foley, S. F. (2007). Fe-rich dunite xenoliths from South African kimberlites: Cumulates from Karoo flood basalts. *Journal of Petrology* **48**, 1387-1409.

Rehfeldt, T., Foley, S. F., Jacob, D. E., Carlson, R. W. & Lowry, D. (2008). Contrasting types of metasomatism in dunite, wehrlite and websterite xenoliths from Kimberley, South Africa. *Geochimica Et Cosmochimica Acta* **72**, 5722-5756.

Richardson, S. H., Harris, J. W. & Gurney, J. J. (1993). Three generations of diamonds from old continental mantle. *Nature* **366**, 256-258.

Richardson, S. H. & Shirey, S. B. (2008). Continental mantle signature of Bushveld magmas and coeval diamonds. *Nature* **453**, 910-913.

Rudnick, R. L., McDonough, W. F. & Chappell, B. W. (1993). Carbonatite metasomatism in the northern Tanzania mantle: Petrographic and geochemical characteristics. *Earth and Planetary Science Letters* **114**, 463-475.

Rudnick, R. L. & Nyblade, A. A. (1999). The thickness and heat production of Archean lithosphere, constraints from xenolith thermobarometry and surface heat flow. In: Fei, Y., Bertka, C. M. & Mysen, B. O. (eds.) *Mantle petrology: Field observations and high pressure experimentation: A tribute to Francis R. Boyd*: The Geochemical Society, 3-12.

Rychert, C. A., Harmon, N., Constable, S. & Wang, S. (2020). The nature of the lithosphere-asthenosphere boundary. *Journal of Geophysical Research* **125**, 1-39.

Sand, K. K., Waight, T. E., Pearson, D. G., Nielsen, T. F. D., Makovicky, E. & Hutchison, M. T. (2009). The lithospheric mantle below southern West Greenland: A geothermobarometric approach to diamond potential and mantle stratigraphy. *Lithos* **112**, 1155-1166.

Scherer, E. E., Münker, C. & Mezger, K. (2001). Calibration of the lutetium-hafnium clock. *Science* **293**, 683-687.

Schiller, M., Gussone, N. & Wombacher, F. (2016). High temperature geochemistry and cosmochemistry. In: Gussone, N., Schmitt, A.-D., Heuser, A., Wombacher, F., Dietzel, M., Tipper, E. T. & Schiller, M. (eds.) *Calcium stable isotope geochemistry*. Heidelberg: Springer, 223-245.

Schmidberger, S. S., Simonetti, A., Heaman, L. M., Creaser, R. A. & Whiteford, S. (2007). Lu-Hf, in-situ Sr and Pb isotope and trace element systematics for mantle eclogites from the Diavik diamond mine: Evidence for Paleoproterozoic subduction beneath the Slave craton, Canada. *Earth and Planetary Science Letters* **254**, 55-68.

Schmitz, M. D., Bowring, S. A., de Wit, M. J. & Gartz, V. (2004). Subduction and terrane collision stabilize the western Kaapvaal craton tectosphere 2.9 billion years ago. *Earth and Planetary Science Letters* **222**, 363-376.

Shaikh, A. M., Tappe, S., Bussweiler, Y., Patel, S. C., Ravi, S., Bolhar, R. & Viljoen, K. S. (2020). Clinopyroxene and garnet mantle cargo in kimberlites as probes of Dharwar craton architecture and geotherms, with implications for post-1.1 Ga lithosphere thinning events beneath southern India. *Journal of Petrology* **61**, egaa087.

Shirey, S. B., Harris, J. W., Richardson, S. H., Fouch, M. J., James, D. E., Cartigny, P., Deines, P. & Viljoen, K. S. (2002). Diamond genesis, seismic structure, and evolution of the Kaapvaal-Zimbabwe craton. *Science* **297**, 1683-1686.

Shirey, S. B., Richardson, S. H. & Harris, J. W. (2004). Integrated models of diamond formation and craton evolution. *Lithos* **77**, 923-944.

Shu, Q. & Brey, G. P. (2015). Ancient mantle metasomatism recorded in subcalcic garnet xenocrysts: Temporal links between mantle metasomatism, diamond growth and crustal tectonomagmatism. *Earth and Planetary Science Letters* **418**, 27-39.

Shu, Q., Brey, G. P., Pearson, D. G., Liu, J. G., Gibson, S. A. & Becker, H. (2019). The evolution of the Kaapvaal craton: A multi-isotopic perspective from lithospheric peridotites from Finsch diamond mine. *Precambrian Research* **331**, 1-21.

Simon, N. S. C., Irvine, G. J., Davies, G. R., Pearson, D. G. & Carlson, R. W. (2003). The origin of garnet and clinopyroxene in "depleted" Kaapvaal peridotites. *Lithos* **71**, 289-322.

Simon, N. S. C., Carlson, R. W., Pearson, D. G. & Davies, G. R. (2007). The origin and evolution of the Kaapvaal cratonic lithospheric mantle. *Journal of Petrology* **48**, 589-625.

Skemer, P. & Karato, S. I. (2008). Sheared lherzolite xenoliths revisited. *Journal of Geophysical Research* **113**, 1-14.

Sleep, N. H. (2003). Geodynamic implications of xenolith geotherms. *Geochemistry Geophysics Geosystems* **4, 1079**.

Smart, K. A., Tappe, S., Stern, R. A., Webb, S. J. & Ashwal, L. D. (2016). Early Archaean tectonics and mantle redox recorded in Witwatersrand diamonds. *Nature Geoscience* **9**, 255-259.

Smart, K. A., Tappe, S., Simonetti, A., Simonetti, S. S., Woodland, A. B. & Harris, C. (2017). Tectonic significance and redox state of Paleoproterozoic eclogite and pyroxenite components in the Slave cratonic mantle lithosphere, Voyageur kimberlite, Arctic Canada. *Chemical Geology* **455**, 98-119.

Smart, K. A., Tappe, S., Woodland, A. B., Greyling, D. R., Harris, C. & Gussone, N. (2021a). Constraints on Archean crust recycling and the origin of mantle redox variability from the δ44/40Ca – δ18O – *f*O2 signatures of cratonic eclogites. *Earth and Planetary Science Letters* **556**, 116720.

Smart, K. A., Tappe, S., Woodland, A. B., Harris, C., Corcoran, L. & Simonetti, A. (2021b). Metasomatized eclogite xenoliths from the central Kaapvaal craton as probes of a seismic mid-lithospheric discontinuity. *Chemical Geology* **578**, 120286.

Smith, E. M., Kopylova, M. G., Nowell, G. M., Pearson, D. G. & Ryder, J. (2012). Archean mantle fluids preserved in fibrous diamonds from Wawa, Superior craton. *Geology* **40**, 1071-1074.

Smith, E. M., Shirey, S. B., Nestola, F., Bullock, E. S., Wang, J. H., Richardson, S. H. & Wang, W. Y. (2016). Large gem diamonds from metallic liquid in Earth's deep mantle. *Science* **354**, 1403-1405.

Smith, E. M., Shirey, S. B., Richardson, S. H., Nestola, F., Bullocks, E. S., Wang, J. H. & Wang, W. Y. (2018). Blue boron-bearing diamonds from Earth's lower mantle. *Nature* **560**, 84-87.

Sobolev, N. V., Lavrent'ev, Y. G., Pokhilenko, N. P. & Usova, L. V. (1973). Chrome-rich garnets from the kimberlites of Yakutia and their parageneses. *Contributions to Mineralogy and Petrology* **40**, 39–52.

Solovova, I. P., Yudovskaya, M. A., Kinnaird, J. A., Wilson, A. H. & Zinovieva, N. G. (2021). A siliceous komatiitic source of Bushveld magmas revealed by primary melt inclusions in olivine. *Lithos* **388**, 106094.

Spencer, C. J., Thomas, R. J., Roberts, N. M. W., Cawood, P. A., Millar, I. & Tapster, S. (2015). Crustal growth during island arc accretion and transcurrent deformation, Natal Metamorphic Province, South Africa: New isotopic constraints. *Precambrian Research* **265**, 203-217.

Stagno, V. & Frost, D. J. (2010). Carbon speciation in the asthenosphere: Experimental measurements of the redox conditions at which carbonate-bearing melts coexist with graphite or diamond in peridotite assemblages. *Earth and Planetary Science Letters* **300**, 72-84.

Stagno, V., Ojwang, D. O., McCammon, C. A. & Frost, D. J. (2013). The oxidation state of the mantle and the extraction of carbon from Earth's interior. *Nature* **493**, 84-88.

Stankiewicz, J. & de Wit, M. J. (2013). 3.5 billion years of reshaped Moho, southern Africa. *Tectonophysics* **609**, 675-689.

Stoddard, P. R. & Abbott, D. (1996). Influence of the tectosphere upon plate motion. *Journal of Geophysical Research* **101**, 5425-5433.

Sun, J., Zhu, X. K., Belshaw, N. S., Chen, W., Doroshkevich, A. G., Luo, W. J., Song, W. L., Chen, B. B., Cheng, Z. G., Li, Z. H., Wang, Y., Kynicky, J. & Henderson, G. M. (2021). Ca isotope systematics of carbonatites: Insights into carbonatite source and evolution. *Geochemical Perspectives Letters* **17**, 11-15.

Tanaka, T., Togashi, S., Kamioka, H., Amakawa, H., Kagami, H., Hamamoto, T., Yuhara, M., Orihashi, Y., Yoneda, S., Shimizu, H., Kunimaru, T., Takahashi, K., Yanagi, T., Nakano, T., Fujimaki, H., Shinjo, R., Asahara, Y., Tanimizu, M. & Dragusanu, C. (2000). JNdi-1: A neodymium isotopic reference in consistency with La Jolla neodymium. *Chemical Geology* **168**, 279-281.

Tappe, S., Foley, S. F., Stracke, A., Romer, R. L., Kjarsgaard, B. A., Heaman, L. M. & Joyce, N. (2007). Craton reactivation on the Labrador Sea margins: $^{40}Ar/^{39}Ar$ age and Sr–Nd–Hf–Pb isotope constraints from alkaline and carbonatite intrusives. *Earth and Planetary Science Letters* **256**, 433-454.

Tappe, S., Pearson, D. G., Nowell, G. M., Nielsen, T. F. D., Milstead, P. & Muehlenbachs, K. (2011). A fresh isotopic look at Greenland kimberlites: Cratonic mantle lithosphere imprint on deep source signal. *Earth and Planetary Science Letters* **305**, 235-248.

Tappe, S., Romer, R. L., Stracke, A., Steenfelt, A., Smart, K. A., Muehlenbachs, K. & Torsvik, T. H. (2017). Sources and mobility of carbonate melts beneath cratons, with implications for deep carbon cycling, metasomatism and rift initiation. *Earth and Planetary Science Letters* **466**, 152-167.

Tappe, S., Dongre, A., Liu, C.-Z. & Wu, F.-Y. (2018a). 'Premier' evidence for prolonged kimberlite pipe formation and its influence on diamond transport from deep Earth. *Geology* **46**, 843–846.

Tappe, S., Smart, K. A., Torsvik, T. H., Massuyeau, M. & de Wit, M. C. J. (2018b). Geodynamics of kimberlites on a cooling Earth: Clues to plate tectonic evolution and deep volatile cycles. *Earth and Planetary Science Letters* **484**, 1-14.

Tappe, S., Budde, G., Stracke, A., Wilson, A. & Kleine, T. (2020a). The tungsten-182 record of kimberlites above the African superplume: Exploring links to the core-mantle boundary. *Earth and Planetary Science Letters* **547**, 116473.

Tappe, S., Stracke, A., van Acken, D., Strauss, H. & Luguet, A. (2020b). Origins of kimberlites and carbonatites during continental collision – Insights beyond decoupled Nd-Hf isotopes. *Earth-Science Reviews* **208**, 103287.

Taylor, W. R. (1998). An experimental test of some geothermometer and geobarometer formulations for upper mantle peridotites with application to the thermobarometry of fertile lherzolite and garnet websterite. *Neues Jahrbuch für Mineralogie Abhandlungen* **172**, 381-408.

Tharimena, S., Rychert, C. & Harmon, N. (2017). A unified continental thickness from seismology and diamonds suggests a melt-defined plate. *Science* **357**, 580-583.

Thirlwall, M. F. (1991). Long-term reproducibility of multicollector Sr and Nd isotope ratio analysis. *Chemical Geology* **94**, 85-104.

Tomlinson, E. L., Kamber, B. S., Hoare, B. C., Stead, C. V. & Ildefonse, B. (2018). An exsolution origin for Archean mantle garnet. *Geology* **46**, 123-126.

van Achterbergh, E., Griffin, W. L., Ryan, C. G., O'Reilly, S. Y., Pearson, N. J., Kivi, K. & Doyle, B. J. (2002). Subduction signature for quenched carbonatites from the deep lithosphere. *Geology* **30**, 743-746.

van Achterbergh, E., Griffin, W. L., Ryan, C. G., O'Reilly, S. Y., Pearson, N. J., Kivi, K. & Doyle, B. J. (2004). Melt inclusions from the deep Slave lithosphere: Implications for the origin and evolution of mantle-derived carbonatite and kimberlite. *Lithos* **76**, 461-474.

van der Meer, Q. H. A., Klaver, M., Waight, T. E. & Davies, G. R. (2013). The provenance of sub-cratonic mantle beneath the Limpopo Mobile Belt (South Africa). *Lithos* **170**, 90-104.

Van Schijndel, V., Cornell, D. H., Anczkiewicz, R. & Schersten, A. (2020). Evidence for Mesoproterozoic collision, deep burial and rapid exhumation of garbenschiefer in the Namaqua Front, South Africa. *Geoscience Frontiers* **11**, 511-531.

Verwoerd, W. J. (2006). The Pilanesberg Alkaline Province. In: Johnson, M. R., Anhaeusser, C. R. & Thomas, R. J. (eds.) *The Geology of South Africa*. Johannesburg: Geological Society of South Africa and Council for Geoscience, 381-393.

Viljoen, K. S., Dobbe, R. & Smit, B. (2009). Geochemical processes in peridotite xenoliths from the Premier diamond mine, South Africa: Evidence for the depletion and refertilisation of subcratonic lithosphere. *Lithos* **112**, 1133-1142.

Viljoen, K. S., Harris, J. W., Ivanic, T., Richardson, S. H. & Gray, K. (2014). Trace element chemistry of peridotitic garnets in diamonds from the Premier (Cullinan) and Finsch kimberlites, South Africa: Contrasting styles of mantle metasomatism. *Lithos* **208**, 1-15.

Walker, R. J., Carlson, R. W., Shirey, S. B. & Boyd, F. R. (1989). Os, Sr, Nd, and Pb isotope systematics of southern African peridotite xenoliths: Implications for the chemical evolution of subcontinental mantle. *Geochimica Et Cosmochimica Acta* **53**, 1583-1595.

Wang, Y., He, Y. S., Wu, H. J., Zhu, C. W., Huang, S. C. & Huang, J. (2019). Calcium isotope fractionation during crustal melting and magma differentiation: Granitoid and mineral-pair perspectives. *Geochimica Et Cosmochimica Acta* **259**, 37-52.

Weis, D., Kieffer, B., Maerschalk, C., Barling, J., de Jong, J., Williams, G. A., Hanano, D., Pretorius, W., Mattielli, N., Scoates, J. S., Goolaerts, A., Friedman, R. M. & Mahoney, J. B. (2006). High-precision isotopic characterization of USGS reference materials by TIMS and MC-ICP-MS. *Geochemistry Geophysics Geosystems* **7**, Q08006.

Weiss, Y., Griffin, W. L., Bell, D. R. & Navon, O. (2011). High-Mg carbonatitic melts in diamonds, kimberlites and the subcontinental lithosphere. *Earth and Planetary Science Letters* **309**, 337-347.

Weiss, Y., Navon, O., Goldstein, S. L. & Harris, J. W. (2018). Inclusions in diamonds constrain thermo-chemical conditions during Mesozoic metasomatism of the Kaapvaal cratonic mantle. *Earth and Planetary Science Letters* **491**, 134-147.

Wilson, A. H. (2012). A chill sequence to the Bushveld Complex: Insight into the first stage of emplacement and implications for the parental magmas. *Journal of Petrology* **53**, 1123-1168.

Woodland, A. B. & Koch, M. (2003). Variation in oxygen fugacity with depth in the upper mantle beneath the Kaapvaal craton, Southern Africa. *Earth and Planetary Science Letters* **214**, 295-310.

Wright, C., Kgaswane, E. M., Kwadiba, M. T. O., Simon, R. E., Nguuri, T. K. & McRae-Samuel, R. (2003). South African seismicity, April 1997 to April 1999, and regional variations in the crust and uppermost mantle of the Kaapvaal craton. *Lithos* **71**, 369-392.

Xiong, X. L. (2006). Trace element evidence for growth of early continental crust by melting of rutile-bearing hydrous eclogite. *Geology* **34**, 945-948.

Yaxley, G. M., Berry, A. J., Kamenetsky, V. S., Woodland, A. B. & Golovin, A. V. (2012). An oxygen fugacity profile through the Siberian Craton: Fe K-edge XANES determinations of Fe3+/Sigma-Fe in garnets in peridotite xenoliths from the Udachnaya East kimberlite. *Lithos* **140**, 142-151.

Yaxley, G. M., Berry, A. J., Rosenthal, A., Woodland, A. B. & Paterson, D. (2017). Redox preconditioning deep cratonic lithosphere for kimberlite genesis: Evidence from the central Slave craton. *Scientific Reports* **7**, 1-10.

Youssof, M., Thybo, H., Artemieva, I. M. & Levander, A. (2013). Moho depth and crustal composition in southern Africa. *Tectonophysics* **609**, 267-287.

Zack, T., Foley, S. F. & Jenner, G. A. (1997). A consistent partition coefficient set for clinopyroxene, amphibole and garnet from laser ablation microprobe analysis of garnet pyroxenites from Kakanui, New Zealand. *Neues Jahrbuch für Mineralogie Abhandlungen* **172**, 23-41.

Zahirovic, S., Müller, R. D., Seton, M. & Flament, N. (2015). Tectonic speed limits from plate kinematic reconstructions. *Earth and Planetary Science Letters* **418**, 40-52.

Ziberna, L., Nimis, P., Kuzmin, D. & Malkovets, V. G. (2016). Error sources in single-clinopyroxene thermobarometry and a mantle geotherm for the Novinka kimberlite, Yakutia. *American Mineralogist* **101**, 2222-2232.

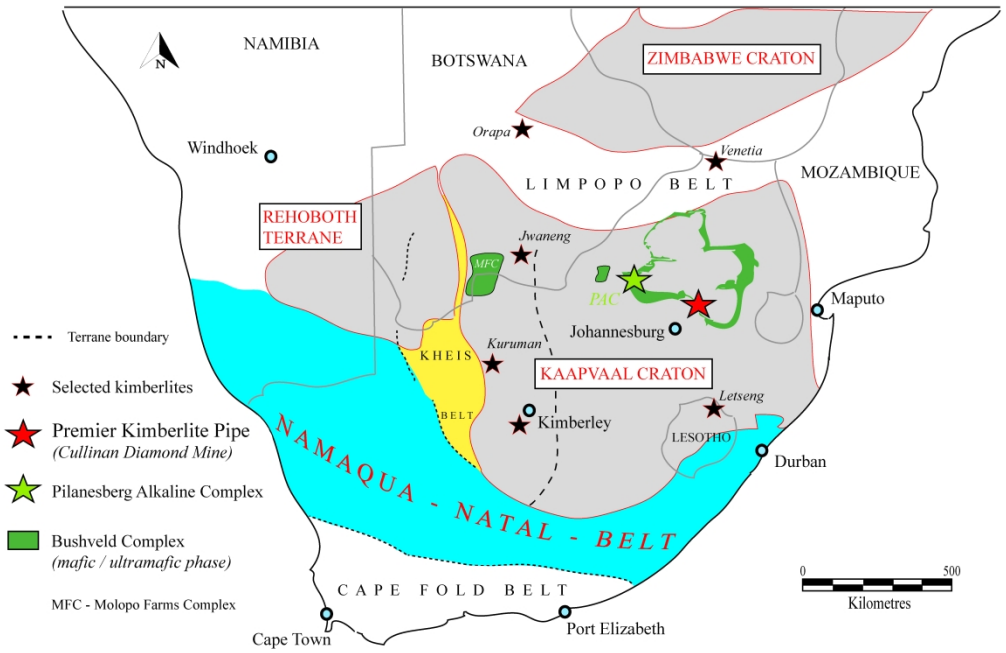

Figure 1:
Geological map of southern Africa showing the outline of the Archean Kaapvaal craton and surrounding Proterozoic terranes plus mobile belts (adopted from Tappe et al., 2020b). The 1153.3 ± 5.3 Ma Premier kimberlite pipe (Cullinan Diamond Mine) is located in the Republic of South Africa on the central Kaapvaal craton at the southern margin of the ca. 2056 Ma Bushveld Complex. The ca. 1400 Ma Pilanesberg alkaline complex (PAC) that intrudes the western lobe of the Bushveld Complex, as well as several renowned Group-1 kimberlite localities on and around the Kaapvaal craton, ranging in age between 1835 and 90 Ma, are shown for reference.

244x157mm (600 x 600 DPI)

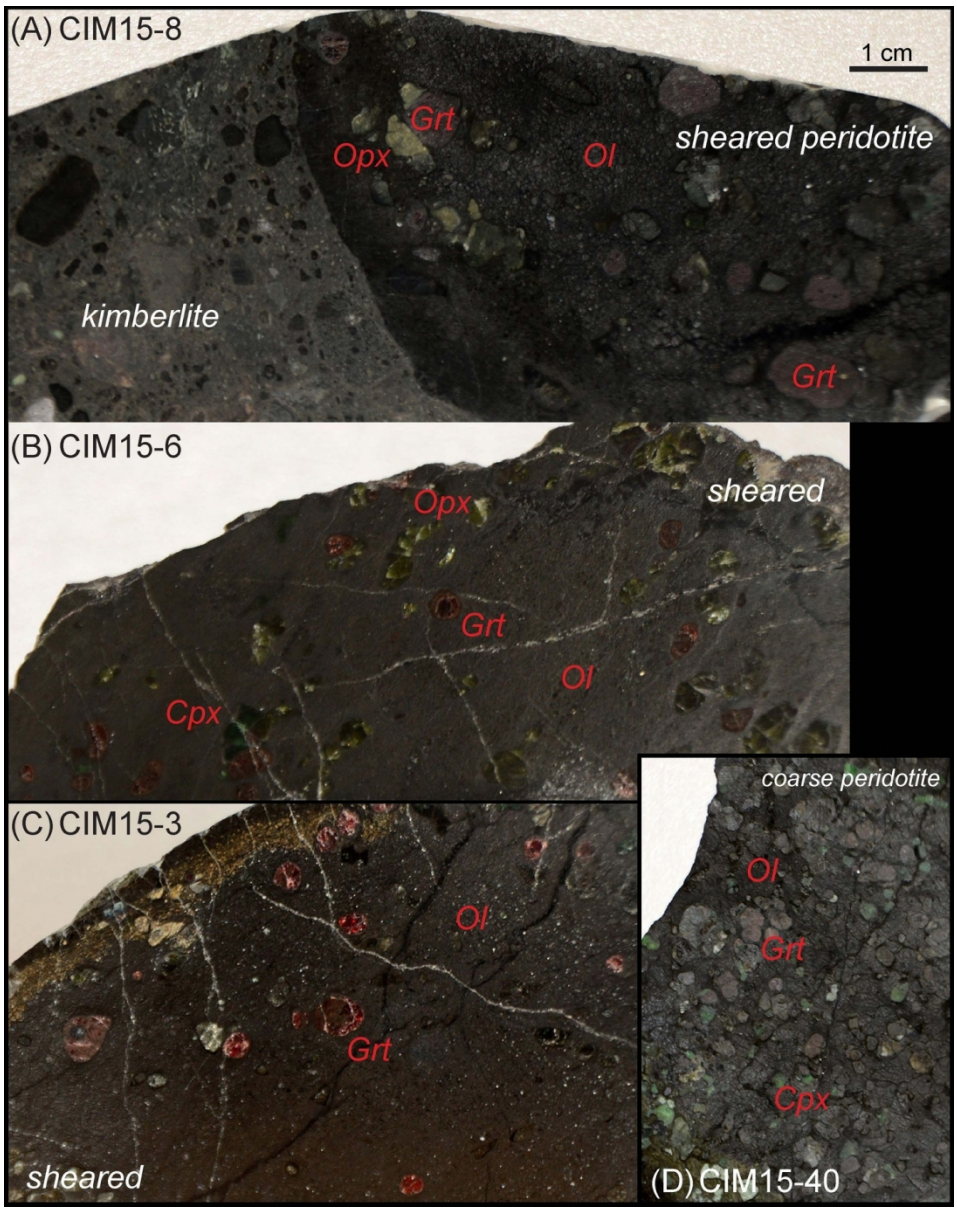

Figure 2:
Photographs of representative sheared peridotite xenoliths (A-C) and coarse peridotite 'nodule' CIM15-40 (D) from the ca. 1150 Ma old Premier kimberlite pipe, Cullinan Diamond Mine, on the central Kaapvaal craton. Panel A reveals the contact between sheared peridotite xenolith CIM15-8 and 'Grey' volcaniclastic kimberlite that fills large volumes of the ~32 hectares large Premier diatreme structure (Tappe et al., 2018a). The scale bar in Panel A applies to all panels. Ol – olivine, Grt – garnet, Opx – orthopyroxene, Cpx – clinopyroxene.

124x157mm (300 x 300 DPI)

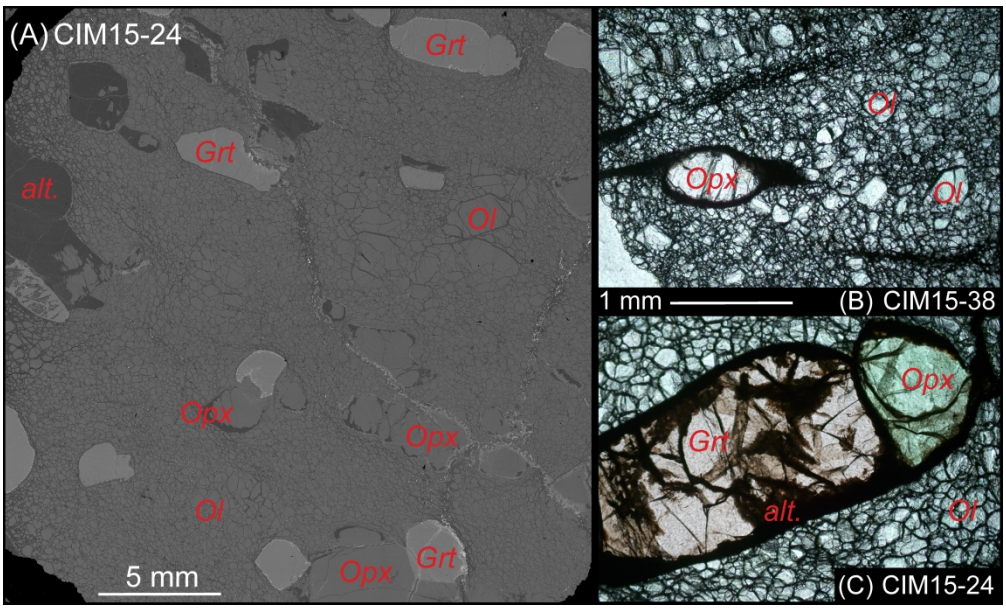

Figure 3:
(A) Back-scattered electron image map of sheared peridotite xenolith CIM15-24 from the Premier kimberlite pipe at the scale of an entire standard petrographic thin section. The BSE map was created with a FEI Quanta 600F MLA system that is equipped with two Bruker 4010 Xflash X-ray detectors. The laminated and disrupted peridotite fabric with isolated garnet–orthopyroxene porphyroclasts set in a matrix of olivine neoblasts can be identified. Note at the image centre the coarser olivine porphyroclasts that underwent grain-size-reduction and neoblast formation along their margins. (B-C) Photomicrographs of sheared peridotite xenoliths from Premier pipe under plane-polarized light. Note the strong ductile deformation textures with development of recrystallization tails that can be used as kinematic shear-sense indicators. Note further touching relationships between coexisting garnet and orthopyroxene grains enabling pressure estimations based on Al-exchange. The scale bar in Panel B also applies to Panel C. Ol – olivine, Grt – garnet, Opx – orthopyroxene, Cpx – clinopyroxene, alt – alteration (e.g., kelyphite).

288x172mm (600 x 600 DPI)

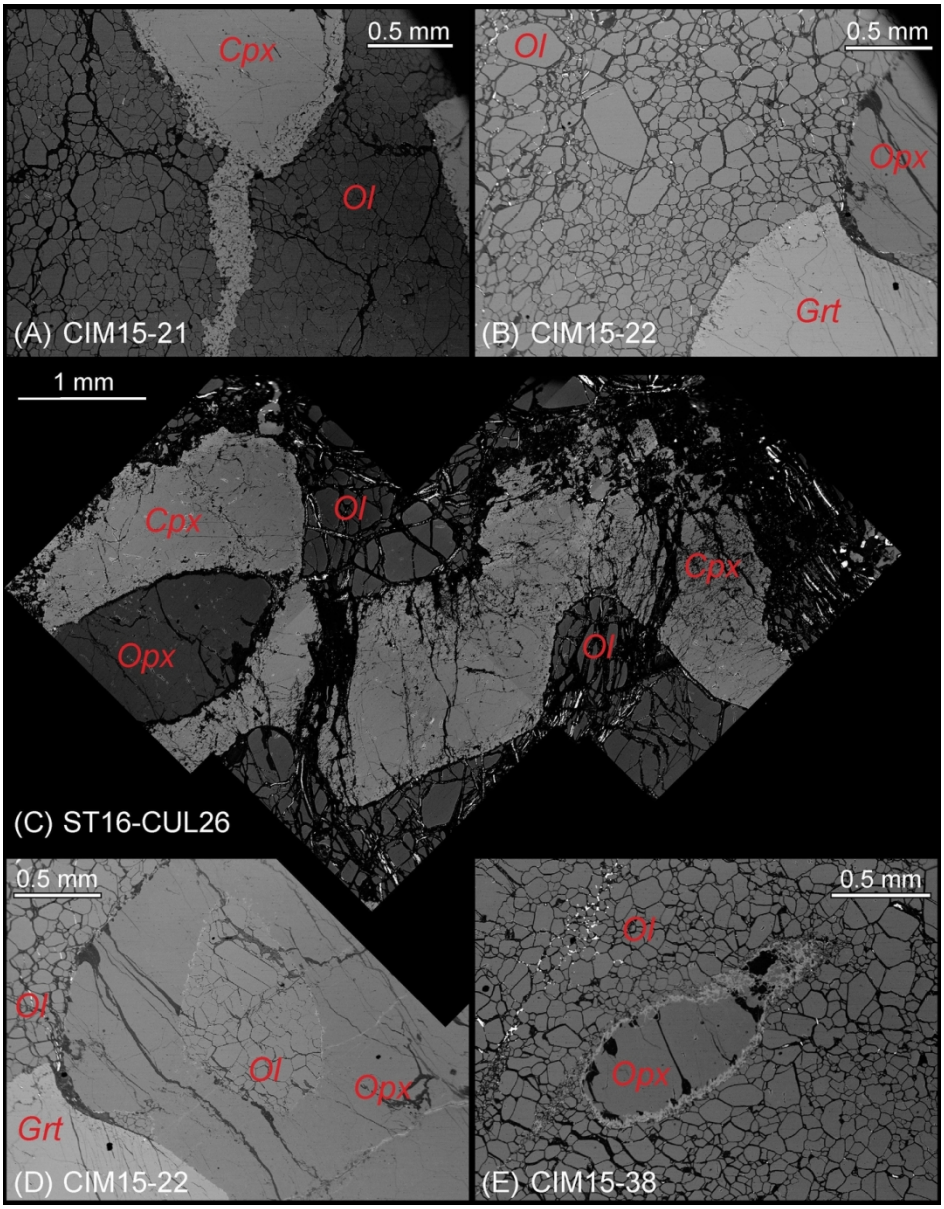

Figure 4:
Back-scattered electron images (A-E) of sheared peridotite xenoliths recovered from the Premier kimberlite pipe, Cullinan Diamond Mine, in South Africa. (A) Stretched clinopyroxene porphyroclast with a spongy-textured halo and fine-grained recrystallization tail engulfed by a matrix that is dominated by olivine neoblasts. (B) Touching pair of garnet and orthopyroxene as part of a porphyroclast set within a fine-grained matrix that consists mainly of neoblastic olivine including undeformed euhedral 'tablets'. (C) Laminated–disrupted porphyroclastic texture of sheared peridotite xenolith ST16-CUL26 showing a tightly folded clinopyroxene crystal at the image centre. The image is a composite comprising four individual BSE images taken at the smallest possible magnification. (D) Touching pair of garnet and orthopyroxene as part of a porphyroclast set within a fine-grained olivine matrix. Note the significant grain-size-reduction and neoblast formation that affected the larger olivine crystal enclosed by porphyroclastic orthopyroxene. (E) Relatively small orthopyroxene porphyroclast with a diffuse melting-induced clinopyroxene halo 'floating' within a neoblastic olivine matrix. Ol – olivine, Grt – garnet, Opx – orthopyroxene, Cpx – clinopyroxene.

120x154mm (300 x 300 DPI)

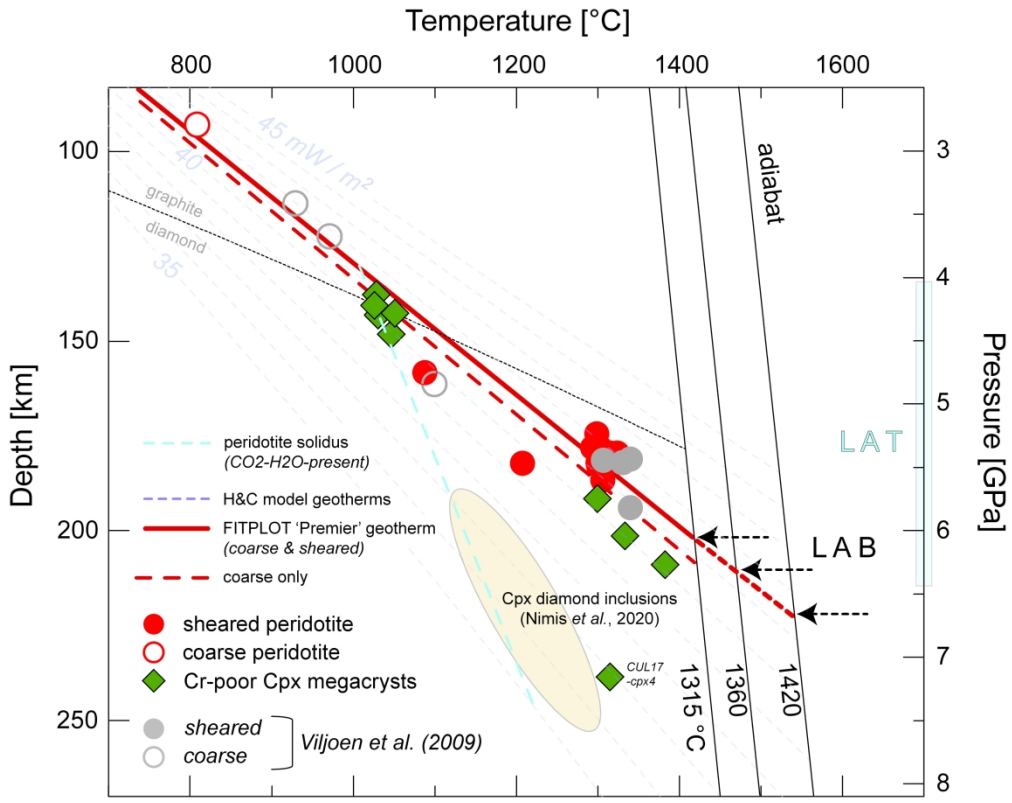

Figure 5:
Pressure–temperature systematics of peridotite xenoliths and Cr-poor clinopyroxene megacrysts from the Premier kimberlite pipe, Cullinan Diamond Mine (all data are listed in Table 1 and Supplementary Data Appendix E). The 'Premier' paleogeotherm (thick solid red curve) was obtained by regression of P-T data for the here investigated and previously reported coarse and sheared / 'deformed' peridotite xenoliths using FITPLOT. The long-dashed red curve represents geotherm fitting that included only coarse peridotite xenoliths. All xenolith data, including those from Viljoen et al. (2009), are calculated or recalculated using the preferred TNG thermobarometer combination (Nickel & Green, 1985; Taylor, 1998). The P-T data for discrete clinopyroxene megacrysts were calculated according to Nimis & Taylor (2000), but are not included into the displayed geotherm fitting (outlier CUL17-cpx4 is discussed in the main text). The brown field for rare 'cold' clinopyroxene xenocrysts and inclusions in some Premier diamonds is based on the data reported in Nimis et al. (2020) (the complete clinopyroxene P-T dataset is displayed in Supplementary Data Figure 2). The graphite/diamond phase transition curve of Day (2012) and conductive model geotherms from Hasterok & Chapman (2011) are shown for reference. The CO2-H2O-present peridotite solidus curve is adopted from Foley et al. (2009) and has been extrapolated beyond 6 GPa applying the data compilations for high-P melting experiments in Tappe et al. (2018b) and Massuyeau et al. (2021). Adiabats for ambient mantle potential temperatures of 1315, 1360 and 1420ºC are shown together with corresponding estimations of the petrological lithosphere–asthenosphere boundary (LAB) beneath the central Kaapvaal craton at ca. 1150 Ma. The blue vertical bar indicates the depth location of a lithosphere–asthenosphere transition zone (LAT), in which low-degree carbonate-rich melts may be ubiquitous (see main text).

297x236mm (300 x 300 DPI)

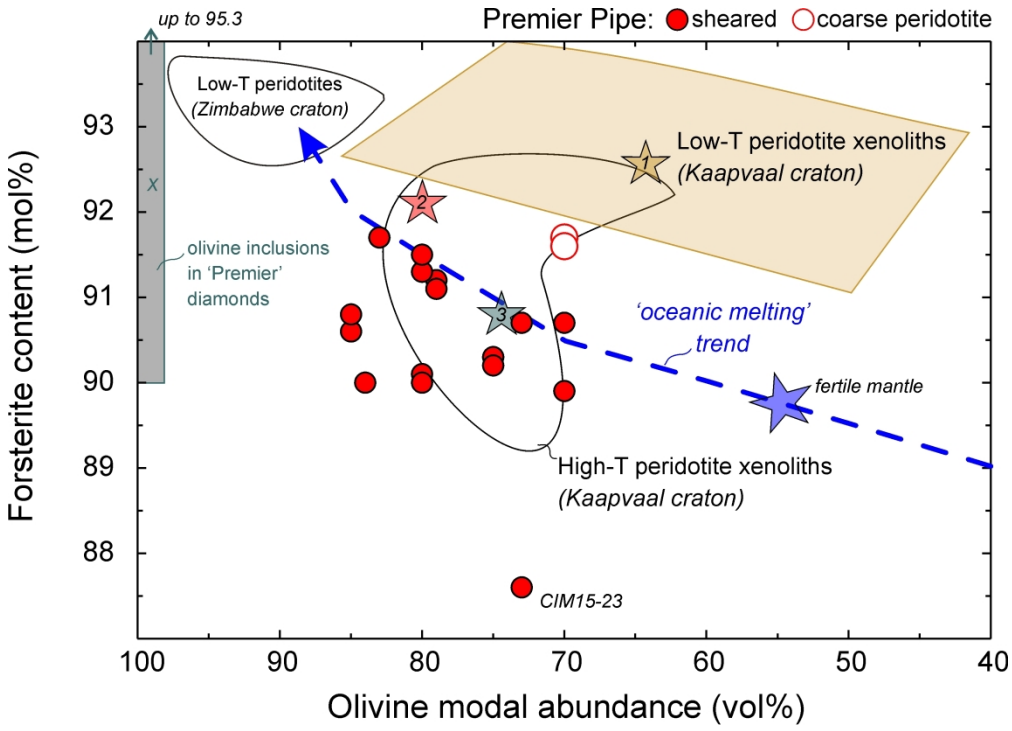

Figure 6:
Average forsterite contents versus corresponding olivine modal abundances of sheared and coarse garnet-facies peridotite xenoliths from the Premier kimberlite pipe, Cullinan Diamond Mine (all data are listed in Supplementary Data Appendix D, E). For the sheared peridotite xenoliths from Premier, both porphyroclastic and neoblastic 'matrix' olivine compositions are shown, without discernable differences in their Mg-numbers within a single nodule. The field for olivine inclusions within Premier diamonds is based on data presented in Viljoen et al. (2014) and Korolev et al. (2018b), with the mean forsterite content shown as an 'X'. Fields for low- and high-temperature peridotite xenoliths from the Kaapvaal and Zimbabwe cratons are adopted from van der Meer et al. (2013). Averages for low-temperature peridotites from the Kaapvaal craton (golden star 1) and other major cratons worldwide (red star 2), as well as for modern abyssal peridotites (green star 3), are taken from Pearson & Wittig (2014). Olivine in sheared peridotites from Premier pipe and other kimberlite occurrences on the Kaapvaal craton resembles olivine from abyssal peridotites of the modern ocean basins, as is also apparent from the proximity to the 'oceanic melting trend' of Boyd (1989).

148x106mm (600 x 600 DPI)

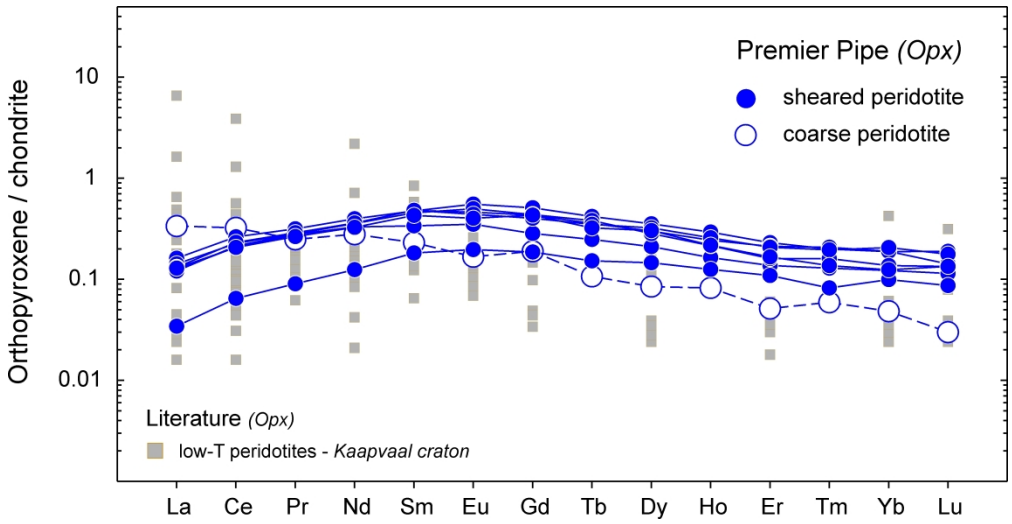

Figure 7:
Chondrite normalized REE distributions for orthopyroxene in sheared and coarse peridotite xenoliths from the Premier kimberlite pipe, Cullinan Diamond Mine (all data are listed in Supplementary Data Appendix D). The REE patterns for orthopyroxene in garnet-facies peridotite xenoliths derived from ca. 90 Ma old kimberlite pipes of Lesotho and Kimberley on the Kaapvaal craton (grey squares) are shown for reference (Simon et al., 2003, 2007). Chondrite values for normalization are from Palme & Jones (2003).

187x96mm (600 x 600 DPI)

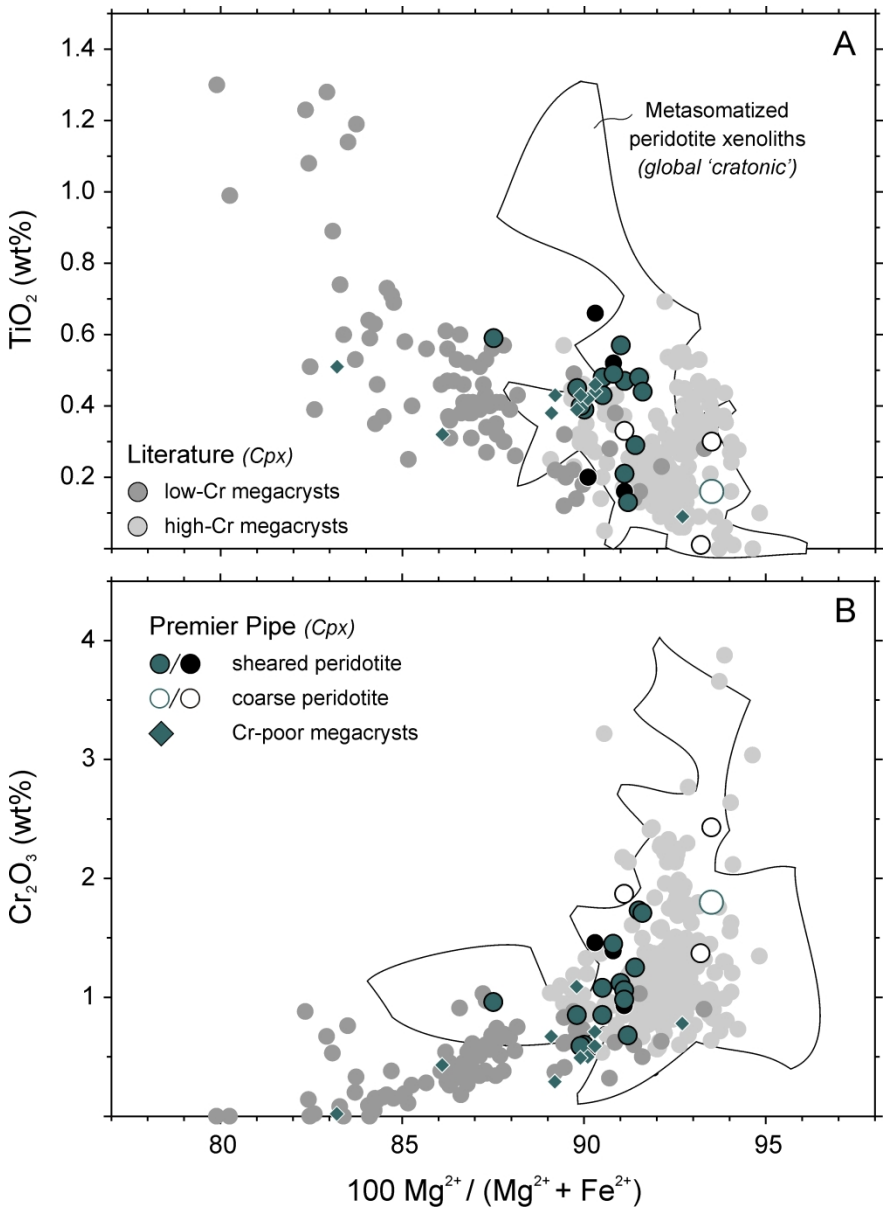

Figure 8:
TiO2 (A) and Cr2O3 (B) contents versus Mg-number for clinopyroxene in sheared and coarse peridotite xenoliths, as well as Cr-poor clinopyroxene megacrysts, from the Premier kimberlite pipe, Cullinan Diamond Mine (all data are listed in Supplementary Data Appendix D). Premier pipe literature data for clinopyroxene from sheared (filled black circles) and coarse (open black circles) peridotite xenoliths are taken from Viljoen et al. (2009). The data compilation for clinopyroxene megacrysts from kimberlite localities worldwide is based on Bussweiler et al. (2018). The field for clinopyroxene compositions in metasomatized peridotite xenoliths from cratons worldwide is based on data provided by Kopylova et al. (1999), Simon et al. (2003, 2007), Aulbach et al. (2007), Rehfeldt et al. (2008), Kargin et al. (2017), and Bussweiler et al. (2018).

145x199mm (600 x 600 DPI)

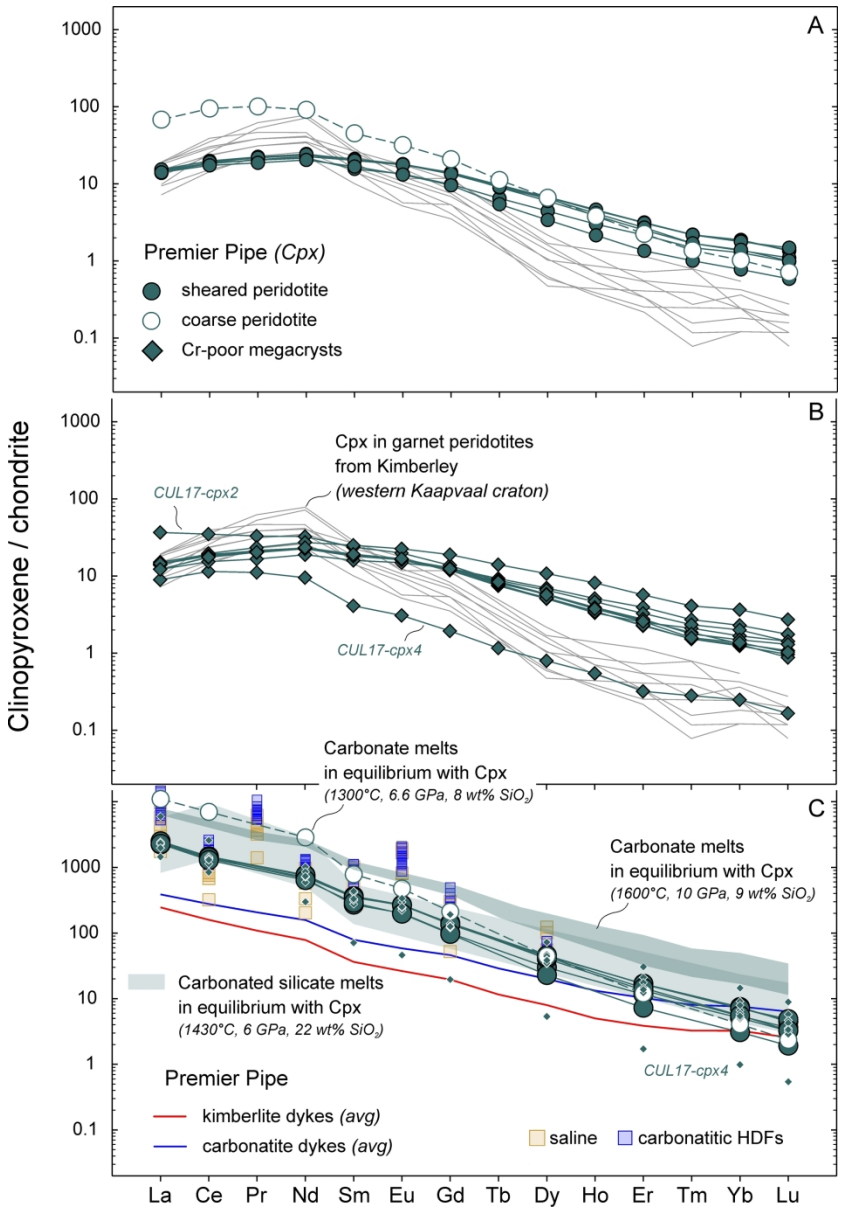

Figure 9:
Chondrite normalized REE distributions for clinopyroxene in sheared and coarse peridotite xenoliths (A) and for Cr-poor clinopyroxene megacrysts (B) from the Premier kimberlite pipe, Cullinan Diamond Mine (all data are listed in Supplementary Data Appendix D). (C) Reconstructed equilibrium melt compositions that may have been responsible for the metasomatic nature of clinopyroxene in garnet-facies peridotite xenoliths from the Premier kimberlite pipe, and may have also caused clinopyroxene megacryst formation. Both the effects of 'carbonate-dominated' (cpx/melt partition coefficients from Dasgupta et al., 2009 and Girnis et al., 2013) and 'carbonated silicate' (Keshav et al., 2005) melts at P-T conditions equivalent to the lithosphere–asthenosphere boundary beneath the central Kaapvaal craton are shown. Average kimberlite (red line) and carbonatite (blue line) dyke compositions from Premier pipe are based on the data presented in Tappe et al. (2020b). The extremely high LREE–MREE concentrations of saline and high-Mg carbonatitic high-density fluids (HDFs) entrapped in diamonds from lithospheric mantle columns of cratons worldwide (Weiss et al., 2011, 2018) suggest their possible involvement in the origin of enriched clinopyroxene signatures within the Kaapvaal continental root. The REE patterns for clinopyroxene from garnet-facies peridotite xenoliths of the

Kimberley kimberlite cluster on the western Kaapvaal craton (grey lines) are shown for reference in Panels A-B-C (Simon et al., 2007). Chondrite values for normalization are from Palme & Jones (2003).

191x276mm (300 x 300 DPI)

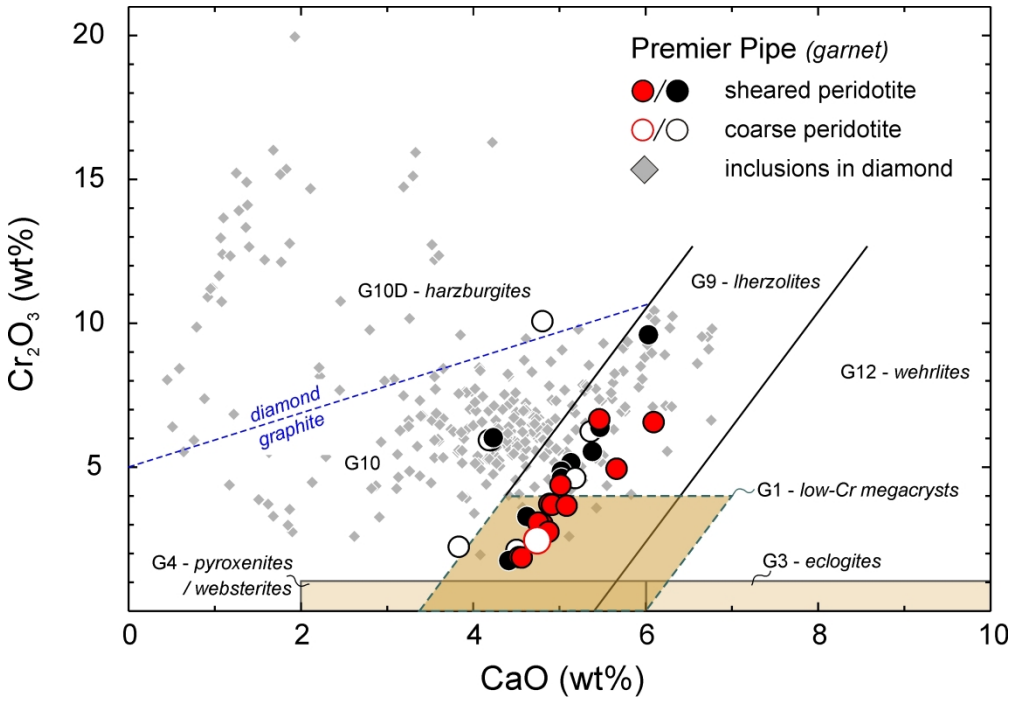

Figure 10:
Cr2O3 versus CaO contents (wt.%) of garnet in sheared and coarse peridotite xenoliths from the Premier kimberlite pipe, Cullinan Diamond Mine (all data are listed in Supplementary Data Appendix D). The garnet 'G-type' classification and the 'graphite–diamond constraint' are according to Grütter et al. (2004). Literature data for garnet from sheared (filled black circles) and coarse (open black circles) peridotite xenoliths, as well as from diamond inclusions (filled grey diamond symbol) are taken from Viljoen et al. (2009) and Viljoen et al. (2014), respectively. Note the partial overlap between G9 lherzolitic garnet grains from Premier pipe and the compositional field of G1 low-Cr garnet megacrysts.

147x101mm (600 x 600 DPI)

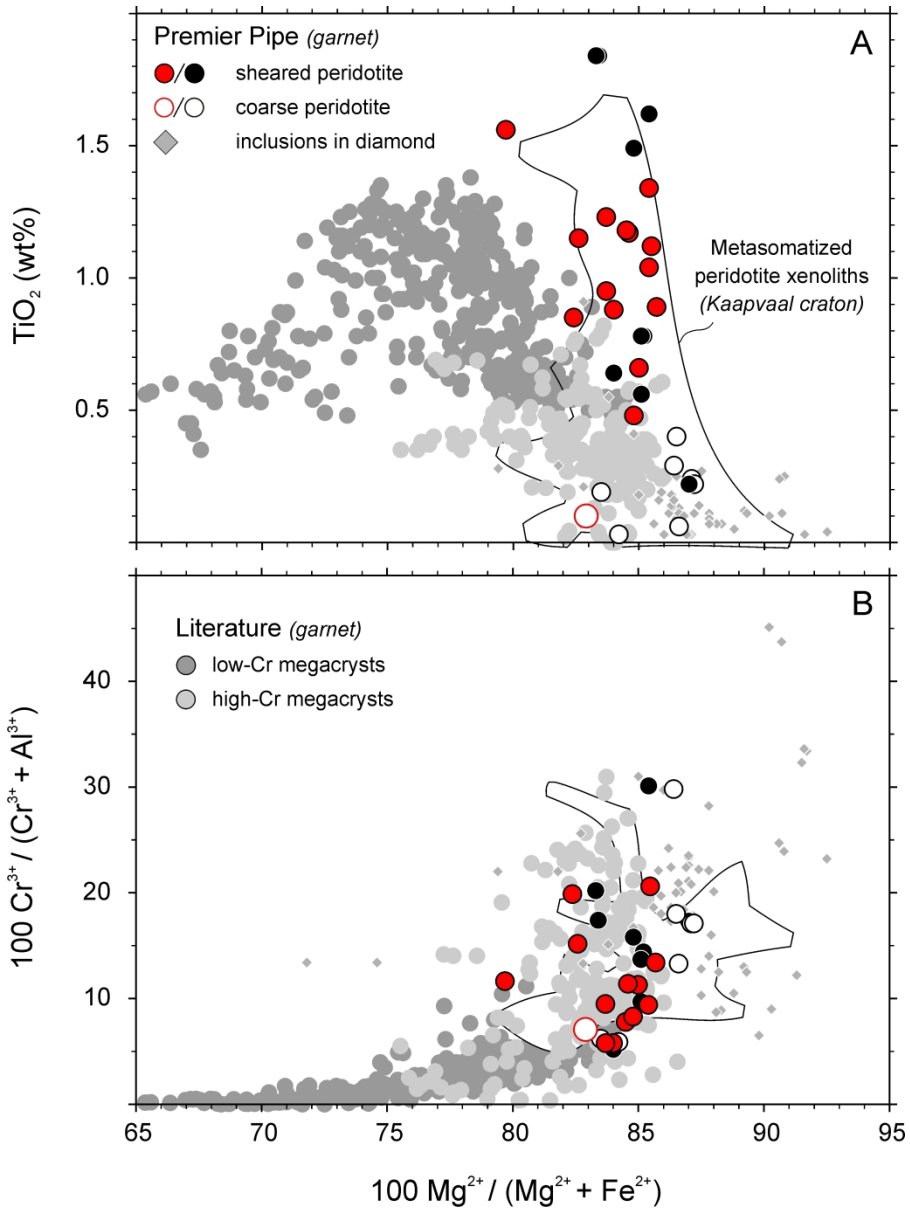

Figure 11:
TiO2 content (A) and Cr-number (B) versus Mg-number for garnet in sheared and coarse peridotite xenoliths from the Premier kimberlite pipe, Cullinan Diamond Mine (all data are listed in Supplementary Data Appendix D). Premier pipe literature data for garnet from sheared (filled black circles) and coarse (open black circles) peridotite xenoliths, as well as from diamond inclusions (filled grey diamond symbol) are taken from Viljoen et al. (2009) and Viljoen et al. (2014), respectively. The data compilation for garnet megacrysts from localities worldwide is based on Bussweiler et al. (2018), and dominated by southern African occurrences for the low-Cr suite (filled dark grey circles), as opposed to occurrences located mainly on the Slave craton in Canada for the high-Cr megacrysts (filled light grey circles). The field for garnet compositions from metasomatized peridotite xenoliths of the Kaapvaal craton is based on data compiled in Bussweiler et al. (2018).

151x201mm (600 x 600 DPI)

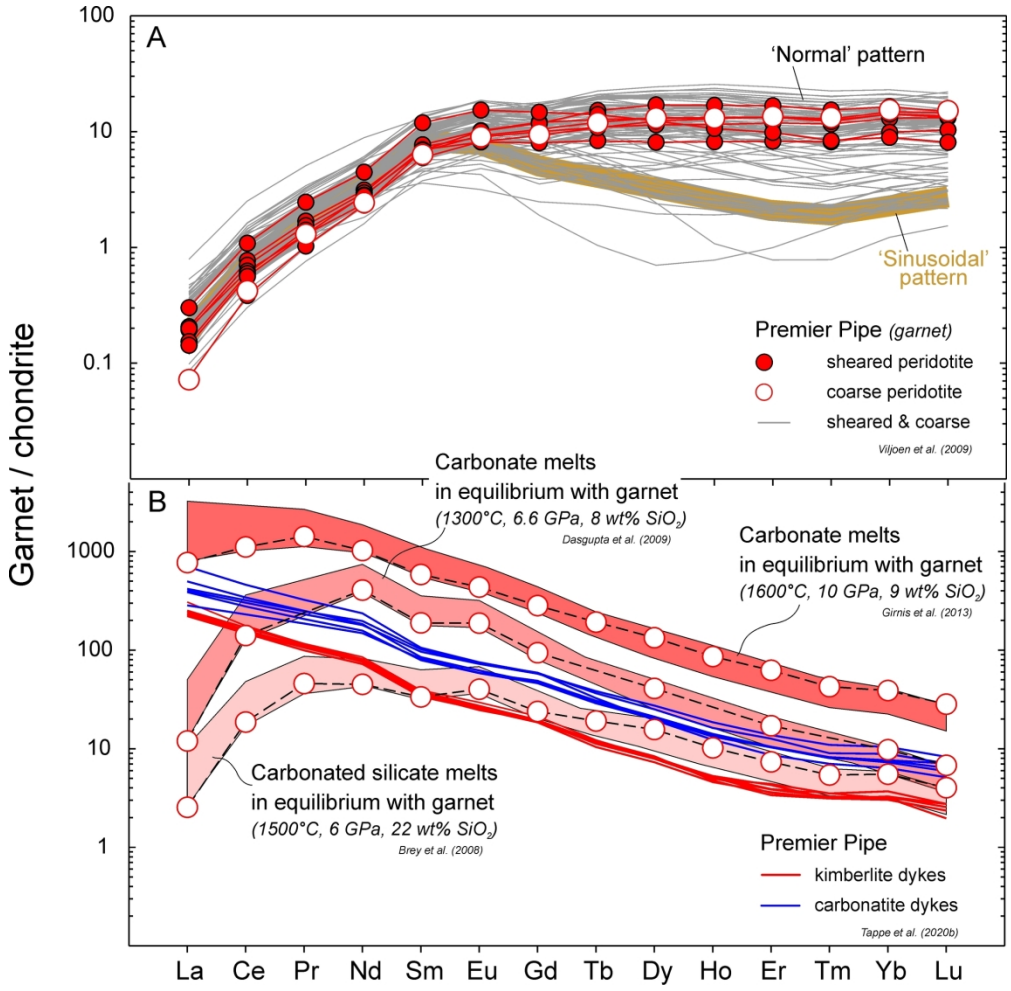

Figure 12:
(A) Chondrite normalized REE distributions for garnet in sheared and coarse peridotite xenoliths from the Premier kimberlite pipe, Cullinan Diamond Mine (all data are listed in Supplementary Data Appendix D). Premier pipe literature data for garnet from sheared / deformed and coarse peridotite xenoliths (grey lines) are taken from Viljoen et al. (2009) and display both 'normal' and 'sinusoidal' patterns. (B) Reconstructed equilibrium melt compositions that may have been responsible for the metasomatic nature of garnet in peridotite xenoliths from the Premier kimberlite pipe. Both the effects of 'carbonate-dominated' (garnet/melt partition coefficients from Dasgupta et al., 2009 and Girnis et al., 2013) and 'carbonated silicate' (Brey et al., 2008) melts at P-T conditions equivalent to the lithosphere–asthenosphere boundary beneath the central Kaapvaal craton are shown. Data for fresh kimberlite (red lines) and carbonatite (blue lines) dykes from Premier pipe are from Tappe et al. (2020b). Chondrite values for normalization are from Palme & Jones (2003).

192x187mm (300 x 300 DPI)

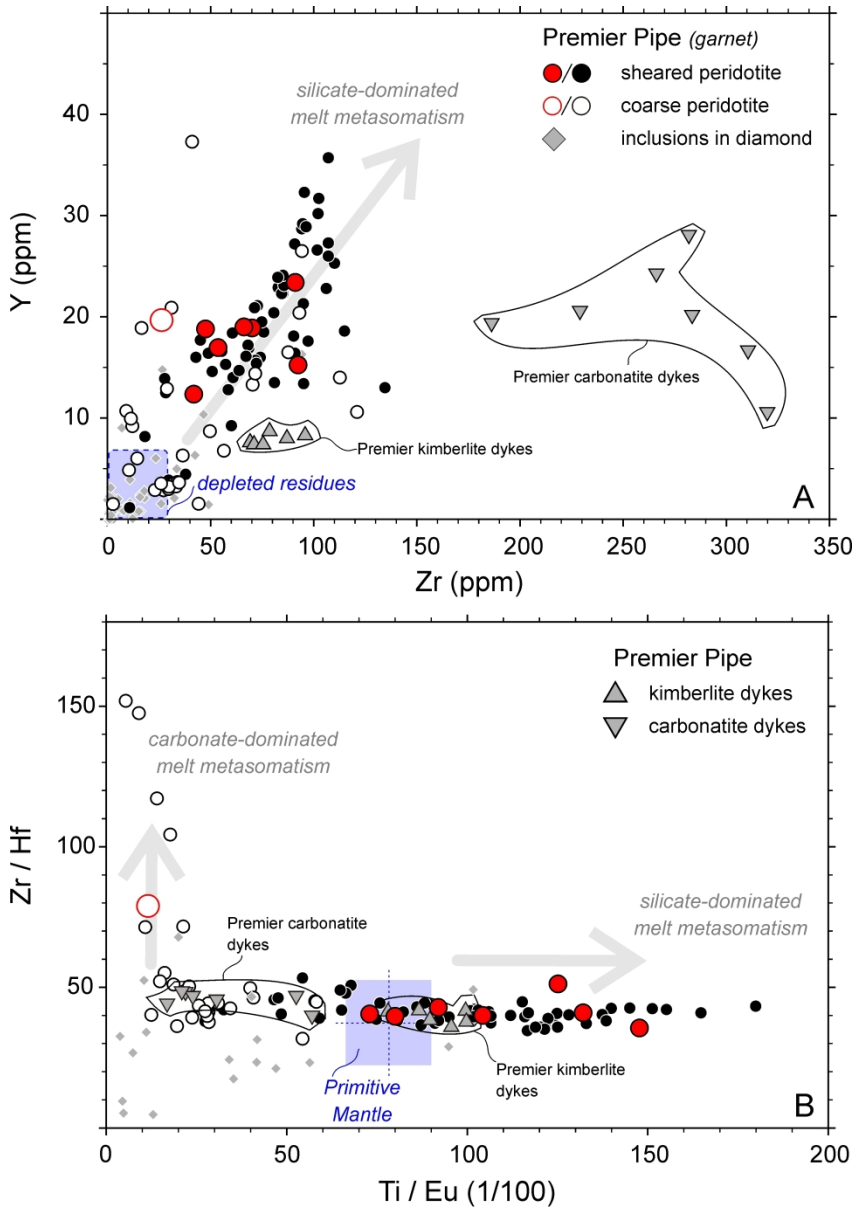

Figure 13:
(A) Y versus Zr contents, and (B) Zr/Hf versus Ti/Eu ratios of garnet in sheared and coarse peridotite xenoliths from the Premier kimberlite pipe, Cullinan Diamond Mine (all data are listed in Supplementary Data Appendix D). Premier pipe literature data for garnet from sheared (filled black circles) and coarse (open black circles) peridotite xenoliths, as well as from diamond inclusions (filled grey diamond symbol) are taken from Viljoen et al. (2009) and Viljoen et al. (2014), respectively. Data for fresh kimberlite (filled grey triangle) and carbonatite (filled grey inverted triangle) dykes from Premier pipe are from Tappe et al. (2020b). The layout of Panel A is adopted from Griffin & Ryan (1995), with some modification to the metasomatic trend. The layout of Panel B is adopted from Shu & Brey (2015), with modifications of the metasomatic trends. Note that the Ti/Eu values have been divided by a hundred for simplicity's sake. Primitive mantle composition is from Palme & O'Neill (2003).

148x210mm (600 x 600 DPI)

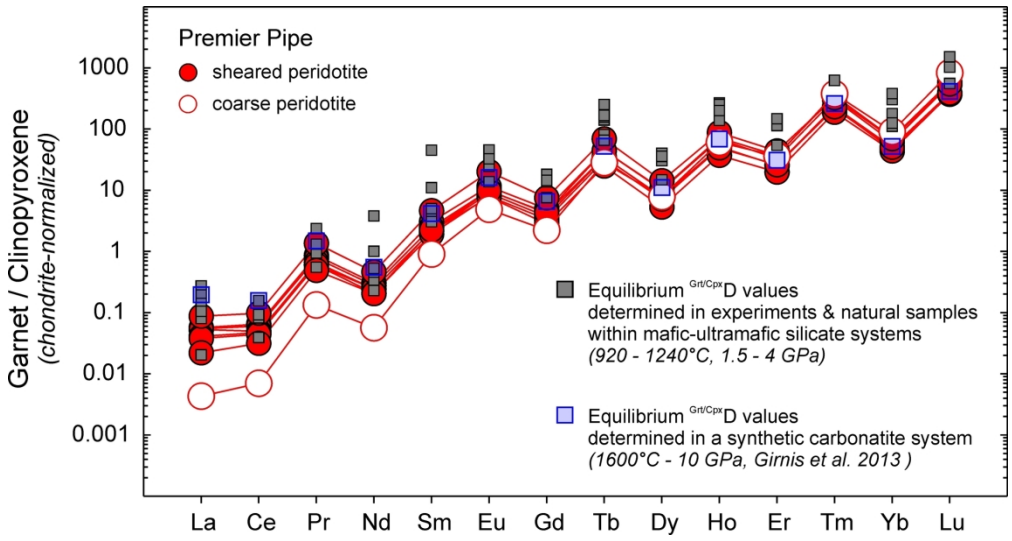

Figure 14:
REE distribution coefficients (chondrite-normalized, Palme & Jones, 2003) for coexisting garnet and clinopyroxene in sheared and coarse peridotite xenoliths from the Premier kimberlite pipe, Cullinan Diamond Mine (all data are listed in Supplementary Data Appendix D). A range of equilibrium Grt/CpxD values determined either experimentally (Green et al., 2000; Adam & Green, 2006; Xiong, 2006; Girnis et al., 2013) or on natural rocks (Zack et al., 1997) is shown for comparison, indicating trace element equilibrium to subtle disequilibrium for the Premier sheared peridotite xenoliths, and notable LREE disequilibrium for coarse peridotite sample CIM15-040. For this sample, clinopyroxene is more LREE enriched than predicted by the composition of coexisting garnet.

181x96mm (300 x 300 DPI)

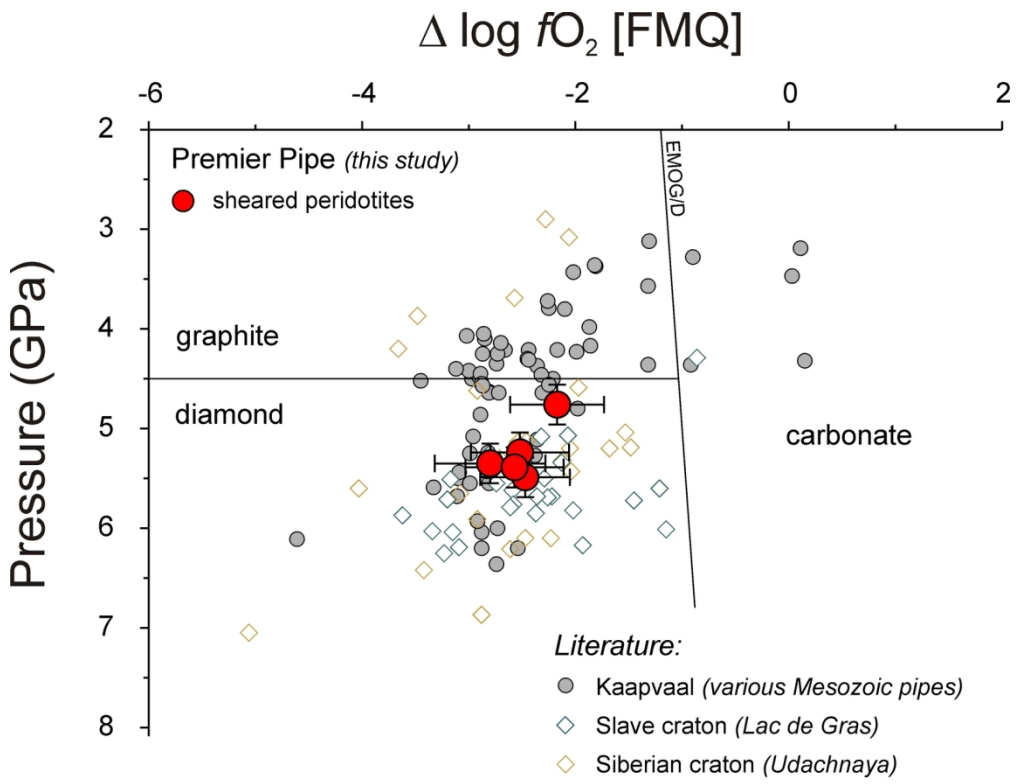

Figure 15:
The pressure versus ΔlogfO2 systematics (relative to the FMQ buffer) of sheared garnet peridotite xenoliths from the Premier kimberlite pipe, Cullinan Diamond Mine (all data are listed in Table 1 and Supplementary Data Appendix E). The error bars entail the 2S.E. uncertainties of the fO2 calculations using the formulation by Stagno et al. (2013) and an estimated uncertainty of 0.2 GPa for pressure calculations using the calibration by Nickel & Green (1985). The previously published data for garnet peridotite xenoliths from the Kaapvaal (Woodland & Koch, 2003; Creighton et al., 2009; Lazarov et al., 2009; Hanger et al., 2015), Slave (Creighton et al., 2010; Yaxley et al., 2017) and Siberian (Goncharov et al., 2012; Yaxley et al., 2012) cratons are recalculated using the Stagno et al. (2013) and Nickel & Green (1985) methods for fO2 and pressure estimations, respectively (Supplementary Data Appendix B). The graphite/diamond phase transition and graphite/diamond versus carbonate stability reaction in a peridotitic system [EMOG/D] at cratonic thermal conditions are adopted from Yaxley et al. (2017).

148x113mm (300 x 300 DPI)

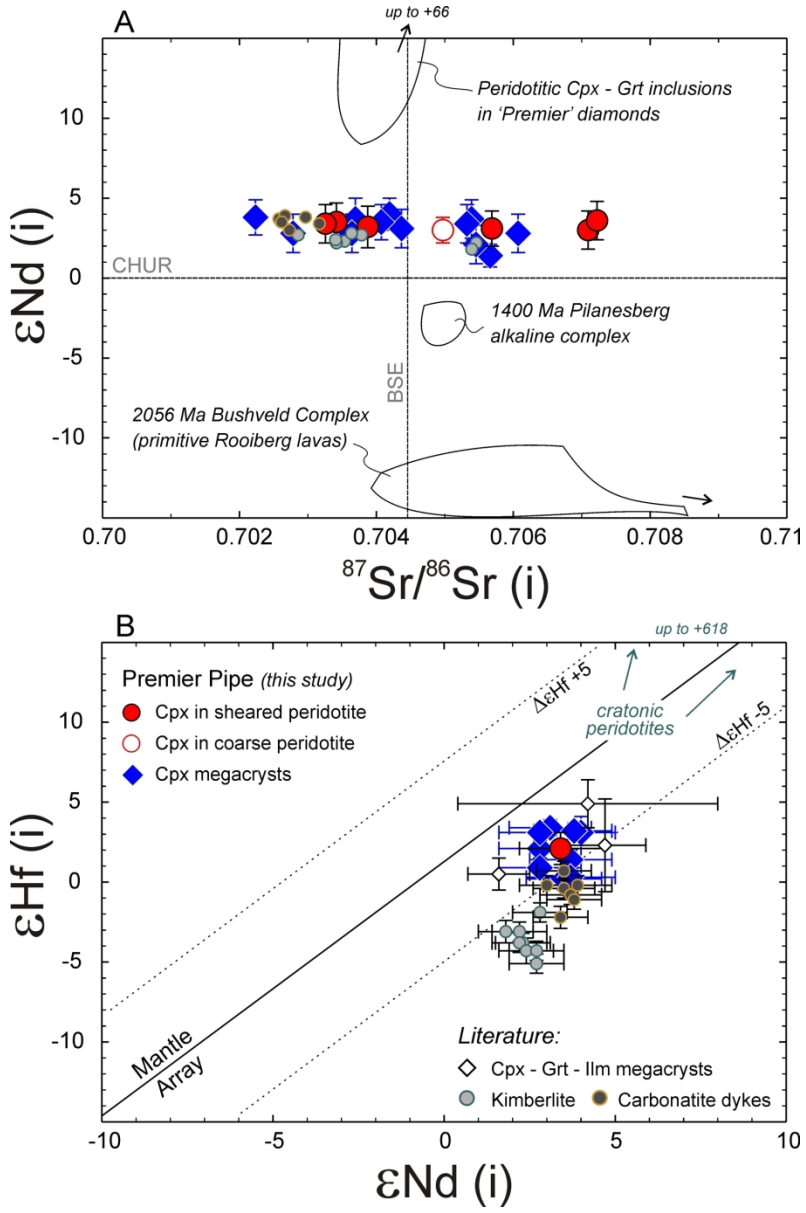

Figure 16:
Initial εNd versus 87Sr/86Sr (A) and εHf versus εNd (B) for clinopyroxene from sheared and coarse peridotite xenoliths, as well as for discrete Cr-poor clinopyroxene megacrysts from the Premier kimberlite pipe, Cullinan Diamond Mine (all data are listed in Table 2 and Supplementary Data Appendix E). Published data for Cr-poor megacrysts (cpx – clinopyroxene, grt – garnet, ilm – ilmenite) from Premier pipe are taken from Nowell et al. (2004). The data for Premier kimberlite and carbonatite dykes are from Tappe et al. (2020b). In Panel A, the Sr-Nd isotope data for clinopyroxene and garnet inclusions within peridotitic diamonds from Premier pipe (Richardson et al., 1993), the ca. 1400 Ma Pilanesberg alkaline complex (Cawthorn et al., 2012), and basaltic lavas from the Rooiberg Group of the ca. 2056 Ma Bushveld Complex on the central Kaapvaal craton (Günther et al., 2018) are shown for comparison. All data in Panel A and B are corrected to the kimberlite magma emplacement age of ca. 1150 Ma for Premier pipe (Tappe et al., 2018a) and they entail a full propagation of uncertainties shown by the error bars (see Methods and the footnote to Table 2). In Panel B, the 'mantle array' is after Chauvel et al. (2008) and the vectors pointing toward depleted ancient cratonic mantle peridotites are after Tappe et al. (2020b).

146x222mm (300 x 300 DPI)

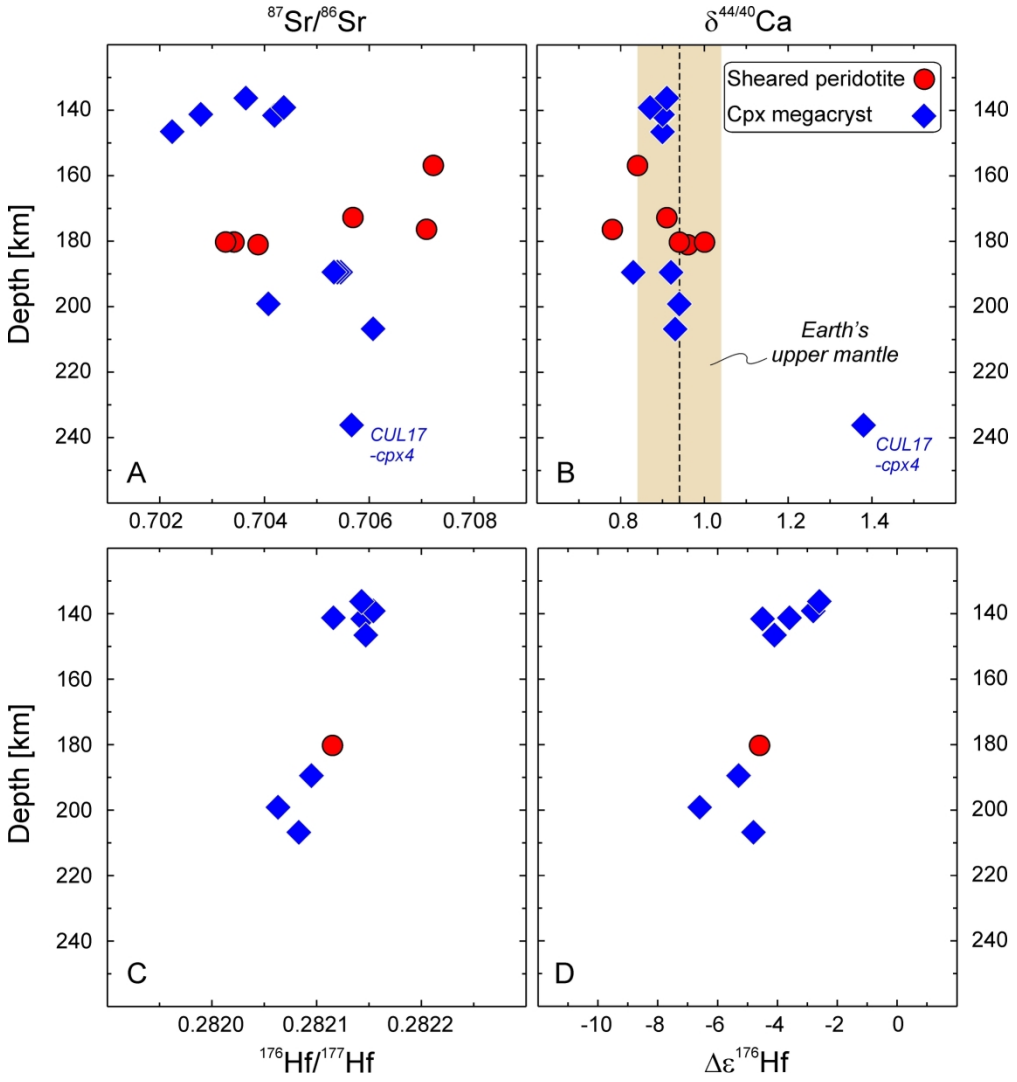

Figure 17:
Initial 87Sr/86Sr (A), δ44/40Ca (B), initial 176Hf/177Hf (C), and initial ΔεHf (D) compositions versus the equilibration depths of clinopyroxene porphyroclasts from sheared peridotite xenoliths and of discrete clinopyroxene megacrysts from the Premier kimberlite pipe, Cullinan Diamond Mine (all data are listed in Supplementary Data Appendix E). No hafnium isotope data are available for megacryst CUL17-cpx4 due to its very low Hf concentration. The upper mantle δ44/40Ca composition is after Chen et al. (2019).

193x206mm (300 x 300 DPI)

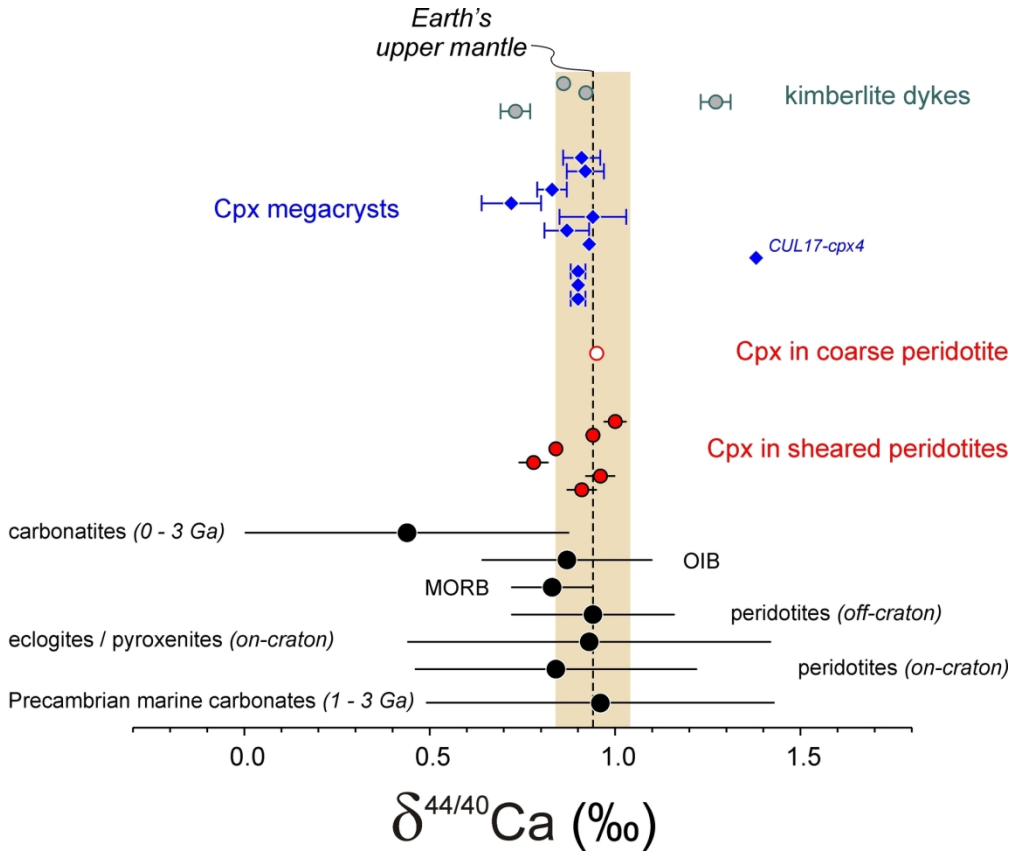

Figure 18:
The δ44/40Ca values for clinopyroxene from sheared and coarse peridotite xenoliths, as well as for discrete Cr-poor clinopyroxene megacrysts from the Premier kimberlite pipe, Cullinan Diamond Mine, reported relative to SRM-915a (all data are listed in Table 2 and Supplementary Data Appendix E). The Ca isotopic compositions of four kimberlite dykes from Premier pipe have also been analysed for comparative purposes. Published δ44/40Ca data for relevant rock types and geochemical reservoirs are taken from the following literature sources and compilations (averages ± 2S.D.): continental peridotite xenoliths (Kang et al., 2017), cratonic eclogites/pyroxenites (Smart et al., 2021), modern oceanic basalts (Schiller et al., 2016; Chen et al., 2019), modern to 3 Ga old Ca-Mg-Fe carbonatites (Amsellem et al., 2020; Sun et al., 2021) and 1-3 Ga old Precambrian marine carbonates (Blättler & Higgins, 2017). The average δ44/40Ca value for the upper mantle of 0.94 ± 0.1‰ (dashed vertical line plus error envelop) is based on Chen et al. (2019).

162x137mm (300 x 300 DPI)

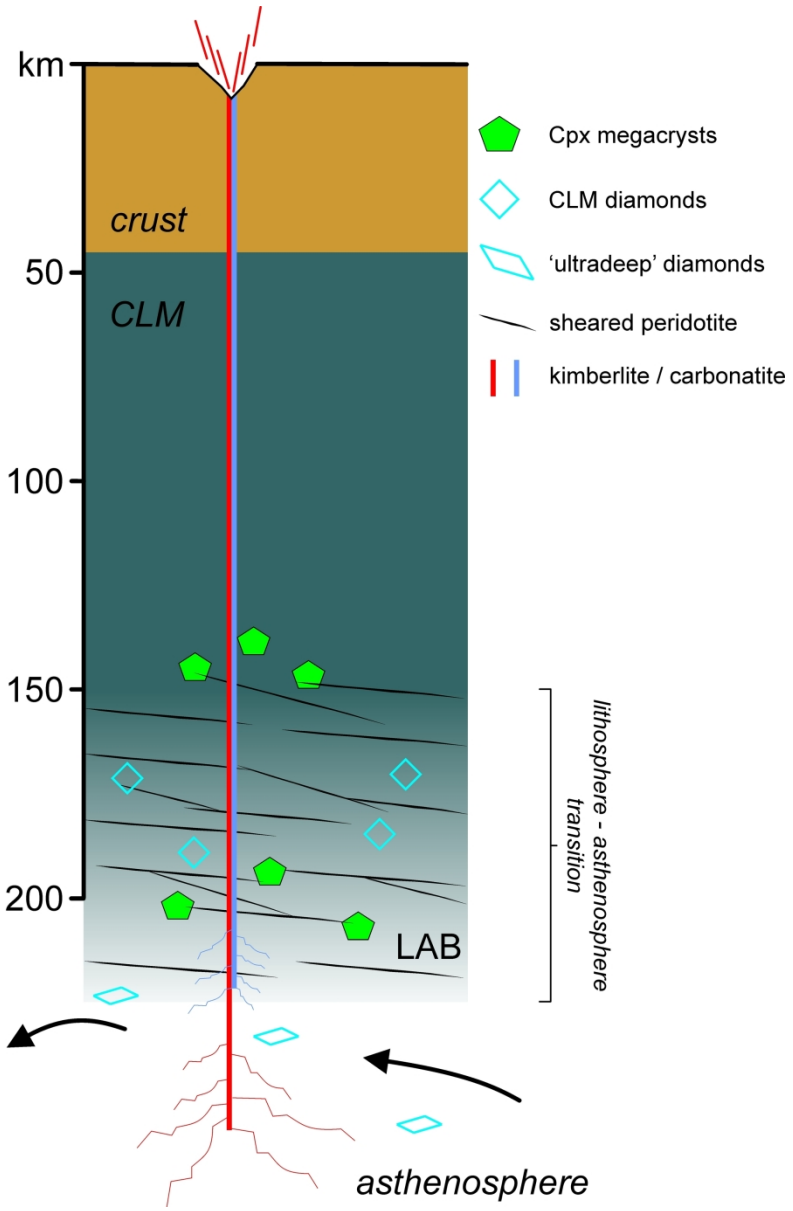

Figure 19:
Schematic model of the central Kaapvaal cratonic mantle lithosphere during the ca. 1150 Ma kimberlite and carbonatite magma eruptions at Premier/Cullinan. This study proposes a ≥50 km thick lithosphere–asthenosphere transition zone between ~150-225 km depth, where strong plastic deformation creates a network of narrow subhorizontal shear zones as represented by abundant sheared peridotite xenoliths. Stress-driven segregation of percolating carbonate-rich melts may provide a link between the common association of megacrysts and sheared peridotites as part of kimberlite mantle cargo. Both lithospheric and sublithospheric (i.e., 'ultradeep') diamonds are shown for reference, but they are not discussed in detail as part of this model. CLM – cratonic lithospheric mantle, LAB – lithosphere–asthenosphere boundary.

187x287mm (300 x 300 DPI)

Table 1: Petrography, pressure-temperature and oxygen fugacity estimates for peridotite xenoliths and clinopyroxene megacrysts from the Premier kimberlite, Kaapvaal craton, South Africa.

			Mineral abundance (%)					*Thermobarometry			Garnet log fO_2		
ID	**Texture**	**Grain size**	**Ol**	**Opx**	**Cpx**	**Grt**		**P (GPa)**	**T (°C)**		$Fe^{3+}/\sum Fe$	ΔFMQ**	**1SE**
Peridotite xenoliths													
CIM15-001	sheared	VF (<100 μm)	79	10	4	7		5.6	1307				
CIM15-003	sheared	F (100-500 μm)	79	8	7	6		5.2	1299		0.085	-2.52	0.23
CIM15-008	sheared	M (>500 μm)	73	12	8	7		5.5	1315				
CIM15-015	sheared	F (100-500 μm)	80	7	7	6		5.3	1294				
CIM15-016	sheared	F (100-500 μm)	84	6	6	4		5.4	1324		0.088	-2.57	0.23
CIM15-018	sheared	F (100-500 μm)	85	5	7	3		5.5	1303				
CIM15-021	sheared	VF (<100 μm)	80	9	7	4		5.5	1302		0.080	-2.47	0.21
CIM15-022	sheared	F (100-500 μm)	70	11	12	7		5.3	1303		0.080	-2.80	0.26
CIM15-023	sheared	F (100-500 μm)	73	13	8	6		5.5	1303				
CIM15-024	sheared	F (100-500 μm)	80	8	7	5		5.4	1315				
CIM15-038	sheared	VF (<100 μm)	85	7	5	3		5.4	1306				
ST16-26-CUL	sheared	M (>500 μm)	75	13	9	3		5.5	1208				
CIM15-035	[a] coarse in sheared	F (100-500 μm), up to 1.2 cm	70	10	15	5		4.8	1088		0.070	-2.17	0.22
CIM15-050	[a] coarse in sheared	F (100-500 μm), up to 1.2 cm	83	5	10	2		5.5	1301				
CIM15-050re	[a] coarse in sheared	F (100-500 μm), up to 1.2 cm	83	5	10	2		5.5	1301				
CIM15-040	coarse	>2 mm (2-5 mm)	70	14	11	5		2.8	809				
Clinopyroxene megacrysts													
CUL17-CPX01	megacrystic	1 × 3 cm						4.3	1030				
CUL17-CPX02	megacrystic	1 × 3 cm						4.4	1046				
CUL17-CPX03	megacrystic	1 × 3 cm						4.3	1051				
CUL17-CPX04	megacrystic	2 × 2 cm						7.2	1313				
CUL17-CPX05	megacrystic	1 × 2 cm						6.3	1382				
CUL17-CPX06	megacrystic	2 × 2 cm						4.2	1026				
CUL17-CPX07	megacrystic	2 × 2 cm						6.0	1333				
CUL17-CPX08	megacrystic	1 × 2 cm						*no solution*	*no solution*				
CUL17-CPX09	megacrystic	2 × 3 cm						5.7	1299				
CUL17-CPX09re1	megacrystic	2 × 3 cm						5.7	1299				
CUL17-CPX09re2	megacrystic	2 × 3 cm						5.7	1299				
CUL17-CPX10	megacrystic	1 × 2 cm						4.1	1028				

*Preferred pressure and temperature estimations for garnet-facies peridotites based on formulations in Nickel & Green (1985) and Taylor (1998), respectively.

*Pressure and temperature calculations for clinopyroxene megacrysts in equilibrium with garnet-facies peridotites based on formulations in Nimis & Taylor (2000).

**log fO_2 calculations for garnet peridotites based on formulation in Stagno et al. (2013).

Texture and grain size descriptions follow Harte (1977): VF - very fine grained, F - fine grained, M - medium grained.

[a] Cpx megacrystic domains in sheared Ol-rich matrix.

Ol - olivine, Opx - orthopyroxene, Cpx - clinopyroxene, Grt - garnet.

Table 2: Sr-Nd-Hf-Ca isotopic compositions of garnet peridotite xenoliths and clinopyroxene megacrysts from the Premier kimberlite, Kaapvaal craton, South Africa.

		Clinopyroxene isotopic compositions																				Garnet isotopes	
ID	Texture	$^{87}Sr/^{86}Sr_m$	2SE	$^{87}Rb/^{87}Sr$	$^{87}Sr/^{86}Sr_i$	$^{143}Nd/^{144}Nd_m$	2SE	$^{147}Sm/^{144}Nd$	$^{143}Nd/^{144}Nd_i$	εNd_i	*2SD	$^{176}Hf/^{177}Hf_m$	2SE	$^{176}Lu/^{177}Hf$	$^{176}Hf/^{177}Hf_i$	εHf_i	*2SD	** $\Delta\varepsilon Hf_i$	$\delta^{44/40}Ca_{SRM915a}$ (‰)	2SE	$\delta^{44/40}Ca_{SRM915a}$ (‰)	2SE
Peridotite xenoliths																							
CIM15-001	sheared																						
CIM15-003	sheared	0.705728	0.000009	0.00241	0.705688	0.512406	0.000005	0.14504	0.511311	3.1	1.1								0.91	0.04	1.24	0.02
CIM15-008	sheared																						
CIM15-015	sheared																						
CIM15-016	sheared																						
CIM15-018	sheared																						
CIM15-021	sheared	0.704232	0.000009	0.02164	0.703875	0.512595	0.000006	0.16997	0.511312	3.2	1.3								0.96	0.04	1.06	0.04
CIM15-022	sheared	0.707104	0.000007	0.00062	0.707094	0.512541	0.000006	0.16381	0.511304	3.0	1.2								0.78	0.04	1.12	0.03
CIM15-023	sheared																						
CIM15-024	sheared																						
CIM15-038	sheared																						
ST16-26-CUL	sheared																						
CIM15-035	[a] coarse in sheared	0.707364	0.000007	0.00850	0.707224	0.512586	0.000007	0.16578	0.511334	3.6	1.2								0.84	0.003	1.19	0.05
CIM15-050	[a] coarse in sheared	0.703453	0.000006	0.00223	0.703416	0.512560	0.000005	0.16274	0.511331	3.5	1.2								0.94	0.02		
CIM15-050re	[a] coarse in sheared	0.703292	0.000009	0.00223	0.703256	0.512553	0.000006	0.16274	0.511325	3.4	1.2	0.282183	0.000024	0.00312	0.282115	2.1	1.0	-4.6	1.00	0.03		
CIM15-040	coarse	0.705421	0.000007	0.02719	0.704973	0.512040	0.000006	0.09762	0.511303	3.0	0.8								0.95	0.01	1.87	0.03
Clinopyroxene megacrysts																							
CUL17-CPX01	megacrystic	0.704376	0.000006	0.01119	0.704192	0.512363	0.000005	0.13366	0.511354	4.0	1.0	0.282169	0.000025	0.00116	0.282144	3.1	1.0	-4.5	0.90	0.02		
CUL17-CPX02	megacrystic	0.703590	0.000006	0.08229	0.702235	0.512475	0.000007	0.14973	0.511345	3.8	1.1	0.282174	0.000007	0.00126	0.282147	3.2	0.5	-4.1	0.90	0.01		
CUL17-CPX03	megacrystic	0.703050	0.000006	0.01616	0.702784	0.512511	0.000006	0.16145	0.511292	2.8	1.2	0.282169	0.000016	0.00243	0.282116	2.1	0.7	-3.6	0.90	0.02		
CUL17-CPX04	megacrystic	0.705687	0.000005	0.00140	0.705664	0.511875	0.000006	0.08647	0.511223	1.4	0.7								1.38	0.003		
CUL17-CPX05	megacrystic	0.706135	0.000007	0.00373	0.706073	0.512553	0.000005	0.16668	0.511294	2.8	1.2	0.282274	0.000011	0.00882	0.282083	0.9	0.6	-4.8	0.93	0.01		
CUL17-CPX06	megacrystic	0.704666	0.000005	0.01810	0.704368	0.512522	0.000005	0.16042	0.511311	3.1	1.2	0.282176	0.000008	0.00103	0.282154	3.4	0.5	-2.8	0.87	0.06		
CUL17-CPX07	megacrystic	0.704317	0.000007	0.01484	0.704073	0.512406	0.000006	0.14246	0.511330	3.5	1.1	0.282175	0.000015	0.00516	0.282063	0.2	0.7	-6.6	0.94	0.09		
CUL17-CPX08	megacrystic	0.703704	0.000013	0.00055	0.703695	0.512629	0.000005	0.17080	0.511339	3.7	1.3	0.282141	0.000006	0.00355	0.282064	0.3	0.5	-6.9	0.72	0.08		
CUL17-CPX09	megacrystic	0.705467	0.000006	0.00068	0.705456	0.512454	0.000007	0.15869	0.511256	2.1	1.2								0.83	0.04		
CUL17-CPX09re1	megacrystic	0.705402	0.000006	0.00068	0.705391	0.512539	0.000006	0.15869	0.511341	3.7	1.2	0.282201	0.000011	0.00489	0.282095	1.4	0.6	-5.3	0.92	0.05		
CUL17-CPX09re2	megacrystic	0.705336	0.000008	0.00068	0.705325	0.512523	0.000005	0.15869	0.511325	3.4	1.2											
CUL17-CPX10	megacrystic	0.703708	0.000007	0.00399	0.703643	0.512527	0.000005	0.16366	0.511291	2.8	1.2	0.282166	0.000009	0.00109	0.282143	3.1	0.5	-2.6	0.91	0.05		

*The 2-sigma uncertainties of the epsilon Nd and Hf values entail a full error propagation (uncertainties of the 1150 Ma age and parent-daughter element ratios are set at 1% and 5%, respectively).

**Initial $\Delta\varepsilon Hf$ is defined as εHf_i-(1.59*εNd_i+1.28), such that analyses with negative values fall by definition below the Nd-Hf isotope regression line of Chauvel et al. (2008).

[a] Clinopyroxene megacrystic domains in sheared olivine-rich matrix.

Initial isotope ratios calculated for the Premier kimberlite emplacement age of 1150 Ma (Tappe et al., 2018a) using the following decay constants: ^{87}Rb 1.42*10^{-11} a^{-1}; ^{147}Sm 6.54*10^{-12} a^{-1}; ^{176}Lu 1.865*10^{-11} a^{-1}.

Initial epsilon Nd values are calculated using ^{147}Sm decay constant of 6.54*10^{-12} a^{-1} (Lugmair & Marti, 1978); $(^{143}Nd/^{144}Nd)_{CHUR}$ = 0.512630 and $(^{147}Sm/^{144}Nd)_{CHUR}$ = 0.1960 (Bouvier et al., 2008).

Initial epsilon Hf values are calculated using ^{176}Lu decay constant of 1.865*10^{-11} a^{-1} (Scherer et al., 2001); $(^{176}Hf/^{177}Hf)_{CHUR}$ = 0.282785 and $(^{176}Lu/^{177}Hf)_{CHUR}$ = 0.0336 (Bouvier et al., 2008).

Measured Sr, Nd, and Hf isotope ratios are normalized to the following standard values:

NBS987 = $^{87}Sr/^{86}Sr$ value of 0.710245 (Thirlwall, 1991); JNdi-1 = $^{143}Nd/^{144}Nd$ value of 0.512115 (Tanaka et al., 2000); JMC475 = $^{176}Hf/^{177}Hf$ value of 0.282160 (Blichert-Toft et al., 1997).

Powders of BCR-2 and BHVO-2 basalt reference materials were processed alongside the Premier/Cullinan xenoliths and megacrysts, and the following values were obtained during this study in 2018/2019:

BCR-2 = $^{87}Sr/^{86}Sr$ value of 0.705005(±7), n=2; BHVO-2 = $^{87}Sr/^{86}Sr$ value of 0.703469(±7), n=2.

BCR-2 = $^{143}Nd/^{144}Nd$ value of 0.512635(±6), n=3; BHVO-2 = $^{143}Nd/^{144}Nd$ value of 0.512990(±16), n=3.

BCR-2 = $^{176}Hf/^{177}Hf$ value of 0.282873(±22), n=3; BHVO-2 = $^{176}Hf/^{177}Hf$ value of 0.283108(±13), n=3.